

PE&RS

June 2020

Volume 86, Number 6

PHOTOGRAMMETRIC ENGINEERING & REMOTE SENSING | *The official journal for imaging and geospatial information science and technology*





WHITTLES
PUBLISHING

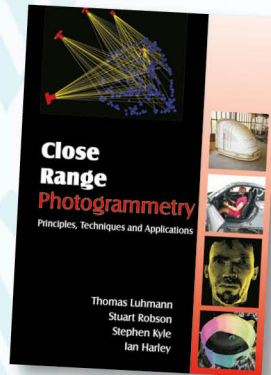
SIMPLY BRILLIANT BOOKS

ASPRS
MEMBER EXCLUSIVE

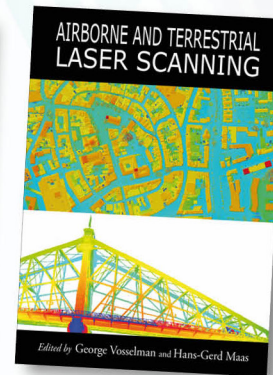
20%
DISCOUNT

ON ALL WHITTLES
PUBLISHING BOOKS
USING CODE WPASPRS2

WHITTLES PUBLISHING'S
STABLE OF CLASSIC
GEOMATICS BOOKS
INCLUDES THE THREE
WINNERS OF THE
PRESTIGIOUS KARL KRAUS
MEDAL AWARDED BY ISPRS



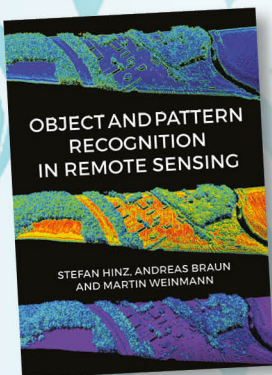
978-1870325-73-8
(Available as a CD)



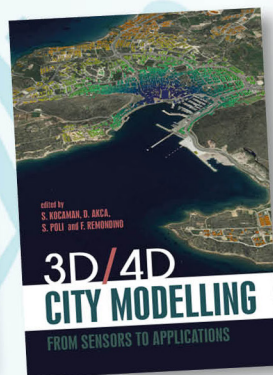
978-1904445-87-6



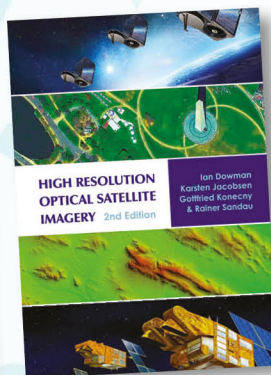
ISBN? Website only has 2nd
edition



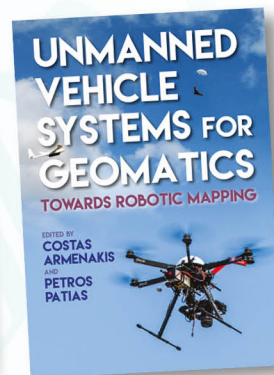
978-184995-128-9



978-184995-475-4



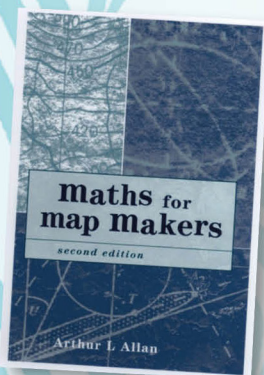
978-184995-390-0



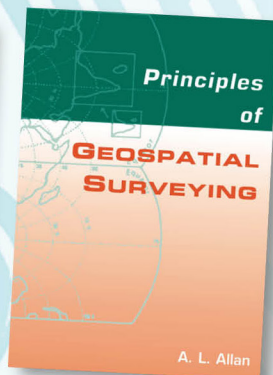
978-184995-127-2

OUR LIST
CONTINUES
TO EXPAND
WITH THESE
NEW TITLES

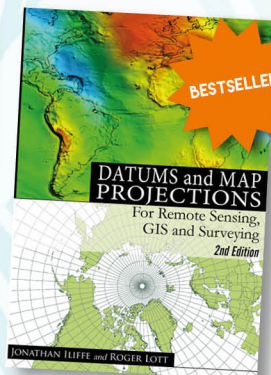
BROWSE OUR WEBSITE TO SEE OUR FULL RANGE
OF ACCLAIMED GEOMATICS BOOKS



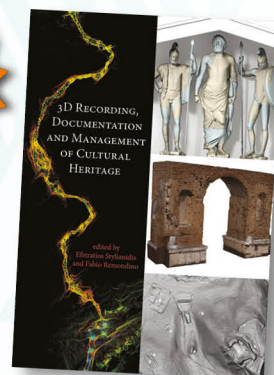
978-1870325-99-8



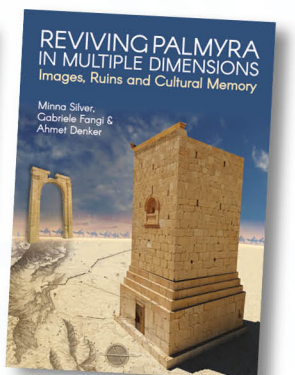
978-1904445-21-0



978-1904445-47-0



978-184995-168-5



978-184995-296-5

ASPRS *GEO WEEK 2020*

ASPRS Geo Week 2020 Technical Program Is Going Virtual In June!

June 22 – 26, 2020

See page 355 or visit the website for more detailed information.

<http://conferences.asprs.org/geoweeek-2020/>

ANNOUNCEMENTS

Teledyne Optech, a Teledyne Technologies [NYSE:TDY] company, announced they have signed an agreement with Aerial Surveys International (ASI) to sell a Galaxy T2000, upgrade their existing Galaxy Prime to a Galaxy T2000 and install both sensors in the productivity-doubling G2 Sensor System.



This purchase will enhance ASI's capabilities through the effective 2-million point per second PRF of each Galaxy T2000. Moreover, by combining both sensors on the G2 Sensor System, ASI will bolster their capacity to a true, effective 4 million point per second that provides unmatched point density with the highest available efficiency.

The Galaxy T2000 is engineered to point all its 2 million laser shots per second to the ground within a programmable field of view, thereby achieving the highest single-pass point density in the market. With faster scanning at up to 320 lines per second and the smallest laser footprint, the T2000 provides a new, unparalleled level of performance for applications involving small-object identification such as wire detection as well as foliage penetration.

The G2 Sensor System features the unique compact form of the ALTM Galaxy, enabling maximum configuration flexibility with the option to install and operate two sensors as one system into a single aircraft portal. The G2 Sensor System uses the same Galaxy production workflow that processes, calibrates, co-registers and outputs survey-grade LAS files from both sensors simultaneously.

"ASI are taking a leadership position in the airborne mapping industry and making major investments in technology and capacity to be strongly positioned for the future, with the ability to offer unmatched point density with the highest efficiency," said Michel Stanier, Executive Vice President and General Manager of Teledyne Optech.

Find out more at www.teledyneoptech.com.

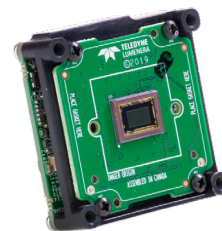
Calibrate Hyperspectral Data with a Spectral Evolution Field Spectroradiometer. SPECTRAL EVOLUTION'S spectrometers and spectroradiometers are single point systems that cover the full VNIR and SWIR spectral range from 350-2500nm. Remote sensing models include the SR-6500, RS-8800, RS-5400, PSR+, and RS-3500. These instruments are designed for field use – rugged design and construction, no moving parts, lightweight and powered by lithiumion batteries. Our instruments deliver better spectral



resolution, signal to noise and spatial resolution capabilities than hyperspectral imaging cameras.

For more information, visit: www.spectralevolution.com

Teledyne Lumenera, a Teledyne Technologies [NYSE:TDY] company, and manufacturer and developer of digital cameras for industrial and scientific imaging applications, is pleased to announce the release of its new Lt Series USB3 Board Level Cameras. Equipped with the latest rolling shutter Starvis™ CMOS sensors and global shutter Pregius™ CMOS sensors from Sony®, and ranging in resolution from 2 - 20 megapixels, these new board level cameras provide flexibility for a wide variety of imaging systems. Teledyne Lumenera's Lt Series Board Level Cameras offer a smaller, lighter, and lower cost imaging solution and are designed specifically to meet the challenges of today's embedded systems.



"The compact design of the new Lt Series Board Level cameras allows for easy integration into imaging systems with small form factors, making them ideal for portable or handheld devices, and compact OEM system designs," said Ghislain Beaupré, General Manager at Teledyne Lumenera.

The Teledyne Lumenera Lt Series Board Level Cameras help ease the vision system design process by eliminating extra camera weight and housing material, making it easier for system designers to integrate these cameras into existing product designs. In addition, a board level camera allows system designers more flexibility around lens options for their imaging application.

Teledyne Lumenera Lt Series Board Level Cameras are engineered to deliver high dynamic range, high speed, with low read noise for applications such as aerial imaging, portable/OEM devices, Intelligent Traffic Systems (ITS), life sciences, and industrial inspection solutions.

For more information about Teledyne Lumenera's Lt Series USB3 Board Level Cameras visit the website.

CALENDAR

- 22-26 June 2020, **ASPRS Geo Week 2020 Technical Program — Virtual**. For more information, visit <http://conferences.asprs.org/geoweek-2020/>.
- 28 January - 4 February 2021, **43rd COSPAR Scientific Assembly**, Sydney, Australia. For more information, visit <https://www.cospar2020.org/>.

FEATURE



333 The Emerging Role of Cubesats for Earth Observation Applications in South Africa

By Paidamwoyo Mhangara, *The University of Witwatersrand*

341 ASPRS Yearbook President's Address, Past-President's Address, and Executive Director's Report

359 Trajectory Drift-Compensated Solution of a Stereo RGB-D Mapping System

Shengjun Tang, Qing Zhu, You Li, Wu Chen, Bo Wu, Renzhong Guo, Xiaoming Li, Chisheng Wang, and Weixi Wang

Multiple sensors are commonly used for three-dimensional (3D)-mapping or robotic-vision applications, as they provide a larger field of view and sufficient observations to fulfill frame-registration and map-updating tasks. However, the data sequences generated by multiple sensors can be inconsistent and contain significant time drift. In this paper, we describe the trajectory drift-compensated strategy that we designed to eliminate the influence of time drift between sensors, remove the inconsistency between the sequences from various sensors, and thereby generate a coarse-to-fine procedure for robust camera-tracking based on two-dimensional-3D observations from stereo sensors.

373 The Geometric Imaging Model for High-Resolution Optical Remote Sensing Satellites Considering Light Aberration and Atmospheric Refraction Errors

Mi Wang, Ying Zhu, Yanli Wang, and Yufeng Cheng

With advances in satellite maneuvering imaging capability, stereoscopic images with large roll and pitch angles can be captured to improve the efficiency of observations. At the same time, the influences of light aberration and atmospheric refraction on image positioning accuracy will be more significant. However, these errors are not accounted for in the traditional imaging and calibration model for optical agile satellites. In this study, the formation mechanisms of the aberration and atmospheric refraction errors in optical remote sensing satellite Earth observation imaging were analyzed quantitatively, and correction models were constructed.

383 Using 250-m MODIS Data for Enhancing Spatiotemporal Fusion by Sparse Representation

Liguo Wang, Xiaoyi Wang, and Qunming Wang

Spatiotemporal fusion is an important technique to solve the problem of incompatibility between the temporal and spatial resolution of remote sensing data. In this article, we studied the fusion of Landsat data with fine spatial resolution but coarse temporal resolution and Moderate Resolution Imaging Spectroradiometer (MODIS) data with coarse spatial resolution but fine temporal resolution.

COLUMNS

347 Mapping Matters

350 GIS Tips & Tricks — Having Options is a Good Thing

351 Grids and Datums

This month we look at the Socialist Republic of Vietnam.

ANNOUNCEMENTS

352 ASPRS Certifications

354 In Memoriam—David C. Smith

355 Headquarters News

356 New ASPRS Members

Join us in welcoming our newest members to ASPRS.

358 *PE&RS* Call for Submissions—Urban Remote Sensing

DEPARTMENTS

330 Industry News

346 Who's Who in ASPRS

357 ASPRS Sustaining Members

See the Cover Description on Page 332

COVER DESCRIPTION

When oceanographer Serge Andréfouet first saw a satellite image of the Great Bahama Bank, he knew the colors and contours were special. He passed the unique image to a colleague, who submitted it to NASA's Earth Observatory (EO) for an Image of the Day in 2002 (top image). Nearly eighteen years later, the image is still much appreciated. In fact, it knocked off more recent satellite imagery to win EO's Tournament Earth 2020.



"There are many nice seagrass and sand patterns worldwide, but none like this anywhere on Earth," said Andréfouet, who is now studying reefs at the Institute for Marine Research & Observation in Indonesia. "I am not surprised it is still a favorite, especially for people who see it for the first time." He said the image has been featured over the years on numerous websites, in books, and even at rave parties.

The varying colors and curves remind us of graceful strokes on a painting, but the features were sculpted by geologic processes and ocean creatures. The Great Bahama Bank was dry land during past ice ages, but it slowly submerged as sea levels rose. Today, the bank is covered by water, though it can be as shallow as two meters (seven feet) deep in places. The bank itself is composed of white carbonate sand and limestone, mainly from the skeletal fragments of corals. The Florida peninsula was built from similar deposits.

Andréfouet's image (above) shows a small section of the bank as it appeared on January 17, 2001, and was acquired by the Enhanced Thematic Mapper Plus (ETM+) on the Landsat 7 satellite (using bands 1-2-3). At that time the instrument's blue channel (band 1) helped distinguish shallow water features better than previous satellite mission.

The wave-shaped ripples in the images are sand on the seafloor. The curves follow the slopes of underwater dunes, which were probably shaped by a fairly strong current near the sea bottom. Sand and seagrass are present in different quantities and at different depths, which gives the image a range of blues and greens. The area appeared largely the same when Landsat 8 passed over on February 15, 2020 (cover image).

The shallow bank quickly drops off into a deep, dark region known as the "Tongue of the Ocean." Diving about 2,000 meters (6,500 feet) deep, the Tongue of the Ocean is home to more than 160 fish and coral species. It lies adjacent to the Andros Island, the largest in the Bahamas and one of the largest fringing reefs in the world. The image to the right was acquired on April 4, 2020, by the Moderate Resolution Imaging Spectroradiometer (MODIS) on NASA's Terra satellite.

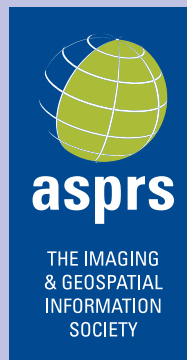


At the time of the 2001 image, researchers did not have a good understanding of the location and distribution of reef systems across the world. Global maps of coral reefs had not changed much since the 19th Century. So researchers turned to satellites for a better view. Andréfouet's image was collected as part of the NASA-funded Millennium Coral Reef Mapping Project, which aimed to image and map coral reefs worldwide. The project gathered more than 1,700 images with Landsat 7, the first Landsat to take images over coastal waters and the open ocean.

Today, many satellites and research programs continue to map and monitor coral reef systems, and marine scientists have a better idea of where the reefs are and how they are faring. Researchers now use reef images and maps in tandem with sea surface temperature data to identify areas vulnerable to coral bleaching.

For more information or to see all three images, visit <https://landsat.visibleearth.nasa.gov/view.php?id=146697>.

NASA Earth Observatory images by Joshua Stevens, using Landsat data from the U.S. Geological Survey, and MODIS data from NASA EOSDIS/LANCE and GIBS/Worldview.2002 imagery courtesy Serge Andrefouet, University of South Florida. Story by Kasha Patel.



PHOTOGRAMMETRIC ENGINEERING & REMOTE SENSING

JOURNAL STAFF

Publisher ASPRS
Editor-In-Chief Alper Yilmaz
Assistant Editor Jie Shan
Assistant Director — Publications Rae Kelley
Electronic Publications Manager/Graphic Artist
Matthew Austin

Photogrammetric Engineering & Remote Sensing is the official journal of the American Society for Photogrammetry and Remote Sensing. It is devoted to the exchange of ideas and information about the applications of photogrammetry, remote sensing, and geographic information systems. The technical activities of the Society are conducted through the following Technical Divisions: Geographic Information Systems, Photogrammetric Applications, Lidar, Primary Data Acquisition, Professional Practice, and Remote Sensing Applications. Additional information on the functioning of the Technical Divisions and the Society can be found in the Yearbook issue of *PE&RS*.

Correspondence relating to all business and editorial matters pertaining to this and other Society publications should be directed to the American Society for Photogrammetry and Remote Sensing, 425 Barlow Place, Suite 210, Bethesda, Maryland 20814-2144, including inquiries, memberships, back issues, changes in address, manuscripts for publication, advertising, subscription issues, and publications. The telephone number of the Society Headquarters is 301-493-0290; the fax number is 225-408-4422; web address is www.asprs.org.

PE&RS. *PE&RS* (ISSN0099-1112) is published monthly by the American Society for Photogrammetry and Remote Sensing, 425 Barlow Place, Suite 210, Bethesda, Maryland 20814-2144. Periodicals postage paid at Bethesda, Maryland and at additional mailing offices.

SUBSCRIPTION. For the 2020 subscription year, ASPRS is offering two options to our *PE&RS* subscribers — an e-Subscription and the print edition. E-subscribers can plus-up their subscriptions with printed copies for a small additional charge. Print and Electronic subscriptions are on a calendar-year basis that runs from January through December. We recommend that customers who choose both e-Subscription and print (e-Subscription + Print) renew on a calendar-year basis.

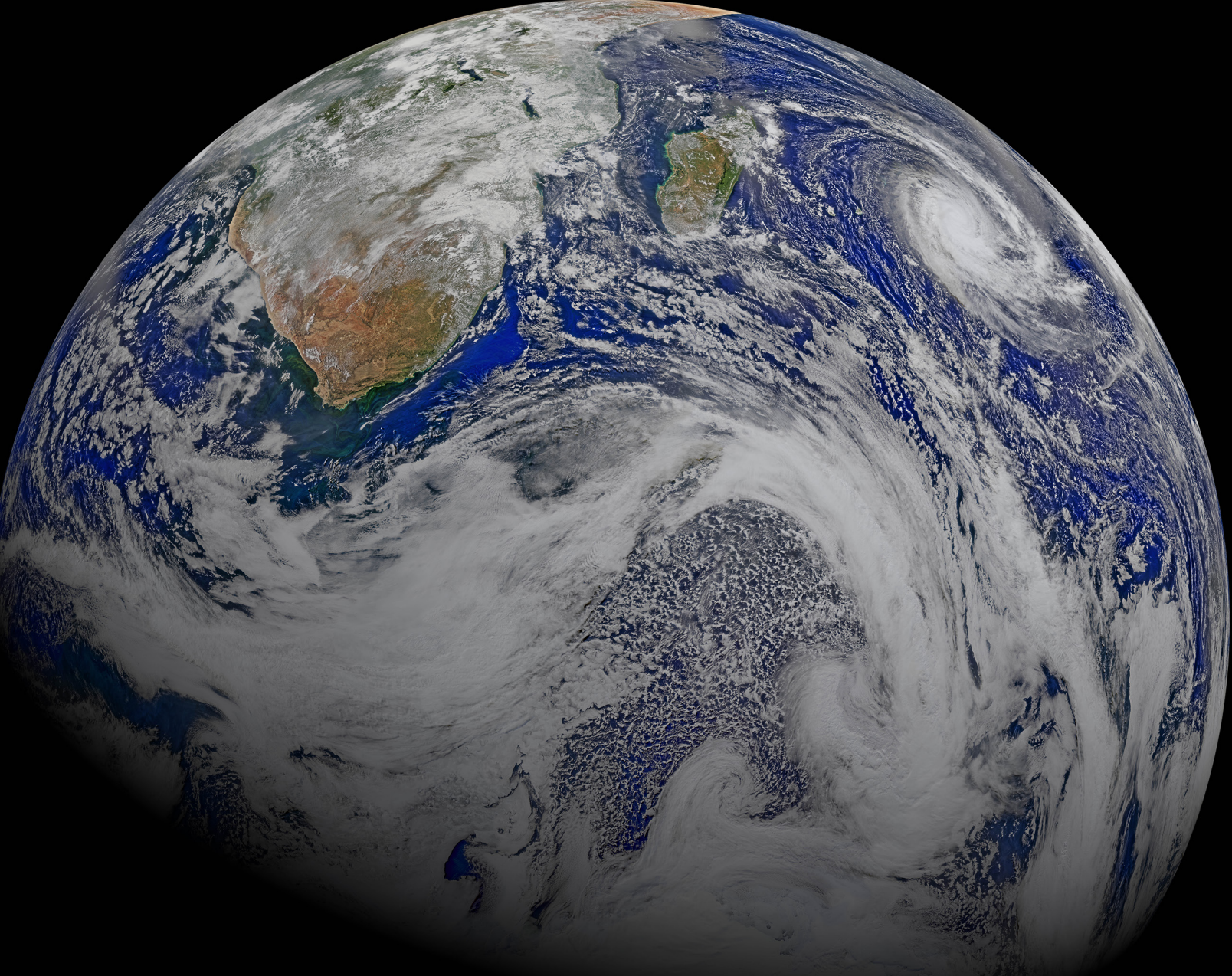
The rate of the e-Subscription (digital) Site License Only for USA and Non-USA is \$1000.00 USD. e-Subscription (digital) Site License Only for Canada* is \$1049.00 USD. e-Subscription (digital) Plus Print for USA is \$1365.00 USD. e-Subscription (digital) Plus Print for Canada* is \$1424.00 USD. e-Subscription (digital) Plus Print for Non-USA is \$1395.00 USD. Printed-Subscription Only for USA is \$1065.00 USD. Printed-Subscription Only for Canada* is \$1124.00 USD. Printed-Subscription Only for Non-USA is \$1195.00 USD. *Note: e-Subscription/Printed-Subscription Only/e-Subscription Plus Print for Canada include 5% of the total amount for Canada's Goods and Services Tax (GST #135123065). **PLEASE NOTE: All Subscription Agencies receive a 20.00 USD discount.**

POSTMASTER. Send address changes to *PE&RS*, ASPRS Headquarters, 425 Barlow Place, Suite 210, Bethesda, Maryland 20814-2144. CDN CPM #40020812

MEMBERSHIP. Membership is open to any person actively engaged in the practice of photogrammetry, photointerpretation, remote sensing and geographic information systems; or who by means of education or profession is interested in the application or development of these arts and sciences. Membership is for one year, with renewal based on the anniversary date of the month joined. Membership Dues include a 12-month electronic subscription to *PE&RS*. Or you can receive the print copy of *PE&RS* Journal which is available to all member types for an additional fee of \$60.00 USD for shipping USA, \$65.00 USD for Canada, or \$75.00 USD for international shipping. Dues for ASPRS Members outside of the U.S. will now be the same as for members residing in the U.S. Annual dues for Regular members (Active Member) is \$150.00 USD; for Student members \$50.00 USD for USA and Canada \$58.00 USD; \$60.00 USD for Other Foreign members. A tax of 5% for Canada's Goods and Service Tax (GST #135123065) is applied to all members residing in Canada.

COPYRIGHT 2020. Copyright by the American Society for Photogrammetry and Remote Sensing. Reproduction of this issue or any part thereof (except short quotations for use in preparing technical and scientific papers) may be made only after obtaining the specific approval of the Managing Editor. The Society is not responsible for any statements made or opinions expressed in technical papers, advertisements, or other portions of this publication. Printed in the United States of America.

PERMISSION TO PHOTOCOPY. The appearance of the code at the bottom of the first page of an article in this journal indicates the copyright owner's consent that copies of the article may be made for personal or internal use or for the personal or internal use of specific clients. This consent is given on the condition, however, that the copier pay the stated per copy fee of 3.00 USD through the Copyright Clearance Center, Inc., 222 Rosewood Drive, Danvers, Massachusetts 01923, for copying beyond that permitted by Sections 107 or 108 of the U.S. Copyright Law. This consent does not extend to other kinds of copying, such as copying for general distribution, for advertising or promotional purposes, for creating new collective works, or for resale.



THE EMERGING ROLE OF CUBESATS FOR EARTH OBSERVATION APPLICATIONS IN SOUTH AFRICA

Paidamwoyo Mhangara, The University of Witwatersrand

Introduction

Cubesats usage is evolving from scientific demonstration and educational platforms to standardized space-borne scientific instruments that support operational earth observation applications (Liebig 2000, Sandau 2010, Woellert et al. 2011, Qiao et al. 2013, Diaz et al. 2016, Kopacz et al. 2020). The effectiveness of Cubesat technology is being attested to globally as nanosatellites are increasingly used to support innovative scientific and operational missions (Rose et al. 2012, Qiao et al. 2013, Xia et al. 2017, Poursanidis et al. 2019). Cubesats have long been recognized as having the potential to be a disruptive force that could replace large conventional earth observation satellites (Southwood 2000, Diaz et al. 2016, Mhangara et al. 2020).

Cubesats have benefited from the accelerated progression towards miniaturization of space-borne satellite platforms and the availability of Commercial-Off-The-Shelf (COTS) components (Woellert et al. 2011, Matandirotya et al. 2013). Small satellites are generally classified into five groups known as Minisatellite (100–500 kg), Microsatellite (10–100 kg), Nanosatellite (1–10 kg), Picosatellite (0.1–1 kg) and Femtosatellite (0.01–0.1 kg) (Sandau 2010, Woellert et al. 2011). Despite their small size, Cubesats are increasingly being considered as ideal platforms for hosting compact earth observation instruments needed to take critical measurements. Conventional earth observation scientific instruments mounted on Cubesats include visible and near-infrared sensors, near-infrared spectrometers, magnetometers, radiometers and short wavelength radars (Liebig 2000, Qiao et al. 2013, Diaz et al. 2016). To date, at least 1200 Cubesats have been launched into low-earth orbit, and this number is predicted to grow (Sandau 2010, Xia et al. 2017).

Cubesats Around the World

Globally, the development of miniaturized satellite platforms has been pioneered by universities (Sandau 2010, Xia et al. 2017). Initially introduced as low-cost space research and engineering projects for university students, Cubesat technology has proliferated in the industry and has been widely adopted by space agencies internationally (Blouvac et al. 2000, Liebig 2000, Southwood 2000). The growth in

Cubesat technology has been augmented by a simultaneous acceleration in technological advancements in nano-, micro-, and miniature technologies in technical fields that include telecommunications, (Opto)electronics, materials, sensors, fluidics, and instrumentation (Woellert et al. 2011, Diaz et al. 2016). This technological wave enabled the development of a variety of miniaturized and novel autonomous instruments and systems to facilitate remote measurements and scientific experiments on a miniaturized platform.

Cubesats have been adopted by space agencies internationally for scientific tests and important scientific missions. Some prominent Cubesat programs include The National Aeronautics and Space Administration's (NASA) CubeSat Launch Initiative program, European Space Agency (ESA)-funded Student Space Exploration and Technology Initiative (SSETI), the National Science Foundation (NSF) initiative in the USA, and the Cubesat Programme at the Cape Peninsula University of Technology's French South African Institute of Technology (F^SATI) whose Cubesats have been funded by the South African National Space Agency (SANSA) (Blouvac et al. 2000, Southwood 2000, Steyn et al. 2013, van Zyl et al. 2013).

Despite their small size, Cubesats are increasingly being considered as ideal platforms for hosting compact earth observation instruments needed to take critical measurements.

The commercial viability of using Cubesats for operational earth observation applications has also gained the attention of private companies (Mhangara et al. 2020). The low capital layout cost, rapid development and related low-risk levels associated with Cubesat platforms are attractive for investors venturing into the space industry. Many academic spin-off companies are being established internationally to develop and integrate Cubesat components and subsystems as well as to provide earth observa-

tion data and downstream products and services (Rose et al. 2012, Xia et al. 2017). A business value chain now exists that is comprised of manufacturers of COTS components, suppliers of Cubesat kits, providers of complete Cubesats, companies for launch services, data vendors and providers for downstream value-added products and services. In a recent market study of the satellite industry, the economic value of Cubesats was \$152 million in 2018, and projected to rise to \$375 million by 2023. The earth observation and traffic monitoring segment constitute a large share of the global Cubesat market (<https://www.marketsandmarkets.com/Market-Reports/cubesat-market-58068326.html>). Prominent earth observation companies that have emerged include Planet Labs, which has a constellation of more than 100 Cubesats in low earth orbit imaging over 250 million km² of the earth's landmass daily. The Planet Labs Cubesat weighs about 5kg and is 10x10x30 centimeters in size.

Cubesats are a feasible way of participating in space-related activities due to their cheap manufacturing costs, low launch

Photogrammetric Engineering & Remote Sensing
Vol. 86, No. 6, June 2020, pp. 333–340.
0099-1112/20/334–340

© 2020 American Society for Photogrammetry
and Remote Sensing
doi: 10.14358/PERS.86.6.333

cost, short development time, small size, light weight, and low power requirements compared to large satellites used in the Landsat satellite missions and Sentinel satellite series (Paules and Luther 2000, Woellert et al. 2011, Diaz et al. 2016). These favorable factors are allowing developing countries to actively participate in satellite development and operations. The potential of Cubesats to accelerate scientific and technological advancement of emerging economies and developing countries has already been articulated (Woellert et al. 2011, Rose et al. 2012). The scholars provide a concise synthesis of the history and a technical overview of Cubesats as well as a synopsis of scientific applications and success stories.

For several decades now, the development of satellites for earth observation applications has been dominated by space-faring nations such as United States, Japan, India, Russia, European Union countries, Japan, Canada and lately China and Brazil (Woellert et al. 2011). Despite the well-established scientific and socio-economic benefits of earth observation, the capital-intensive nature and engineering complexity of conventional satellite building programs limited developing countries in constructing their own satellites. The advent of Cubesats have lowered the barrier to entry for less developed countries and has provided them with an invaluable opportunity to launch space programs. (van Zyl. 2011, Rose et al. 2012, Ngcofe and Gottschalk 2013) The development of Cubesats accompanies some of the achievements by African countries with emerging space capabilities in small satellites such as Algeria, Egypt, Nigeria and South Africa. In Africa, there is growing interest from universities, governments, space agencies and commercial companies to develop small satellites to support earth observation applications (van Zyl. 2011, Steyn et al. 2013, van Zyl et al. 2013). The low development and launch costs associated with small satellites have spurred developing African nations such as South Africa, Nigeria, Egypt, Ghana, Kenya, Algeria and Zimbabwe to launch space programs aimed at advancing technological innovation in space (Ngcofe and Gottschalk 2013, Oyewole 2017). While some studies have focused on the growth of space technology in various countries, little focus has been placed on the evolving role of Cubesats in South Africa.

Development of Cubesats in South Africa

Early Development

While the evolution of Cubesats in South Africa accelerated with the technological forces towards miniaturization of satellites and electronic systems, the growth was also spurred by the country's preceding satellite engineering capability

(Gottschalk 2010, Ngcofe and Gottschalk 2013, Steyn et al. 2013, van Zyl et al. 2013). South Africa has a long history in space science and technology that dates back to the emergence of the space era. The country's heritage in space technology can be traced as far back as the 1950's when it was involved in amateur rocket launches.

In a review of South Africa's space program, Gottschalk (Gottschalk 2010) divides the evolution of the country's space initiative into three epochs. The first phase was from 1947-1962 and was named the age of amateurs. The apartheid government led the second phase called the military era from 1963-1993. This era involved the development of a secret military space launcher program targeted at developing reconnaissance satellites. While the period didn't produce a flight-ready satellite, South Africa developed a comprehensive space infrastructure that included satellite testing, site design and a coastal launch facility with telemetry capacity.

The third phase, named the civilian era, emerged after the country became democratic in 1994. During this period, the country established several legal instruments and policies to regulate space activities and developed institutions and structures to coordinate them. Some of the space laws implemented include the Space Affairs Act 84 of 1993, Space Affairs Amendment Act 64 of 1995 and the South African National Space Agency Act 36 of 2008. Prominent institutions and councils set up include the South Africa National Space Agency (SANSA) and the Space Affairs Council of South Africa (SACSA) (Gottschalk 2010, Ngcofe and Gottschalk 2013, Steyn et al. 2013).

The advent of Cubesats have lowered the barrier to entry for less developed countries and has provided them with an invaluable opportunity to launch space programs.

Launched in February 1999, the SUNSAT microsatellite was the first South African satellite that went into orbit. Built by the University of Stellenbosch, the microsatellite project started in 1992 to develop satellite engineering skills for use by the space industry in the country (Steyn et al. 2013). The satellite weighed 64kg and carried a pushbroom multispectral imager with three spectral bands at a ground sampling distance of 15m. SUNSAT had a mission life of two years. In September 2009 a second microsatellite known as Sumbandisat was launched and operated until August 2011. Sumbandilasat carried a pushbroom multispectral imager with six spectral bands capturing data at a ground sampling distance of 6.25m.

University Involvement

In South Africa, the thrust of the development of Cubesats was aimed at education and training, technology demonstration, space weather research and earth observation (van Zyl 2011, van Zyl et al. 2013, Zaidi et al. 2018). The low investment costs involved in developing Cubesats makes

them perfect candidates for education and training, particularly for student research groups. The F'SATI program at the Cape Peninsula University of Technology is a postgraduate program in satellite systems engineering that focuses on the development of Cubesats. This initiative enabled students to acquire hands-on technical skills in satellite engineering and to undertake innovative research in the development of Cubesats. The program was funded by the Department of Science and Innovation (DSI), the National Research Foundation (NRF) and the South African National Space Agency.

Three Cubesats have been successfully launched from the program to date, including ZACube-01 and ZACube-02. ZACube-1 is an 1U Cubesat ("U" refers to a 100x100x-113.5mm cube) that carries an HF beacon transmitter for ionospheric tomography as its primary payload for monitoring space weather. The payload was developed jointly with scientists at SANSA Science in Hermanus and consists of a simple radio transmitter. It emits a 14 MHz beacon signal received on the ground to characterize the electron density for the zone of the ionosphere traversed by the Cubesat. The data was used to validate and improve the International Reference Ionosphere model and to characterize the ionospheric radar for the Super Dual Auroral Radar Network (SuperDARN) (van Zyl et al. 2013). ZACube-01 also carries onboard a very low-resolution camera to capture pictures of the earth. Launched on December 27, 2018, ZACube-2 is a 3U Cubesat carrying an automatic identification system (AIS) as its primary payload and an additional ocean color and fire detection imager (Zaidi and van Zyl 2017, Zaidi et al. 2018). The K-line and reference infrared camera channels constitute a secondary payload. The AIS is used for detecting and tracking ship movement in the South African territorial waters in support of maritime domain awareness. The K-line and reference camera channels are used for wildfire detection and monitoring.

Recent Activities

In 2017, two South African Cubesats, ZA-AeroSat and nSight-1 were launched from the International Space Station (ISS) as part of ESA's QB50 project for upper tropospheric modeling research. ZA-AeroSat 3U Cubesat was jointly developed by Stellenbosch University, Cape Peninsula University of Technology and CubeSpace. The satellite was used to showcase passive Cubesat aerodynamic stabilization using its four communication antennas as aerodynamic feathers, but the Cubesat was only semi-operational due to weak signal issues.

nSight-1 is a 2Us Cubesat built by a private South African company, Space Commercial Services. It carries onboard IPEX (Flux-Φ-Probe Experiment) scientific instrument that collects atmospheric oxygen data in the lower thermosphere. nSight-1 also carries an additional RGB (Red, Green and Blue) multispectral earth observation imager as a secondary payload that captures images to support remote sensing applications (Mhangara et al. 2020).

The maturity of Cubesats as a space platform to support operational earth observation data has gained the attention of the South African space industry. The last decade has witnessed an increased number of South African companies participating in the development of Cubesats, namely Space Commercial Service, NewSpace Systems, Simera Technology Group, CubeSpace, Spaceteq and Amaya. Most of the companies are collaborating with universities that have satellite engineering capability, such as Cape Peninsula University of Technology and Stellenbosch University, as innovation partners.

Emerging Cubesat Remote Sensing Applications

Cubesats are progressively transforming the space science and technology landscape in South Africa. The four South African Cubesats launched in the last decade demonstrate the feasibility of using nanosatellites as operational platforms to support earth observation applications for socio-economic benefit. It is evident from the review of the Cubesats that imagers were only added as secondary payloads piggy-backing on funded scientific experiments that were the primary missions. An analysis of the images produced by nSight-1 nanosatellite and the infrared imager in ZACube-2 shows the feasibility of using Cubesats for operational remote sensing applications as a means of complementing data from current missions such as Landsat 8 and Sentinel-2.

In a recent study, Mhangara et al. (2020) analyzed nSight-1 and observed that the images are valuable for a multitude of remote sensing applications. Some of the identified uses included geological mapping, geomorphological analysis, extraction of surface water bodies, agricultural field demarcation and crop mapping, ship detection, vegetation assessments, differentiation of urbanized areas and other land use and land cover applications. The visual interpretation of nSight-1 imagery showed the images were suitable for a range of applications. Land use and land cover types discernable from nSight-1 imagery include agricultural fields, surface water bodies and geomorphological and structural geology features as illustrated in Figure 1, Figure 2 and Figure 3, respectively.

The infrared sensor onboard ZACube-2 is an invaluable tool for fire monitoring. The novelty of this imager is that it is capable of detecting the characteristic potassium spectral emissions of burning vegetation biomass using the near-infrared spectral channel and is valuable in identifying ocean color. Figure 4 displays an infrared image acquired by this sensor.

The practical value of the automatic identification system onboard ZACube-2 is maritime surveillance. AIS data from ZACube-2 is already being used for ocean vessel detection in South African Exclusive Economic Zone (EEZ) in support of a government oceans economy program known as Operations



Figure 1: nSight-1 Image: Agricultural fields in Delano, California, USA (Mhangara et al. 2020 and Credits: SCS).

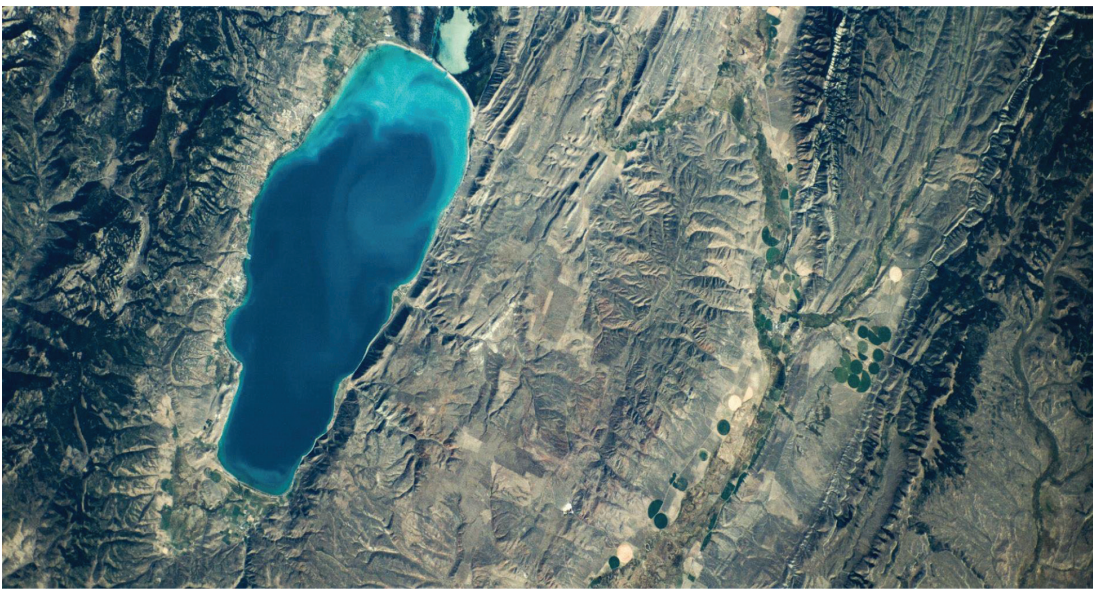


Figure 2: nSight-1 Image: Water Resources and Agriculture at Bear Lake, Utah, USA (Mhangara et al. 2020 and Credits: SCS).

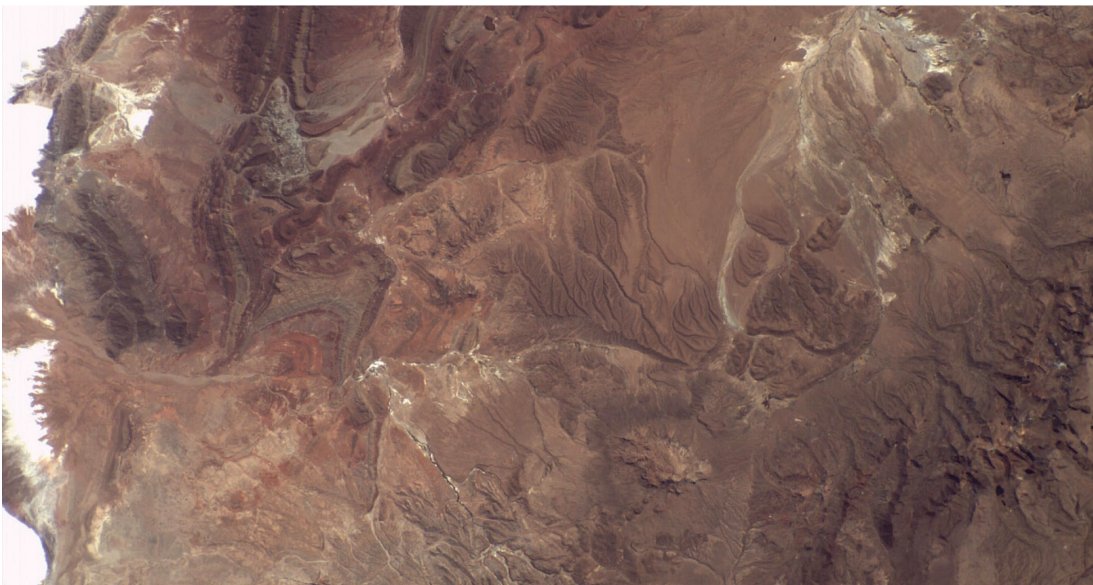


Figure 3: nSight-1 Image: Geomorphological features and structural geology in Salar de Uyuni, Bolivia (Mhangara et al. 2020 and Credits: SCS).



Figure 4. ZACube-2. NIR image over Voëlvelei Dam, Western Cape, South Africa from the K-line sensor (Credits: CPUT).

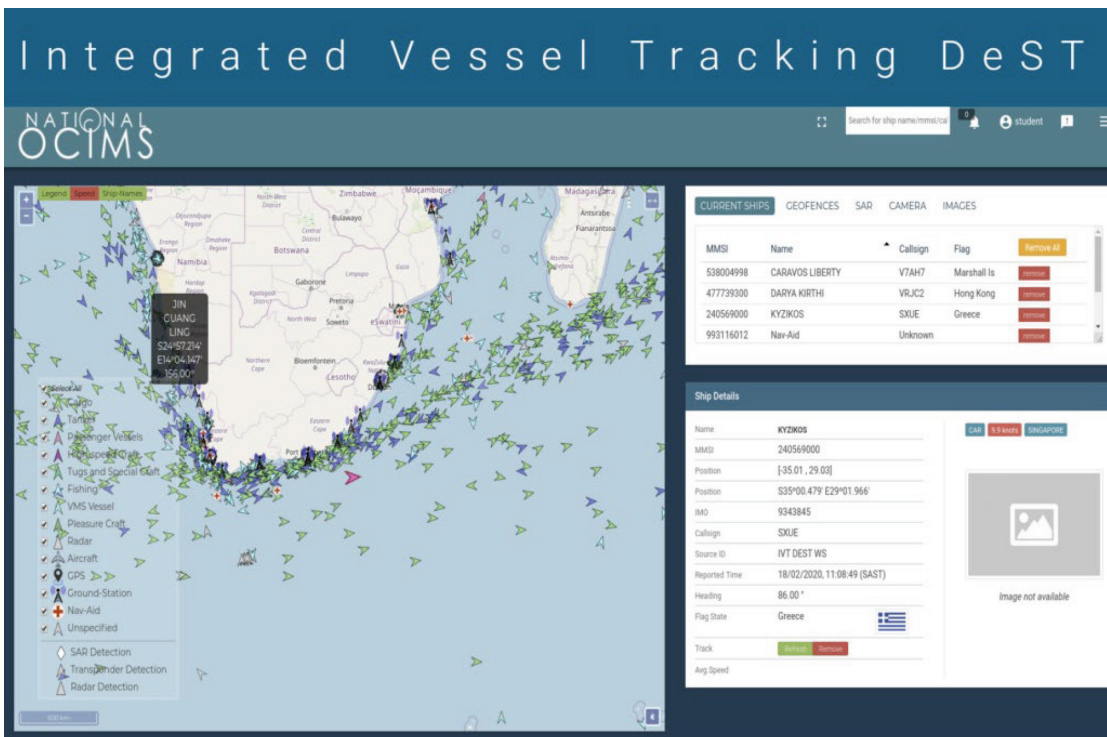


Figure 5: Integrated Vessel Tracking system that uses AIS data from ZA-CUBE 2. <https://www.ocims.gov.za/integrated-vessel-tracking-tool/>.

Phakisa. The AIS data augments the Radarsat-2 synthetic aperture radar (SAR) satellite data used for monitoring illegal vessels along the coastline and the broader EEZ. AIS also feeds into the Integrated Vessel Tracking Tool in the National Oceans and Coastal Information Management System (OCIMS). Illegal fishing vessels are notoriously known for turning off their AIS transponders during unlawful fishing operations. The AIS data is fed into the Integrated Vessel Tracking Tool shown in Figure 5 to track the movement of vessels using transponder information (such as AIS) and sends out notifications when ships encroach into Marine Protected Areas (MPAs).

The success of the ZACube-2 has prompted the Department of Science and Innovation in South Africa to provide funding for two additional Cubesats, one devoted to maritime surveillance and the other for fire monitoring with the ultimate objective of having a constellation of nine nanosatellites (<https://www.itweb.co.za/content/kLgB1MeJPNGq59N4>). Similarly, the success of nSight-1 compelled SCS to develop a follow-up compact Cubesat imager known as the Chameleon (<http://scs-space.com/payloads/chameleon/>).

Discussion

The capability demonstrated by nSight-1 and ZACube-2 nanosatellites in acquiring satellite imagery indicates that Cubesats can play a meaningful role in supporting operational remote sensing applications. Mhangara et al. (2020) analyzed a variety of nSight-1 imagery and concluded that the imagery is capable of supporting several remote sensing applications, including agricultural field mapping, surface water body mapping, soil erosion and other geomorphological assessments, wetlands mapping, urban demarcation, land cover and land use mapping, and a wide range of cartographic applications. The infrared imagery from the ZACube-2 K-line Sensor shows some potential for vegetation mapping, fire detection and wetland assessment. ZACube-2 has shown the remarkable capability to consistently supply AIS data to support the operational tracking of illegal vessels in the South African EEZ.

Lack of onboard radiometric calibration functionality on most Cubesats is a deficiency of current nanosatellites. Cross-calibration with other well-calibrated satellite missions could be used to address this shortcoming. The ability of the nanosatellites to provide reliable and consistent data services is an essential user requirement. This aspect could not be ascertained due to the experimental and short-term nature of the launched nanosatellites. It can, however, be argued that the success of Planet Labs Cubesats provides sufficient evidence of the potential mission life of Cubesats.

The emerging applications for nanosatellites in South Africa are consistent with global trends. A review of remote sensing applications using data from Cubesats is indicative of the pervasive nature of nanosatellites. McCabe et al. (2017) showcased the use of Cubesats in hydrology, especially in assessing vegetation dynamics and terrestrial evaporation. The utility of Cubesats for crop monitoring has been elaborated by many scholars (Houborg and McCabe 2018, Mhangara et al. 2020). Quite recently, Santilli et al. (2016) highlighted that a constellation of Cubesats is capable of supplying timely satellite data in disaster situations due to the more frequent revisiting of disaster areas. The ability of Cubesats to monitor temporal surface water changes was demonstrated by Cooley et al. (2019). Using high-resolution Cubesat imagery, Cooley et al. (2019) detected the daily changes in Arctic-Boreal Lake Dynamics. Houborg and McCabe (2018) demonstrated the feasibility of using Cubesat data to derive vegetation indices such as the Normalized Difference Vegetation Index and Leaf Area Index for crop and general vegetation monitoring. Recently, Poursanidis et al. (2019) demonstrated the utility of Cubesats to derive bathymetric measurements in coastal areas. The feasibility of using Cubesats for global mesopause temperature sensing in support of climate monitoring has been shown by Doe and Watchorn using the Climate Monitoring Cubesat Mission (CM2). The use of Cubesats as platforms for GNSS remote sensing and navigation has been explored by Qiao et al. (2013).

In general, our review suggests that remote sensing data applications undertaken by Cubesats cross the entire spectrum of the earth observation Societal Benefit Areas (SBAs) outlined by the Group on Earth Observation (GEO). Earth Observation SBAs include biodiversity and ecosystem sustainability, disaster resilience, energy and mineral resource management, food security and sustainable agriculture, infrastructure and transportation management, public health surveillance, sustainable urban development and water resources management (<https://www.earthobservations.org/sbas.php>).

Conclusion

Cubesats are increasingly being used worldwide as educational platforms for training, as a means to demonstrate engineering capability, and as hosts for scientific space-related experiments at low cost. Some of the favorable factors driving the growth in the development of Cubesats include the small size of Cubesats, short development time, access to COTS components and cheap launch costs compared to large satellite missions. In South Africa, while Cubesats were initially aimed as training tools for satellite engineering students at universities, the technology is reaching maturity and being deployed for operational applications. The growth areas for Cubesats include earth observation, surveillance, space weather monitoring, meteorology and telecommunications. A review of earth observation applications articulated in this paper suggests that Cubesats could be used to support a wide range of remote sensing applications to complement the data services offered by prominent missions such as the Landsat and Sentinel series of satellites.

The quality of imagery produced by nSight-1 and ZACubesat-2 is adequate to fulfil a myriad of cartographic and monitoring applications. nSight-1 has shown a capability to map agricultural fields, surface water resources, land degradations and other geomorphological processes. Similarly, the K-Line Infrared Sensor onboard ZACubesat-2 has collected imagery that can be used for fire monitoring, vegetation delineation and detection of wetlands. The ability of the AIS instrument onboard Cube-2 to monitor illegal vessels in the South African oceanic EEZ has been successfully demonstrated. The emergence and growth of small enterprises involved in the manufacturing and component supply chain of Cubesats testify that Cubesat technology is reaching maturity for deployment for operational purposes. In addition, in the last decade, one of the greatest success of Cubesats in South Africa has been for the postgraduate training of satellite engineering students at universities.

References

- Blouvac, J., B. Lazard, and J. M. Martinuzzi. 2000. CNES small satellites earth observation scientific future missions. *Acta Astronautica* 46:75–79.
- Cooley, S. W., L. C. Smith, J. C. Ryan, L. H. Pitcher, and T.

- M. Pavelsky. 2019. Arctic-Boreal Lake Dynamics Revealed Using CubeSat Imagery. *Geophysical Research Letters* 46:2111–2120.
- Diaz, M. A., J. C. Zagal, C. Falcon, M. Stepanova, J. A. Valdivia, M. Martinez-Ledesma, J. Diaz-Peña, F. R. Jaramillo, N. Romanova, E. Pacheco, M. Milla, M. Orchard, J. Silva, and F. P. Mena. 2016. New opportunities offered by Cubesats for space research in Latin America: The SUCHAI project case. *Advances in Space Research* 58:2134–2147.
- Doe, R.A. and Watchorn, S., 2011, September. Climate-monitoring CubeSat mission (CM2): a project for global mesopause temperature sensing. In *Earth Observing Systems XVI* (Vol. 8153, p. 81530Q). International Society for Optics and Photonics.
- Gottschalk, K. 2010. South Africa's space program. *Astropolitics* 8:35–48.
- Houborg, R., and M. F. McCabe. 2018. Daily retrieval of NDVI and LAI at 3 m resolution via the fusion of CubeSat, Landsat, and MODIS data. *Remote Sensing* 10.
- Kopacz, J. R., R. Herschitz, and J. Roney. 2020. Small satellites an overview and assessment. *Acta Astronautica* 170:93–105.
- Liebig, V. 2000. Small satellites for earth observation - the German small satellite programme. *Acta Astronautica* 46:81–86.
- Matandirotya, E., R. R. V. Zyl, D. J. Gouws, and E. F. Saunderson. 2013. Evaluation of a Commercial-Off-the-Shelf Fluxgate Magnetometer for CubeSat Space Magnetometry. *Journal of Small Satellites* 2:133–146.
- McCabe, M. F., B. Aragon, R. Houborg, and J. Mascaro. 2017. CubeSats in Hydrology: Ultrahigh-Resolution Insights Into Vegetation Dynamics and Terrestrial Evaporation. *Water Resources Research* 53:10017–10024.
- Mhangara, P., W. Mapurisa, and N. Mudau. 2020. *Image Interpretability of nSight-1 Nanosatellite Imagery for Remote Sensing Applications*.
- Ngcofe, L., and K. Gottschalk. 2013. The growth of space science in African countries for Earth observation in the 21st century. *South African Journal of Science* 109:1–5.
- Oyewole, S. 2017. Space research and development in Africa. *Astropolitics* 15:185–208.
- Paules, G. and Luther, M., 2000. NASA's Earth science program—increasing science opportunity and payoff through small satellites. *Acta Astronautica*, 46(2-6), pp.61-64.
- Poursanidis, D., D. Traganos, N. Chrysoulakis, and P. Reinartz. 2019. Cubesats allow high spatiotemporal estimates of satellite-derived bathymetry. *Remote Sensing* 11.
- Qiao, L., E. Glennon, A. G. Dempster, and S. Chaoui. 2013. Using cubesats as platforms for remote sensing with satellite navigation signals. *International Geoscience and Remote Sensing Symposium (IGARSS)*:852–855.
- Rose, R., J. Dickinson, and A. Ridley. 2012. CubeSats to NanoSats; bridging the gap between educational tools and science workhorses. *IEEE Aerospace Conference Proceedings*:1–11.
- Sandau, R. 2010. Status and trends of small satellite missions for Earth observation. *Acta Astronautica* 66:1–12.
- Santilli, G., C. Cappelletti, S. Battistini, and C. Vendittozzi. 2016. Disaster management of remote areas by constellation of CubeSats. *Proceedings of the International Astronautical Congress, IAC*:26–30.
- Southwood, D. J. 2000. Future ESA earth-observation strategy and ESA's 'living planet' programme. *Acta Astronautica* 46:55–60.
- Steyn, W. H., R. Van Zyl, M. Inggs, and P. J. Cilliers. 2013. Current and future small satellite projects in South Africa. *International Geoscience and Remote Sensing Symposium (IGARSS)*:1294–1297.
- Woellert, K., P. Ehrenfreund, A. J. Ricco, and H. Hertzfeld. 2011. Cubesats: Cost-effective science and technology platforms for emerging and developing nations. *Advances in Space Research* 47:663–684.
- Xia, X., G. Sun, K. Zhang, S. Wu, T. Wang, L. Xia, and S. Liu. 2017. NanoSats/CubeSats ADCS survey. *Proceedings of the 29th Chinese Control and Decision Conference, CCDC* 2017:5151–5158.
- Zaidi, Y., R. R. van Zyl, and N. G. Fitz-Coy. 2018. A GMSK VHF-uplink/UHF-downlink transceiver for the CubeSat missions: Thermo-functional performance. *CEAS Space Journal* 10:453–467.
- Zaidi, Y., and R. Van Zyl. 2017. A low cost testbed and test-design methodology for nanosatellite sub-/systems. *2017 IEEE AFRICON: Science, Technology and Innovation for Africa, AFRICON* 2017:416–423.
- van Zyl, R. R., D. F. Visser, P. J. Cilliers, and B. D. L. Opperman. 2013. ZACUBE-1 space weather mission: Characterize the superDARN HF radar antenna array at SANAE-IV. *Space Weather* 11:52–54.
- van Zyl, R. R. 2011. *CubeSats – a 21st century revolution*.

Author

Paida Mhangara, paida.mhangara@wits.ac.za, is Head of School of Geography, Archaeology and Environment Studies at the University of the Witwatersrand in Johannesburg, South Africa. Paida previously worked as Earth Observation Manager for Research and Applications Development at the South African National Space Agency until October 2019. Mhangara is a professional geospatial scientist and holds a PhD in Environmental Geography with a specialization in remote sensing, MSc in Geographical Information Systems and an MBA degree with an emphasis in Strategic Planning. Over the last fifteen years Paida led the implementation of several earth observation projects in South Africa and taught remote sensing and GIS courses at undergraduate and postgraduate level. He is a member of the Landsat Technical Working Group led by the USGS and has contributed to the Committee of Earth Observation Satellites (CEOS) initiatives.

Cover image courtesy of NASA.

The President's Address was given during the 2020 ASPRS Annual Conference. The conference was presented online during the week of March 23, 2020.

Hello, my name is Jeff Lovin and I am the incoming president of the American Society for Photogrammetry and Remote Sensing for 2020. I want to express how grateful I am to be able to serve this organization in this capacity. When I reflect on the list of individuals who have served ASPRS as president over the last 86 years, starting with the names we all know—Colonel Birdseye, Talbert Abrams, John Davidson, Harry Kelsh, Frank Moffitt—to the more recent names that have had an influence on my career—like Mike Renslow, Terry Keating, Kass Green, Carolyn Merry and many others—I am quite humbled to be listed among these individuals. I count it as a great privilege to lead this organization in this capacity.

I would like to express my gratitude to Tommy Jordan for his leadership over the past year, and for his gracious help and guidance over the last two years as I served under him on the board. I want to thank our board for their hard work and dedication, especially over the last several weeks. I also want to thank our staff, including Matt Austin, Rae Kelley, Brenna LeMaire with our association management firm, Jesse Winch our executive director, and lastly an individual who puts in more hours and passion than any of us, our managing director, Karen Schuckman.

Since I was elected vice president a couple of years ago, I have had several of people say to me, “Hey, I hear you are stepping up to lead ASPRS. That’s great, but it is so sad to hear what has happened to the organization,” while others have asked, “Is ASPRS going to survive?” The message I want to get out to our membership today is yes, we have had some tragic and devastating changes to our leadership, we endured the challenges all professional organizations faced through the Great Recession, and now I guess we can add a global pandemic to the list. In spite of all that, I can proudly say we are not only surviving, we are doing well as an organization. As Tommy noted in his speech, things are truly looking very positive for our organization.

- We have stabilized our finances and are paying back region loans.
- We have hired an association management firm, which is saving us money while providing a higher level of service to our members.
- We are overhauling our website and enhancing our social media presence.
- We are developing online education resources, which are proving pretty timely right now. Anne Hillyer is

leading that charge for us and doing a tremendous job.

- We are growing. In 2019, we had 82 new applicants for certification. It thrills me to know we have that many new professionals joining our field.

So, my challenge to my peers and to all of those who have pulled back or have been in a “wait-and-see” mode: I implore you to re-engage and get involved. We need your time, your money and your talent, and I would argue that ASPRS is well worth the investment. Whether it is renewing as a sustaining member or just renewing your individual membership, it matters. So please, step up and get involved. I am sure if you reach out to anyone on the board or on our staff, there is something you can help with our get involved in within the organization.

A lot of involvement starts at the region level. As Tommy said, Lorraine Amenda has worked tirelessly on the regions, consolidating and realigning. Personally, I first served on the Eastern Great Lakes Region board and then as president there before I got involved at the national level. Healthy regions are key to our sustained health as an organization, so please get involved with your local region.

In my own firm, we have several people involved in the organization beyond myself. Joe Cantz has led the Sustaining Members Council; as you heard from Tommy, Mike Zoltek has taken over the certification program; and Qassim Abdullah has put on workshops for many years. I don’t say all that to brag about my team, I say it to show you that I am not asking anything of you and your organization that I am not doing myself—giving back to a profession that has been very good to me and many of you, and helping others do the same.

This also brings to mind our Rising Stars program, which started under Anne Hillyer’s presidency and is led by Becky Morton. This program provides a way for you to promote the up-and-coming individuals within your organization, exposing them to the professional world. As always, it is the next generation that will carry this organization forward.

Besides a call to re-engage, what are the goals of my presidency?

- I want to continue to improve the level of service we provide to our members. So if you have ideas, let me know—I want to hear them.

- I want to reaffirm ASPRS' role in the industry. For the past few years, we have been internally focused, righting the ship and getting things back on track. That was the right thing to do.

Now, just as I asked you to re-engage with ASPRS, it is also time for ASPRS to re-engage with the professional geospatial community. Over the next year, I want to make sure we are at the table with key geospatial organizations, such as AUVSI, USGIF, USGEO and MAPPS. Each of these organizations serve a niche role in the geospatial community and so do we. I feel our niche is education, certification and specifications. These are important to the entire industry, and we need to own them. We need to be the go-to organization for these three key things.

Take AUVSI for example, I just ended a three-year term on their board of directors and, just before I left, we completed an in-depth membership survey. We found the fastest growing segment of their membership is the survey and mapping community. We need to offer our educational and certification programs to their members as

we partner with them. I am going to spend a great deal of my time as president making sure ASPRS is back at the forefront of the geospatial landscape.

These are truly exciting times to be a part of this organization. I thank you again for this great honor to serve as your president for 2020.

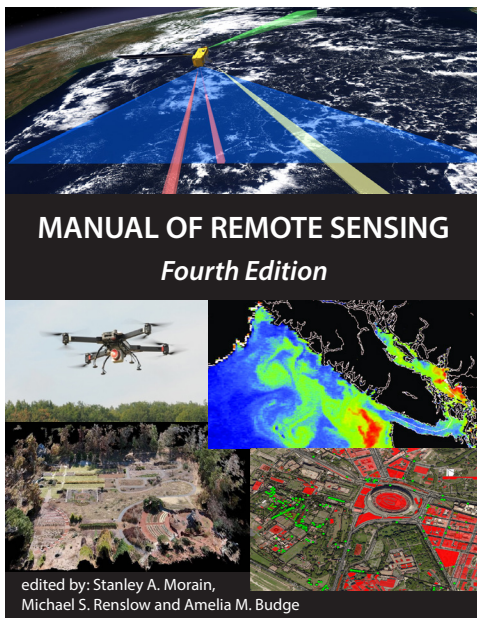
Thank you!



Jeff Lovin, Senior Vice President, Director of Government Solutions at Woolpert, 2020 ASPRS President.

NOW AVAILABLE!

ASPRS Announces the 4th Edition of the *Manual of Remote Sensing*!



The *Manual of Remote Sensing, 4th Ed.* (MRS-4) is an “enhanced” electronic publication available online from ASPRS. This edition expands its scope from previous editions, focusing on new and updated material since the turn of the 21st Century. Stanley Morain (Editor-in-Chief), and co-editors Michael Renslow and Amelia Budge have compiled material provided by numerous contributors who are experts in various aspects of remote sensing technologies, data preservation practices, data access mechanisms, data processing and modeling techniques, societal benefits, and legal aspects such as space policies and space law. These topics are organized into nine chapters. MRS4 is unique from previous editions in that it is a “living” document that can be updated easily in years to come as new technologies and practices evolve. It also is designed to include animated illustrations and videos to further enhance the reader’s experience.

MRS-4 is available to ASPRS Members as a member benefit or can be purchased by non-members. To access MRS-4, visit <https://my.asprs.org/mrs4>.



The Past-President's Address was given during the 2020 ASPRS Annual Conference. The conference was presented online during the week of March 23, 2020.

Hello, for those of you who don't know me, I am Tommy Jordan and I have served as President of The American Society for Photogrammetry and Remote Sensing for the past year. It's a beautiful Spring day here in Georgia and I am here in my front yard to report on the activities and initiatives that we have undertaken as a Society during my term.

We have had a good, productive year since Anne Hillyer handed me the gavel last January in Denver. I thought that I would be delivering this address from the stage in Washington DC at the GeoWeek conference but here I am instead – self-quarantined in Athens, Georgia. I'll still talk about all that we have accomplished but first we need to talk about the impact the Coronavirus pandemic has had on GeoWeek. And I want to emphasize the resilience and creativity shown by the ASPRS leadership in these uncertain times.

Following several weeks of deliberation, the entire GeoWeek conference was rightly postponed due to concerns about the Coronavirus. But what could have been a real tragedy and financial disaster for ASPRS may well turn out to be OK as a result of the timely decisions we have made and the actions we have taken to remediate the effects of postponing this conference. Much of the organizing effort for this decision was done under the leadership of ASPRS Managing Director Karen Schuckman, who worked with DivCom and the ASPRS Officers and Board of Directors to explore a range of alternatives. The final plan was to hold many of the meetings and workshops virtually using the Zoom meeting platform and to postpone the entire technical session until the rescheduled conference.

We were able to hold our committee meetings and the Board Meeting according to the original planned schedule – but instead of meeting face-to-face, we met in the virtual environment. Since we meet regularly using Zoom, this was not difficult or even a hardship, aside from the fact that we all enjoy seeing one another and socializing during these conferences. Unfortunately, awards and scholarships will not formally be presented during our annual business meeting as usual but will instead be mailed to the recipients. The Awards Program will be published in its entirety in the May issue of PERS so that the recipients will be granted the public recognition they deserve. Finally, new officers and board members will be sworn in during a separate virtual meeting.

This week and next we will be presenting most of our workshops online according to a modified schedule that eliminates concurrent workshop sessions. We reached out to the workshop presenters and participants and our proposal to hold these training sessions online was enthusiastically embraced. We will be recording each of the sessions and hope to be able to jump start our new online education program using these materials.

As many of you know, ASPRS has gone through some trying times in recent years. Today, I am pleased to tell you that we have spent the last two full years working on these challenges and we are now on a solid footing for continued growth.

Throughout the past year, we have continued to revise many of our operational methods and procedures to streamline our business operations and cut costs. Significantly, we have hired the P&N Association Management Company to take over business services that had previously been subcontracted out. These services are now fully integrated into our operations and include such functions as membership and certification management, accounts receivables, web and IT services and communications. Bringing P&N aboard has resulted in a positive difference in efficiency and cost-savings to our overall operation. This is a good thing by any measure.

For various reasons, a financial review of ASPRS accounts had not been conducted for several years. Consequently, we had a full review of our income and expenditures performed last year so that the P&N accountants could start working with a clean slate and organized books. Moving forward, they will be able to provide us with monthly and annual financial statements which will enable us to better understand and manage our income streams and expenses.

We also have had several changes at ASPRS headquarters, the most significant of which is the resignation of long-time employee Priscilla Weeks. We have eliminated all subcontractors - thanks to our work with P&N – leaving us with four paid staff members. And because of our overall cost savings, this year we were able to give the staff members merit raises in addition to cost-of-living adjustments. Finally, about half of our office space was renovated and remodeled last year and temporarily leased to BrightView Senior Living. This has produced enough rental income for ASPRS to cover our monthly condominium fees for the past year.

Under the leadership of Lorraine Amenda, we have revitalized the Region Officers Council and reorganized several of the lower performing Regions by merging them with adjacent regions. These changes resulted in the dissolution of the New England and Intermountain Regions, the renaming the Central New York Region to Northeastern Region and the creation of the Cascadia Region. The regions are exploring teaming opportunities with Sustaining Member Firms and, perhaps, most significantly, a monthly, very well attended telecon has been implemented as a forum for the various Region officers to bounce ideas off each other and to work together in other ways.

We have been developing ways to diversify and increase our income streams. To this end, we have completely overhauled and automated our Certification Program thanks to efforts by Mike Zoltek, Jesse Winch and Brenna LeMaire of P&N. Virtually all of the application and review processes are on-line, and a goal is being met to limit the processing time to two months per application. Our efforts to become the 'place to go' for geospatial certification are succeeding in that we have had 82 new certification applications in the past year and our periodic certification review workshops typically sell out. This is a service that we can continue to expand upon and become the industry leaders in.

We also have initiated an online education program that will provide training for ASPRS members and other members of the mapping community. We will also publish workshops and webinars and provide on-line testing capabilities which could be used to further streamline the Certification process. This is another major step towards our goal of being the provider of high-quality geospatial training opportunities.

Finally, I would like to talk a bit about the International Society for Photogrammetry and Remote Sensing or ISPRS. The ASPRS is classified as an Ordinary Member of ISPRS, meaning that we represent the United States in this international body. We have long been involved with ISPRS with several of our members holding important positions in the Society. Over the past year, we have continued to strengthen our relationship with ISPRS. Moving forward, we will be publishing our conference proceedings in the ISPRS Archives so that the papers can be readily available and searchable on the internet. Manuscripts from the recent Pecora conference are already available on the ISPRS website and GeoWeek papers will be made available soon after the conference. We have also initiated a bid to host the XXV ISPRS Congress in Denver in 2024. This is a huge undertaking being led by ASPRS Past President Charles Toth and, should we win

the bid, it will be the first time the United States has hosted the international Congress since 1992. The decision will be made at the ISPRS Congress in Nice, France this summer.

In closing, I would like to say that it has been a distinct pleasure and honor for me to serve as the President of ASPRS over this past year when I have been able to work with our outstanding Board members and professional staff on a wide range of important issues. I believe that, through our efforts, we have made ASPRS a much stronger Society and that we have laid a firm foundation for continued growth in the coming years. We have demonstrated that we have the flexibility to react to adverse events and the resilience to turn that adversity into strengths. I'm proud of us and what we have accomplished together, and I'm pleased to be able to pass the leadership of our Society over our new President, Jeff Lovin. I know that Jeff will be a strong and capable leader during the coming year of continued growth for the American Society for Photogrammetry and Remote Sensing.



Tommy Jordan, Associate Director, CRMS at University of Georgia, 2019 ASPRS President.

The Executive Director's Report was given during the 2020 ASPRS Annual Conference. The conference was presented online during the week of March 23, 2020.

The ASPRS Headquarters staff:

- Matthew Austin, Graphic Designer, Digital Publications Manager
- Rae Kelley, Assistant Director, Publications
- Karen Schuckman, Managing Director

In our 86th year, ASPRS continues on the upward track of financial stability with a strong and committed group of volunteers – our Board of Directors and Division, Region and Committee leaders - who have truly shown their dedication to the development and promotion of the geospatial sciences. As Tommy Jordan completes his Presidential term, we thank him for his guidance and leadership and welcome Jeff Lovin to the Office and wish him great success during the year.

Even though our Annual Conference has been postponed due to the spread of COVID-19, we were still able to hold all scheduled meetings and even expand our workshop offerings in the virtual meeting world. The architect of our success, both financial and administrative is our indefatigable Managing Director, Karen Schuckman to whom we owe a great deal of thanks.

The shift to presenting our workshops in a virtual format has meant that more people were able to take more of the offerings than ever before. It appears that we had more people at most of the meetings than we would have had in person adding to our rich history of scientific excellence and a consistently high quality of professional services.

Headquarters/Condo

In our Headquarters building, the other three associations are all working from home until further notice. On the ASPRS side, I visit the office once a week and Matthew Austin twice a week mainly to check the mail and deposit checks, etc.

Our renters, BrightView Senior Living, are maintaining a presence but not seeing the public. At this point, they plan to stay on through July, a month longer than originally planned. It's uncertain how all the closings will affect their construction schedule and, as of now, whether they will opt to extend even beyond July. I have talked to one realtor about renting the space to a new client when they move. No action on that at this point.

Certification

The certification application process is now entirely electronic with Brenna LeMaire at P&N handling all the processing of applications, payments, and communications with the respective review committees.

Mike Zoltek, Brenna and I attended the annual (virtual) meeting of the Council of Engineering and Scientific Specialty Boards, the agency that accredits our certification program. Main topic of discussion was their strategic plan with input from all attending.

Awards

Under the direction of Chair Lindi Quackenbush, and the management expertise of Peng Fu, the Awards Committee managed a very successful scholarship application process this year with close to 100 applications.

Annual Election

The recent annual election went very smoothly with P&N handling the electronic balloting (we are no longer using paper ballots). Results were verified by the Teller Committee, Larry Hothem, Chair and Chris McGlone. We still consistently have a low voter turnout.

Membership

Numbers for 2020 so far have been pretty static but it is early and P&N is keeping a close eye on trends and will be reporting on them later in the year. We are developing a membership management plan for the coming year.

Publications

DEM Manual 3rd Edition sales dominate but fluctuate depending on class usage during the academic year.

We continue to sell books on Amazon. We've had 75 orders from September 26, 2019 to March 15, 2020 with the Lidar Manual being the most popular and *DEM 3rd Edition* being the second most popular.

The ASPRS Best Sellers List (totals from Amazon and our on-line book store)

- *DEM 3rd Edition*
- *Airborne Topographic Lidar Manual*
- *Manual of Remote Sensing 4*
- *Manual of Photogrammetry, 6th Edition*
- *Glossary of the Mapping Sciences*

PE&RS

The Allen Press system continues to work well. Backlog of papers has been processed, and the queue is slowly filling up again.

A new way to host the Flipping Book version of *PE&RS* will be decided upon before October 2020, when Chrome stops supporting Flash. An HTML web page for each issue hosted on the ASPRS website would most likely be the best solution. Hosting a downloadable PDF of each issue's public version (minus peer-reviewed papers) is the direction we're going.

In these difficult times, the cooperation and help we have received from our members, volunteers and staff has been exceptional and a tribute to everyone's commitment to keeping our Society alive and well until we emerge from this terrible pandemic. My sincere thanks go out to all.



Jesse Winch, Acting Executive Director

ASPRS BOARD OF DIRECTORS

BOARD OFFICERS

President

Jeff Lovin

Woolpert

President-Elect

Jason M. Stoker, Ph.D.

U.S. Geological Survey

Vice President

Christopher Parrish, Ph.D.

Oregon State University

Past President

Thomas Jordan, Ph.D.

University of Georgia

Treasurer

Stewart Walker, Ph.D.

Secretary

Lorraine B. Amenda, PLS, CP

BOARD MEMBERS

Sustaining Members Council – 2021

Chair: Joe Cantz

Early-Career Professionals Council – 2021

Chair: Bobby Arlen

Vice Chair: Melissa Martin

Region Officers Council – 2021

Chair: Lorraine B. Amenda, PLS, CP

Vice Chair: Demetrio Zourarakas

Student Advisory Council – 2021

Chair: Youssef Kaddoura

Technical Division Directors Council – 2021

Chair: Bandana Kar, Ph.D.

Vice Chair: Denise G. Theunissen

TECHNICAL DIVISION OFFICERS

Geographic Information Systems Division – 2021

Director: Xan Fredericks

Assistant Director: Denise G. Theunissen

Lidar Division – 2022

Director: Joshua Nimetz, CMS

Assistant Director: Ajit Sampath

Photogrammetric Applications Division – 2022

Director: Kurt Rogers

Assistant Director: Benjamin Wilkinson

Primary Data Acquisition Division – 2021

Director: Jon Christopherson

Assistant Director: J. Chris Ogier

Professional Practice Division – 2022

Director: Harold W. Rempel, III, CP

Assistant Director: Bill Swope

Remote Sensing Applications Division – 2022

Director: Raechel A. Portelli, Ph.D.

Assistant Director: Amr Abd-Elrahman

Unmanned Autonomous Systems (UAS) – 2022

Director: Megan Ritelli, Ph.D.

Assistant Director: Dan Hubert

REGION PRESIDENTS

Alaska Region

David Parret

Cascadia Region

Robert Hairston-Porter

Eastern Great Lakes Region

Shawana P. Johnson, Ph.D, GISP

Florida Region

Xan Fredericks

Heartland Region

Whit Lynn

Northeast Region

(representing the merger of The New England and Central New York Regions)

Travis Gigliotti, Interim President

North Atlantic Region

Richard W. Carlson, Jr., P.L.S., C.P.

Pacific Southwest Region

Omar G. Mora

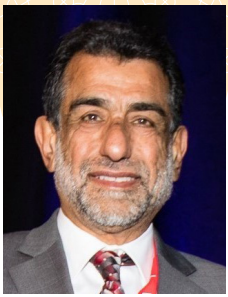
Potomac Region

Dave Lasko

Rocky Mountain Region

Western Great Lakes Region

Brandon Krumwiede



MAPPING MATTERS

YOUR QUESTIONS ANSWERED

The layman's perspective on technical theory and practical applications of mapping and GIS

BY Qassim A. Abdullah, Ph.D., PLS, CP**

QUESTION:

Question: For one of our projects, we have been asked to provide an orthorectified imagery product with a horizontal accuracy of 10cm at 95% confidence, according to the ASPRS Positional Accuracy Standards for Digital Geospatial Data of 2014. The questions I have are the following:

1. What is the ground sampling distance (GSD) of the imagery we need to collect and use to meet the required accuracy?
2. What is the accuracy of the ground control points we need for the aerial triangulation?
3. What is the accuracy of aerial triangulation we need to meet?
4. Can we use RTK surveying techniques to survey the needed ground control points?

Dr. Srinu Dharmapuri CP, PMP, GISP, Sanborn

Dr. Abdullah: First, I would like to reiterate the design philosophy that the new ASPRS Positional Accuracy Standards for Digital Geospatial Data of 2014 was based upon, and that is that the standards are sensor agnostic and data driven. With this philosophy, the standards do not endorse the use of GSD, contour interval or map scale to express product accuracy. Product accuracy should be determined by user need and the fidelity and quality of the product generation process. Certain imagery resolution can be used to produce orthorectified products with different accuracies based on the production process used, quality and number of ground control points, and the quality and accuracy of the digital elevation model used in the orthorectification process. Another good reason for not associating product accuracy with imagery resolution is the various designs of today's digital cameras. Film-based aerial cameras were designed with one film format/size (9 inches or 229mm) and one lens focal length (6 inches or 152mm), which enabled us to predict product accuracy based on film scale or flying altitude. Digital aerial cameras are made with a variety of charge-coupled device (CCD) array size and lenses that make it impossible to adopt one accuracy figure for all of them based on the flying altitude or imagery ground resolution. Table 1 illustrates this issue as it lists the flying altitudes for six well-known digital cameras, all set to acquire imagery with 15cm resolution. The table shows the wide range of altitudes (1,440m to 3,538m above ground

Table 1. Digital cameras and flying altitude.

Sensor	Flying Altitude (m)	Flying Altitude (ft)
UltraCAM CONDOR (100mm)	3,261	10,698
ULTRACAM EAGLE MARK III (92mm)	3,450	11,319
DMC III (92mm)	3,538	11,609
ADS100 (62.5mm)	1,875	6,152
PhaseONE 190MP	2,935	9,629
ADS80	1,440	4,725

level, or AGL) used for different cameras to acquire the same 15cm imagery.

While products from these cameras are expected to meet the highest accuracy when a stringent photogrammetric workflow is followed, one needs to be extra careful when dealing with imagery acquired from a very high altitude. Errors in the final products caused by the residual errors in the computed exterior-orientation parameters, especially the sensor attitudes (i.e. omega, phi and kappa), are linearly proportional to the flying altitude. Table 2 lists the degree of error expected in a product

Table 2. Relationship between flying altitude and product horizontal accuracy.

Flying Altitude AGL (ft)		Horizontal Error in X or Y (ft)	
ft	meter	ft	cm
100.0	30.5	0.007	0.22
150.0	45.7	0.011	0.33
200.0	61.0	0.015	0.44
400.0	121.9	0.029	0.89
3,000.0	914.4	0.218	6.65
6,000.0	1,828.8	0.436	13.30
10,000.0	3,048.0	0.727	22.17

Photogrammetric Engineering & Remote Sensing
Vol. 86, No. 6, June 2020, pp. 347–349.
0099-1112/20/347–349

© 2020 American Society for Photogrammetry
and Remote Sensing
doi: 10.14358/PERS.86.6.347

“The new Accuracy Standards for Digital Geospatial Data of 2014 are sensor agnostic and data driven. It does not endorse the use of GSD, contour interval or map scale to express product accuracy.”

using inaccurate sensor altitudes, as determined by an aerial triangulation that is accurate to 15 arc seconds.

Table 2 clearly demonstrates why products from unmanned aircraft systems (UAS) flown from an altitude of 45 meters are expected to be more accurate than products flown from an altitude of 3,048 meters using manned aircraft.

Now that I have explained the problem with associating product accuracy with imagery resolution, let me respond to your questions:

1) What is the imagery GSD you need to request to meet the 10cm accuracy threshold?

Before I answer this question, let us convert your accuracy figure from 95% confidence level to root mean square error (RMSE) so it is compatible with ASPRS accuracy standards. The ASPRS standard in Section B.7 provides the following conversion formula:

$$\text{Accuracy at 95\% or Accuracy}_T = 2.4477 \times \text{RMSE}_x = 2.4477 \times \text{RMSE}_y$$

Therefore,

$$\text{RMSE}_x \text{ or } \text{RMSE}_y = \text{Accuracy at 95\%} / 2.4477, \text{ or}$$

$$\text{RMSE}_x \text{ or } \text{RMSE}_y = 10\text{cm} / 2.4477 = 4.085\text{cm}$$

Again, ASPRS does not provide exact correlation between product accuracy and imagery resolution for the reasons I outlined earlier. However, the ASPRS standards provided guidelines for the users to be followed during the transition period from the legacy ASPRS standards of 1990 to the new standards. Table B.5 of the standards, also partially provided in Table 3, provides recommendations on the orthoimagery pixel sizes and the associated accuracy classes. These are largely based on experience with current sensor technologies and primarily apply to large- and medium-format metric cameras. The table is only provided as a guideline for users during the transition period to the new standards. These associations may change in the future as mapping technologies continue to advance and evolve. As you see in Table 3 and based on our experience with digital cameras, users on a regular basis obtained accuracy that is equivalent to two times the GSD and, in some cases, one GSD if extra efforts were exerted during the production process. Based on this, you can propose the acquisition of imagery with a GSD of 8cm or even 4cm if needed. I do not recommend the latter GSD of 4cm as it is a risky practice that may jeopardize your ability to deliver products with an accuracy of 4cm.

“RTK surveying techniques will not meet these requirements and you will need to use traditional surveying techniques or static GPS for horizontal coordinates and differential leveling for height survey or the combination of the two”

Table 3 digital orthoimagery accuracy examples for current large and medium format metric cameras.

Common Orthoimagery Pixel Sizes	Recommended Horizontal Accuracy Class RMSE _x and RMSE _y (cm)	Orthoimage RMSE _x and RMSE _y in terms of pixels	Recommended use
1.25cm	≤1.3	≤1 pixel	Highest accuracy work
	2.5	2 pixels	Standard mapping and GIS work
	≥3.8	≥3 pixels	Visualization and less accurate work
2.5cm	≤2.5	≤1 pixel	Highest accuracy work
	5.0	2 pixels	Standard mapping and GIS work
	≥7.5	≥3 pixels	Visualization and less accurate work
5cm	≤5.0	≤1 pixel	Highest accuracy work
	10.0	2 pixels	Standard mapping and GIS work
	≥15.0	≥3 pixels	Visualization and less accurate work
7.5cm	≤7.5	≤1 pixel	Highest accuracy work
	15.0	2 pixels	Standard mapping and GIS work
	≥22.5	≥3 pixels	Visualization and less accurate work
15cm	≤15.0	≤1 pixel	Highest accuracy work
	30.0	2 pixels	Standard mapping and GIS work
	≥45.0	≥3 pixels	Visualization and less accurate work

2) **What is the accuracy of the ground control points you need for the aerial triangulation?**

ASPRS standards require the accuracy for the ground control points to meet the following criteria:

- a. The accuracy of ground control designed for planimetric data (orthoimagery and/or digital planimetric map) production **only**:

$$\text{RMSE}_x \text{ or } \text{RMSE}_y = 1/4 * \text{RMSE}_{x(\text{Map})} \text{ or } \text{RMSE}_{y(\text{Map})},$$

$$\text{RMSE}_z = 1/2 * \text{RMSE}_{x(\text{Map})} \text{ or } \text{RMSE}_{y(\text{Map})}$$

- b. The accuracy of ground control designed for elevation data, or planimetric data and elevation data production:

$$\text{RMSE}_x, \text{RMSE}_y \text{ or } \text{RMSE}_z = 1/4 * \text{RMSE}_{x(\text{Map})}, \text{RMSE}_{y(\text{Map})} \text{ or } \text{RMSE}_{z(\text{DEM})}$$

According to the above requirements, here are the accuracy figures for the ground control points for your project:

- a. To produce orthos and planimetric map **ONLY**:
Accuracy of ground control RMSE_x or $\text{RMSE}_y = 1\text{cm}$
Accuracy of ground control $\text{RMSE}_z = 2\text{cm}$
- b. To produce orthos, planimetric maps and digital elevation models:
Accuracy of ground control $\text{RMSE}_x, \text{RMSE}_y$ or $\text{RMSE}_z = 1\text{cm}$, assuming that the accuracy of the derived elevation data is also expected to meet an RMSE_z of 4cm .

Film-based aerial cameras were designed with one film format/size (9 inches or 229mm) and one lens focal length (6 inches or 152mm), which enabled us to predict product accuracy based on film scale or flying altitude."

3) **What is the accuracy of aerial triangulation you need to meet?**

ASPRS standards require the following accuracy for aerial triangulation:

- a. The accuracy of aerial triangulation designed for planimetric data (orthoimagery and/or digital planimetric map) production **only**:

$$\text{RMSE}_{x(AT)} \text{ or } \text{RMSE}_{y(AT)} = 1/2 * \text{RMSE}_{x(\text{Map})} \text{ or } \text{RMSE}_{y(\text{Map})},$$

$$\text{RMSE}_{z(AT)} = \text{RMSE}_{x(\text{Map})} \text{ or } \text{RMSE}_{y(\text{Map})}$$

- b. The accuracy of ground control designed for elevation data, or planimetric data and elevation data production:

"Digital aerial cameras are made with a variety of CCD array size and lenses that make it impossible to adopt one accuracy figure for all of them based on the flying altitude or imagery ground resolution"

$$\text{RMSE}_{x(AT)}, \text{RMSE}_{y(AT)} \text{ or } \text{RMSE}_{z(AT)} = 1/2 * \text{RMSE}_{x(\text{Map})}, \text{RMSE}_{y(\text{Map})} \text{ or } \text{RMSE}_{z(\text{DEM})}$$

According to the above requirements, here are the accuracy figures for aerial triangulation for your project:

- a. To produce orthos and planimetric maps **ONLY**:

$$\text{RMSE}_{x(AT)} \text{ or } \text{RMSE}_{y(AT)} = 2\text{cm}$$

$$\text{RMSE}_{z(AT)} = 4\text{cm}$$

- b. To produce orthos, planimetric maps and digital elevation models:

$\text{RMSE}_x, \text{RMSE}_y$ or $\text{RMSE}_z = 2\text{cm}$, assuming that the accuracy of the derived elevation data is also expected to meet an RMSE_z of 4cm .

4) **Can we use RTK surveying techniques to survey the needed ground control points?**

RTK field surveying techniques usually result in an accuracy of about 2cm horizontally and 3cm vertically (as RMSE or one sigma). Considering the 1cm accuracy requirement for the ground control points needed for your product, RTK surveying techniques will not meet these requirements and you will need to use traditional surveying techniques or static GPS for horizontal coordinates and differential leveling for height survey or the combination of the two.

***Dr. Abdullah is Vice President and Chief Scientist at Woolpert, Inc. He is also adjunct professor at Penn State and the University of Maryland Baltimore County. Dr. Abdullah is ASPRS fellow and the recipient of the ASPRS Life Time Achievement Award and the Fairchild Photogrammetric Award.*

The contents of this column reflect the views of the author, who is responsible for the facts and accuracy of the data presented herein. The contents do not necessarily reflect the official views or policies of the American Society for Photogrammetry and Remote Sensing, Woolpert, Inc., Penn State, and/or the University of Maryland Baltimore County.

Having Options is a Good Thing

Introduction

Let's face it, we have options when it comes to completing our geospatial tasks. That's a good thing. I cannot tell you the countless times I've had a chat with a colleague to determine how we can speed up a process and learn they are using slightly different tools or methods to meet the same goal as I am. That's the beauty of our industry, you don't have to know everything to achieve quality results, but the more experience we obtain we find new and exciting ways to achieve them faster. In this case, having options is a good thing.

MicroStation

MicroStation by Bentley Systems is a robust piece of CAD software that is versatile in its usefulness across multiple industries but can be a notoriously finicky program. The



GUI isn't the most intuitive design, with its weird menus that require a click and hold of the mouse, windows that disappear, and funky terminology (what's the difference between a fence and a SmartLine again?). Yet, despite its quirks, MicroStation provides enough functionality to accomplish many robust tasks. Essentially, the challenge of learning the program pays off when you can accomplish functions such as seeing edits to a digital elevation model occur in real time.

Topic: Selection Tools

If you are working with shapes, text, or any other element within MicroStation you almost certainly have used the Element Selection tool. The tool is used to target an element for modification or manipulation. The most common way to select is using the *Individual* method, where the user can click on an element to select it or draw a rectangle, where the direction you draw determines the selection. To select multiple elements the user can hold the <Ctrl> key. Likewise, to deselect an element the same key is used. One of MicroStation's quirks shows itself when using the *Individual* method to select an element by rectangle. By dragging left to right, anything contained in the box is selected. Dragging the cursor right to left selects anything that the selection box crosses.



Element
Selection



Drag selection box left to right.



Drag selection box right to left.

Yes, something as simple as the direction of the selection box changes its function but it doesn't end there. By holding the <Shift> key the user can alternate between both while drawing left to right. It seems easy enough, drawing left or drawing right to select in the box or anything the box touches but it can be frustrating when confusion sets in. Don't ask me why but drawing in the same direction and using <Shift> to determine the selection method works for me. Maybe the drawing direction of the box works for you. Whichever method works for you, it's nice that Bentley gave us some options to work with.

Al Karlin, Ph.D., CMS-L, GISP and Todd Waldorf are with Dewberry's Geospatial and Technology Services group in Tampa, FL. As a Senior GIS Professional, Al works with all aspects of Lidar, remote sensing, photogrammetry, and GIS-related projects. Todd is a Geospatial Analyst who works on Lidar and Remote Sensing projects and in his spare time does some photo-interpretation and creative writing.

Photogrammetric Engineering & Remote Sensing
Vol. 86, No. 6, June 2020, pp. 350.

0099-1112/20/350

© 2020 American Society for Photogrammetry
and Remote Sensing

doi: 10.14358/PERS.86.6.350



& GRIDS & DATUMS

BY Clifford J. Mugnier, CP, CMS, FASPRS

THE SOCIALIST REPUBLIC OF VIETNAM

The Grids & Datums column has completed an exploration of every country on the Earth. For those who did not get to enjoy this world tour the first time, *PE&RS* is reprinting prior articles from the column. This month's article on the Socialist Republic of Vietnam was originally printed in 2002 but contains updates to their coordinate system since then.

Inhabited since Paleolithic times, the beginning of Vietnamese civilization dates back to the late Neolithic or early Bronze Age. Vietnam is tropical in the south and subject to monsoons in the north. The country is low, comprised of the Mekong Delta in the south, the Red River Delta in the north, central highlands, hilly, mountainous in the far north and northwest. The lowest point in Vietnam is the South China Sea; the highest is Ngoc Linh at 3,143 meters. The area of Vietnam is slightly larger than New Mexico; with a 3,260-km coastline, its maritime boundary had been established according to the "Straight Baseline" principle. Vietnam is a poor, densely populated communist state that has had to recover from the ravages of war, the loss of financial support from the old Soviet Bloc, and the rigidities of a centrally planned economy. Independence Day is 02 September (1945).

France had occupied all of Vietnam by 1884 and remained for the most part until 1954. Longitude was determined in Haiphong by Héraud and Bouillet, hydrographic engineers, in 1874. The longitude was deduced from the time transfer from Saigon; two chronometers were used for the first traverse and five chronometers were used between the observatory at Haiphong and the observatory of Saigon. It is interesting to note that by 1883, Hong Kong and Haiphong were connected by submarine cable. The longitude of Hong Kong had been determined in 1881 by telegraph, so it was deduced that the longitude of Haiphong was now determined to a better precision than was determined by the use of chronometers. In 1886, Héraud measured the baseline in Haiphong between Grand Mirador and Petit Mirador to be 4,312.8 meters. "The observatory in Haiphong was established to observe the longitude difference. It was essentially comprised of a masonry pillar constructed on a solid foundation, and a grass hut was constructed of bamboo." The position observed



in 1874 was $\Phi_0 = 20^\circ 51' 43.5''$ N and $\Lambda_0 = 104^\circ 20' 30''$ East of Paris or $106^\circ 40' 43.95''$ East of Greenwich. These observations were the initial determinations that later would provide the defining datum for the northern part of Vietnam. Grand Mirador was defined as the position of the geodetic net (Position du réseau géodesique indochinois) where $\Phi_0 = 21^\circ 01' 58.415''$ N and $\Lambda_0 = 109^\circ 00' 57.90''$ East of Greenwich. The azimuth from Grand Mirador to Nui Deo is $\alpha_0 = 334^\circ 29' 49.8''$. The ellipsoid of reference is the Clarke 1880 where $a = 6,378,249$ m and $1/f = 293.46$. The subsequent transferred origin of the grid for Signal Grand Mirador was $\phi_0 = 20^\circ 42' 24.337''$ N and $\lambda_0 = 106^\circ 46' 29.282''$ East of Greenwich. The False Easting and False Northing for this Hatt Azimuthal Projection were each equal to zero. There were

Photogrammetric Engineering & Remote Sensing
Vol. 86, No. 6, June 2020, pp. 351–353.
0099-1112/20/351–353

© 2020 American Society for Photogrammetry
and Remote Sensing
doi: 10.14358/PERS.86.6.351

four bases measured in the 1880s by the French; they were near Sontay, at Than-Hoa, south of Haiphong, and near Baria.

Grand Mirador de Do-Son was observed in April, 1887, and was a local datum such that $\Phi_0 = 20^\circ 42' 24.9''$ N and $\Lambda_0 = 106^\circ 46' 36.15''$ East of Greenwich. The defining azimuth was $\alpha_0 = 191^\circ 33' 22''$. In 1929, the coordinates were updated to $\Phi_0 = 20^\circ 42' 24.34''$ N and $\Lambda_0 = 106^\circ 46' 29.28''$ E, and in 1932 A. Gougenheim finally changed the coordinates of Doson to $\Phi_0 = 20^\circ 42' 24.337''$ N and $\Lambda_0 = 106^\circ 46' 29.2282''$ E.

Another grid was defined as Haiphong, the west gable of the observatory pagoda: $\Phi_0 = 20^\circ 51' 44.3''$ N and $\Lambda_0 = 106^\circ 40' 43.95''$ E. Nearby, the derivative Hanoi system at the "tour de la citadelle," the tower of the standard, had coordinates of $\phi_0 = 21^\circ 01' 58''$ N and $\lambda_0 = 103^\circ 29' 52.2''$ E, and was used for some French surveys, but it was based on the Haiphong System because its coordinates are $x = 99,618.0$ m W. and $y = 34,531.0$ m N. Furthermore, the derivative Tour de la citadelle de Nam Dinh had coordinates of $\phi_0 = 20^\circ 25' 30.4''$ N and $\lambda_0 = 103^\circ 49' 50.0''$ E, and was used for some French surveys, but was based on the Haiphong System because its coordinates are $x = 65,292.8$ m W. and $y = 32,917.5$ m S. Note that all the azimuthal grids used by the French in Vietnam were quadrant-based; no false origins were used.

The Hon-Matt Grid based on the Hatt Azimuthal projection was established in 1877, and is near Vinh on the Ca River. The coordinates of the origin are $\phi_0 = 18^\circ 47' 40''$ N and $\lambda_0 = 105^\circ 55' 58.95''$ E. In 1924, the Hon-Nieu Grid was used where $\phi_0 = 18^\circ 48' 10.183''$ N and $\lambda_0 = 105^\circ 46' 33.799''$ E. It was also used in 1932 for additional French hydrographic surveys. The old Cape Saint-Jacques Light-house (phare) hydrographic survey was based on $\phi_0 = 10^\circ 19' 33.220''$ N and $\lambda_0 = 104^\circ 44' 32.663''$ E.

The Bay of Tourane (now Da Nang) Grid was established in 1907 by Cot, where $\phi_0 = 16^\circ 11' 01.44''$ N and $\lambda_0 = 108^\circ 06' 17.61''$ E; the pillar was listed at Nui-Hoi. The defining azimuth from Nui-Hoi to Tien-Cha is $\alpha_0 = 110^\circ 33' 32.2''$.

In 1913, a number of new hydrographic survey grids were established, including the Cathedral of Saigon, where: $\phi_0 = 10^\circ 46' 44.180''$ N and $\lambda_0 = 104^\circ 21' 25.803''$ East of Paris, as compared with the Old Observatory of Saigon where $\phi_0 = 10^\circ 46' 42.78''$ N and $\lambda_0 = 104^\circ 21' 31.29''$ East of Paris. (Note that Paris is $2^\circ 20' 13.95''$ East of Greenwich.) The Bay of Natrang was surveyed with a Hatt Grid in 1913, and the origin of the coordinates was at Signal Honheo where $\phi_0 = 12^\circ 24' 13.11''$ N and $\lambda_0 = 106^\circ 56' 00.14''$ East of Paris.

By 1914, a Hatt Azimuthal Grid was observed and

STAND OUT FROM THE REST

EARN ASPRS CERTIFICATION

ASPRS congratulates these recently Certified and Re-certified individuals:

CERTIFIED MAPPING SCIENTIST UAS

Hayes Wilkinson, Certification #UAS033

Effective May 5, 2020, expires May 5, 2025

RECERTIFIED MAPPING SCIENTISTS GIS/LIS

Timothy Thomas, Certification #R174GS

Effective February 2, 2020, expires February 2, 2025

John Bender, Certification #R211GS

Effective April 1, 2020, expires April 1, 2025

RECERTIFIED MAPPING SCIENTIST REMOTE SENSING

Jonathan Ellinger, Certification #R224RS

Effective December 15, 2019, expires December 15, 2024

RECERTIFIED PHOTOGRAMMETRISTS

Michael B. Shillenn, Certification #R1027

Effective March 18, 2020, expires March 18, 2025

Sean Maxwell, Certification #R1066

Effective January 11, 2020, expires January 11, 2025

James "Chip" Campbell, Certification #R1443

Effective March 14, 2020, expires March 14, 2025

Zachary DiCicco, Certification #R1581

Effective March 19, 2020, expires March 19, 2025

Todd Andrews, Certification #R1471

Effective December 15, 2019, expires December 15, 2024

Brad W. Marz, Certification #R1448

Effective June 28, 2020, expires June 28, 2025

ASPRS Certification validates your professional practice and experience. It differentiates you from others in the profession. For more information on the ASPRS Certification program: contact certification@asprs.org, visit <https://www.asprs.org/general/asprs-certification-program.html>



established at Cana, where $\phi_0 = 11^\circ 22' 35.067''$ N and $\lambda_0 = 108^\circ 50' 20.137''$ E (1929 updated coordinates are listed). After the First World War in Europe, the Cana Grid was also used for the Îles Catwick in 1924. In 1923, a local survey was run from the lighthouse at Baikan where $\phi_0 = 8^\circ 39' 59.17''$ N and $\lambda_0 = 104^\circ 21' 48.31''$ East of Paris; X_0 and Y_0 were equal to zero. A datum and cadastral grid system were established at Long Vinh where $\Phi_0 = 9^\circ 35' 59.79''$ N and $\Lambda_0 = 106^\circ 18' 58.07''$ East of Greenwich. The baseline was run from Lich Hoi Binch to Long Vinh, and measured 17,805.73 m. The defining azimuth of that baseline was $\alpha_0 = 230^\circ 56' 07.426''$. That same year, the Îles Poulo-Condore Datum of 1923 (now Con Son) was established where $\Phi_0 = 8^\circ 41' 35.86''$ N, $\Lambda_0 = 104^\circ 14' 27.28''$ East of Paris, the azimuth of West Base to East Base was defined as $\alpha_0 = 191^\circ 33' 22''$, and its length was measured to be 1,411.83 m. By 1923, the coordinates for “Mirador d’ Hanoi” were published as $\phi_0 = 21^\circ 01' 58.415''$ N and $\lambda_0 = 103^\circ 29' 52.120''$ East of Paris.

In the annual report of A. Gougenheim for his hydrographic mission to French Indochina of June 1930 to June 1931, he listed a projection summary that enumerated all of the Hatt Azimuthal Equidistant projections he used that year in his mission, including the calculating machine coefficients for both the direct and the inverse for Origine Grand Mirador de Doson, Origine Hon Nieu, Origine Cana, and Origine Nui Chauvien. Each pair of formulae for direct and inverse also included a version for units of sexagesimal seconds (degrees) as well as centesimal seconds (grads). Of course, everything was truncated at the cubic! Gougenheim later presented his own machine calculation for the ellipsoidal geodesic that was recast and presented by Paul D. Thomas of the U.S. Naval Hydrographic Office during the 1970s.

After the Second World War, three Hatt Azimuthal Grids were devised by the French in Vietnam. The Signal Haiphuc (1933) origin was at $\phi_0 = 13^\circ 26' 04.693''$ N and $\lambda_0 = 109^\circ 17' 44.322''$ East of Greenwich. The Borne (monument) de Bac Lieu (1933) origin was at $\phi_0 = 9^\circ 15' 42.02''$ N and $\lambda_0 = 105^\circ 43' 14.48''$ East of Greenwich. The last grid established by the French was at Cam Ranh Bay in 1949 where the origin was published as $\phi_0 = 11^\circ 55' 55.85''$ N and $\lambda_0 = 100^\circ 49' 58.60''$ East of Paris rather than East of Greenwich!

John W. Hager tells me that “in 1954, the triangulation of Thailand was adjusted to Indian 1916 [Datum] based on 10 stations on the Burma border. In 1960, the triangulation of Cambodia and Vietnam was adjusted holding fixed two Cambodian stations connected to the Thailand adjustment of stations from the Cambodian-Vietnam adjustment. North Vietnam was also adjusted to this system but with lower standards. The details are that of the Indian Datum as defined in 1900 and labeled as Indian 1916: origin at Kalianpur Hill Station, $\Phi_0 = 24^\circ 07' 11.26''$ N, $\Lambda_0 = 77^\circ 39' 17.57''$ East of Greenwich, the initial azimuth to Surantal from south is: $\alpha_0 = 190^\circ 27' 05.10''$. The ellipsoid of reference is the Everest 1830 where $a = 6,377,276.345$ m, and $1/f = 300.8017''$.”

I was assigned to Army Map Service (later TOPOCOM)

during the Vietnam War, and for a short period was a Company Commander. Some of “my” personnel were at a SECOR satellite tracking station in Thailand while establishing a precise location for a SHORAN transmitter for navigation control of airplanes. The South Asia Datum was used for that application, and was referenced to the Modified Fisher 1960 ellipsoid where $a = 6,378,155$ m and $1/f = 298.3$. I do not think that that Datum was ever used (at that time) for unclassified applications. NIMA lists two transformations for Vietnam. For Vietnam near 16° N, from the Indian 1960 Datum to the WGS 84 Datum: $\Delta X = +198\text{m} \pm 25\text{m}$, $\Delta Y = +881\text{m} \pm 25\text{m}$, and $\Delta Z = +317\text{m} \pm 25\text{m}$, and the solution is based on two stations. For Con Son Island from the Indian 1960 Datum to the WGS 84 Datum: $\Delta X = +182\text{m} \pm 25\text{m}$, $Y = +915\text{m} \pm 25\text{m}$, and $\Delta Z = +344\text{m} \pm 25\text{m}$, and the solution is based on one station.

Mal Jones of Perth, Australia tells me that from the WGS 84 Datum to the Hanoi 1972 Datum, the ellipsoid of reference is the Krassovsky 1940 where $a = 6,378,245$ m and $1/f = 298.3$, and the parameters are $\Delta X = -21\text{m}$, $\Delta Y = +124\text{m}$, $\Delta Z = +68\text{m}$, rX axis rotation = $+0''$, rY axis rotation = $+0''$, rZ axis rotation = $+0.814''$, and dS scale change = $+0.38$ ppm. From the WGS 84 Datum to the Indian (Vietnam) Datum, $X = -199\text{m}$, $\Delta Y = -931\text{m}$, and $\Delta Z = -321\text{m}$. According to “Vietsovpetro,” further details and accuracy are unknown. However, this is suspiciously close to the VT78 parameters for the WGS 72 Datum that I received from Robert Holloway of Mt. Lawley, West Australia back in 1998. The current geodetic and mapping authority is the General Department of Land Administration in Hanoi. Vietnam continues to be an enigma, and I believe that it is due to its history of the last couple of centuries..

UPDATE

Vietnam geodesy is no longer an enigma. Hoa, Dung, Thu, Huynh and Nhung published a paper¹ last year that detailed in exquisite detail the relationships among VN-2000, ITRS, WGS84 & PZ-90 and the various realizations of those systems.

The National Coordinate Control Network consists of 71 points of “0” order, 328 points of 1st order, 1,177 points of 2nd order, 160 points of 2nd order traverse, and 12,658 points of 3rd order. Vietnam has implemented a national network of GPS CORS sites and appears to be completely open for business development.

¹ <https://doi.org/10.1051/e3sconf/20199403014>

The contents of this column reflect the views of the author, who is responsible for the facts and accuracy of the data presented herein. The contents do not necessarily reflect the official views or policies of the American Society for Photogrammetry and Remote Sensing and/or the Louisiana State University Center for GeoInformatics (C⁴G). This column was previously published in *PE&RS*.

David C. Smith

November 30, 1938 to March 24, 2020

On March 24, 2020, David C. Smith (81) passed away peacefully at his home in Portland, Oregon, surrounded by his family.

Dave was a Certified Photogrammetrist and Professional Land Surveyor and the founder of David C. Smith and Associates, Inc., a photogrammetric mapping company located in Portland, Oregon. Dave was a long-time member of ASPRS, one of the original members of MAPPS when it was formed in 1982 and served one term as MAPPS president. Dave remained active in both organizations for many years; he was also an active member of ACSM, Professional Land Surveyors of Oregon and the Professional Land Surveyors of Washington.



Dave was a pioneer in the photogrammetry industry and embraced new technologies. He was an early adopter of orthophotography, digital mapping, analytical aero-triangulation and other emerging photogrammetry technologies in the 1970's and 1980's. He was very successful in business, choosing to keep the company as a small family business in order to balance his passion for his business with his love of family, church and the outdoors. He spent his free time hunting, fishing, biking, skiing, golfing, vacationing with his children and grandchildren and traveling with his wife Marilyn. Currently, David C. Smith and Associates, Inc. is run by Dave's two sons, Scott and Doug Smith.

Dave became interested in surveying and photogrammetry at Oregon State College (now Oregon State University) during course work taken in working towards his Bachelor of Science degree in Forestry, which he earned in 1960. While in college Dave worked summers fighting forest fires for the State of Oregon and was enrolled in the Army ROTC program. Upon earning his degree, Dave was commissioned as a Second Lieutenant in the Army. In 1962, following his service in the army, Dave worked briefly as a timber cruiser for Weyerhaeuser before moving to Portland to pursue a career in photogrammetry and surveying. He initially worked for KB Wood & Associates, Inc. before purchasing the mapping business from Mr. Wood and forming his own photogrammetry company, David C. Smith and Associates, in 1965.

Dave is survived by his wife, Marilyn Smith, his three children and his four grandchildren.

JOURNAL STAFF

Editor-In-Chief

Alper Yilmaz, Ph.D., PERSeditor@asprs.org

Associate Editors

Rongjun Qin, Ph.D., qin.324@osu.edu

Michael Yang, Ph.D., michael.yang@utwente.nl

Petra Helmholz, Ph.D., Petra.Helmholz@curtin.edu.au

Bo Wu, Ph.D., bo.wu@polyu.edu.hk

Clement Mallet, Ph.D., clemallet@gmail.com

Vasit Sagan, Ph.D., Vasit.Sagan@slu.edu

Jose M. Pena, Ph.D., jmpena@ica.csic.es

Prasad Thenkabail, Ph.D., pthenkabail@usgs.gov

Ruisheng Wang, Ph.D., ruiswang@ucalgary.ca

Desheng Liu, Ph.D., liu.738@osu.edu

Valérie Gouet-Brunet, Ph.D., valerie.gouet@ign.fr

Dorota Iwaszczuk, Ph.D., dorota.iwaszczuk@tum.de

Qunming Wang, Ph.D., wqm11111@126.com

Filiz Sunar, Ph.D., fsunar@itu.edu.tr

Norbert Pfeifer, Ph.D., np@ipf.tuwien.ac.at

Jan Dirk Wegner, Ph.D., jan.wegner@geod.baug.ethz.ch

Hongyan Zhang, Ph.D., zhanghongyan@whu.edu.cn

Zhenfeng Shao, Ph.D., shaozhenfeng@whu.edu.cn

Dongdong Wang, Ph.D., ddwang@umd.edu

Assistant Editor

Jie Shan, Ph.D., jshan@ecn.purdue.edu

Contributing Editors

Grids & Datums Column

Clifford J. Mugnier, C.P., C.M.S., cjmce@lsu.edu

Book Reviews

Sagar Deshpande, Ph.D., bookreview@asprs.org

Mapping Matters Column

Qassim Abdullah, Ph.D., Mapping_Matters@asprs.org

Sector Insight

Lucia Lovison-Golob, Ph.D., lucia.lovison@sat-drones.com

Bob Ryerson, Ph.D., FASPRS, bryerson@kimgeomatics.com

GIS Tips & Tricks

Alvan Karlin, Ph.D., CMS-L, GISP akarlin@Dewberry.com

ASPRS Staff

Assistant Director — Publications

Rae Kelley, rkelley@asprs.org

Electronic Publications Manager/Graphic Artist

Matthew Austin, maustin@asprs.org

Advertising Sales Representative

Bill Spilman, bill@innovativemediasolutions.com

ASPRS GEO WEEK 2020 TECHNICAL PROGRAM IS GOING VIRTUAL IN JUNE!

Due to continuing uncertainties and safety concerns related to the COVID-19 pandemic, ASPRS has made the difficult decision to withdraw from the Geo Week 2020 face-to-face event currently scheduled at the McCormick Center in Chicago, Illinois on July 27-29. We are offering all presenters originally accepted for the March event in Washington, DC the opportunity to share their work in the ASPRS 2020 Annual Conference Virtual Technical Program, a series of online technical sessions during the week of June 22 – 26, 2020.

Because the ASPRS 2020 Annual Conference Virtual Technical Program is being hosted, organized, and managed by ASPRS alone, there will be a new, separate registration process and fee for all presenters and attendees. Existing Geo Week 2020 conference registrations are NOT TRANSFERABLE to this new ASPRS event. You may contact info@geo-week.com if you wish to request a refund for all or part of your Geo Week 2020 registration or transfer your 2020 registration to Geo Week 2021.

The ASPRS 2020 Annual Conference Virtual Technical Program is open for both presenters and attendees at <http://conferences.asprs.org/geoweeek-2020>. Registrants will be given access to all of the online technical sessions as live webinars and as on-demand recordings. The full program will be published on the conference website on June 8, 2020.

Registration fees for presenters and attendees are shown below. ASPRS members are eligible for a discount. Non-members who join ASPRS during the conference registration process will also be eligible for the member discount.

Non-Member	\$200
ASPRS Individual Member	\$150
ASPRS Student Member	\$ 50
Non-Member Individual + 1-year ASPRS membership	\$300
Non-Member Student + 1-year ASPRS membership	\$100

Important dates and deadlines are as follows:

- May 13, 2020 — Online Registration open
- May 25, 2020 — Presenter Registration deadline
- June 8, 2020 — Virtual Technical Program published

NEW ASPRS MEMBERS

ASPRS would like to welcome the following new members!

At Large

Gerard Allali
 Fei Deng
 Hongjie He
 Bing Xu Hu
 Prof. Jonathan Li, P. Eng
 Liyuan Qing
 Weikai Tan
 Jianshen Wang
 Qiutong Yu
 Dedong Zhang
 Zhehan Zhang
 Wenxuan Zhu

Cascadia

Douglas Lee Smith, CP

Eastern Great Lakes

Sean R. Cannady
 David Greening

Florida

George Poole, III

Heartland

Derek M. Smith, PT

Intermountain

Kevin Reid, CP

Mid South

Jordan Bartlett Hicks

Pacific Southwest

Lawrence E. Brower
 Jay Ure

Rocky Mountain

Susan Ann Hunter Norman

Western Great Lakes

Jessica Campbell

FOR MORE INFORMATION ON ASPRS
 MEMBERSHIP, VISIT

[HTTP://WWW.ASPRS.ORG/JOIN-NOW](http://www.asprs.org/join-now)

**Your Path To Success In The Geospatial
 Community**

- June 22 – 26, 2020 — Live Technical Sessions daily between the hours of 11 AM and 6 PM Eastern Daylight Time

We hope that the ASPRS 2020 Annual Conference Virtual Technical Program gives our Geo Week 2020 presenters the forum to share their important work publicly without further delays. We also hope that this virtual program will attract many new attendees from around the world who would not have been able to travel to either Washington DC or Chicago for a traditional face-to-face conference. We hope to “see” you there!

If you have any questions or concerns, please contact us by email at programs@asprs.org.

ASPRS HOSTED GEOSPATIAL WEBINARS FOR KIDS

ASPRS hosted three one-hour educational webinars for kids. These webinars were focused on geospatial concepts and technology. GeoBits, based on our successful GeoBytes Series, were free for the general public and were recorded.

The 1st GeoBit, **Career Opportunities in Land Surveying**, was presented by Ryan Swingley, *ESP Associates*. This session presented career opportunities in the exciting world of land surveying. What is it like to be a surveyor? How does land surveying affect the physical world around us? What are the different career segments in land surveying and the future job outlook?

The 2nd GeoBit, **Studying Population Change using Interactive Mapping Tools**, was presented by Joseph Kerski, *Esri*. This session explored patterns of population change, migration, and demography with interactive web maps and web mapping applications.

The 3rd GeoBit, **Product Management, 3D, and Maps**, was presented by Chris Andrews, *Esri*. This session discussed how product management is the art and science of guiding development of a product from concept to sale to use by a real-world person to accomplish work.

To view the recordings, visit <https://www.asprs.org/Geobytes.html>.

SUSTAINING MEMBERS

ACI USA Inc.

Weston, Florida
acicorporation.com
Member Since: 1/2018

Aerial Services, Inc.

Cedar Falls, Iowa
www.AerialServicesInc.com
Member Since: 5/2001

Airbus Defense and Space

Chantilly, Virginia
www.intelligence-airbusds.com
Member Since: 11/2018

Ayres Associates

Madison, Wisconsin
www.AyresAssociates.com
Member Since: 1/1953

Bohannon Huston, Inc.

Albuquerque, New Mexico
www.bhinc.com
Member Since: 11/1992

Cardinal Systems, LLC

Flagler Beach, Florida
www.cardinalsystems.net
Member Since: 1/2001

Dewberry

Fairfax, Virginia
www.dewberry.com
Member Since: 1/1985

Environmental Research Incorporated

Linden, Virginia
www.eri.us.com
Member Since: 8/2008

Esri

Redlands, California
www.esri.com
Member Since: 1/1987

GeoBC

Victoria, Canada
www.geobc.gov.bc.ca
Member Since: 12/2008

GeoCue Group

Madison, Alabama
info@geocue.com
Member Since: 10/2003

Geojano

Pleasanton, California
https://geojano.com/
Member Since: 05/2019

GeoWing Mapping, Inc.

Richmond, California
www.geowingmapping.com
Member Since: 12/2016

Global Science & Technology, Inc.

Greenbelt, Maryland
www.gst.com
Member Since: 10/2010

GPI Geospatial Inc.

formerly **Aerial Cartographics of America, Inc. (ACA)**
Orlando, Florida
www.aca-net.com
Member Since: 10/1994

Green Grid Inc.

San Ramon, California
www.greengridinc.com
Member Since: 1/2020

Kucera International

Willoughby, Ohio
www.kucerainternational.com
Member Since: 1/1992

L3Harris Corporation

Broomfield, Colorado
www.harris.com
Member Since: 6/2008

Martinez Geospatial, Inc. (MTZ)

Eagan, Minnesota
www.mtzgeo.com
Member Since: 1/1979

Pickett and Associates, Inc.

Bartow, Florida
www.pickettusa.com
Member Since: 4/2007

Quantum Spatial, Inc.

Sheboygan Falls, Wisconsin
www.quantumspatial.com
Member Since 1/1974

Robinson Aerial Survey, Inc. (RAS)

Hackettstown, New Jersey
www.robinsonaerial.com
Member Since: 1/1954

Routescene, Inc.

Durango, Colorado
www.routescene.com/
Member Since: 12/2007

Sanborn Map Company

Colorado Springs, Colorado
www.sanborn.com
Member Since: 10/1984

Towill, Inc.

San Francisco, California
www.towill.com
Member Since: 1/1952

Trimble

Munich, Germany
www.trimble.com/geospatial
Member Since: 4/19942

U.S. Geological Survey

Reston, Virginia
www.usgs.gov
Member Since: 4/2002

Woolpert LLP

Dayton, Ohio
www.woolpert.com
Member Since: 1/1985

Call for Submissions

Special Issue on Urban Remote Sensing

Photogrammetric Engineering and Remote Sensing (PE&RS) is seeking submissions for a special issue on Urban Remote Sensing.

The formulation of the 17 Sustainable Development Goals (SDGs) is a major leap towards humankind's quest for sustainability. In recent decades, global urban areas have been rapidly expanding, especially in developing countries. The prospect is that the urbanization rate will reach 60% by 2030. Urban expansion will inevitably increase vulnerability to natural hazards, natural vegetation cover decline and arable land loss, urban heat islands, air pollution, hydrological cycle alteration and biotic homogenization. Since urban ecosystems are strongly influenced by anthropogenic activities, a considerable amount of research has been conducted all around the world to understand the spatial patterns, driving forces and the ecological and social consequences of urbanization. It is not only crucial for characterizing the ecological consequences of urbanization but also for developing effective economic, social and environmental policies in order to mitigate its adverse impacts.

Remote sensing has been widely used for investigating urban environment and the associated drivers during the urbanization process, as it can quickly and frequently monitor large area surface change with lower cost, compared to field survey or in situ measurements. Digital archives of remotely sensed data provide an excellent opportunity to study historical urban changes and to relate their spatio-temporal patterns to environmental and human factors. With the rapid development of Earth observation techniques, it has become convenient to obtain a large number of remotely-sensed imagery over a certain area at different times, from hundreds of Earth observation platforms. However, this brings challenges to researchers to timely process the remote sensing big data as well as to rapidly transfer the data into information and knowledge.

Considering this, this special issue of *PE&RS* is aimed at reporting novel studies on exploiting remote sensing big data to monitor and improve urban environment, and showing the potential of remote sensing in developing sustainable cities, including but not limited to:

- Urban remote sensing big data
- Remote sensing information interpretation
- Urban expansion, dynamics and associated environment consequences
- Remote sensing of urban water quality

- Remote sensing of urban thermal environment
- Remote sensing of urban geological environment
- Urban sustainability assessment
- Urban sustainable development
- Urban Spatiotemporal analysis
- Urban Sustainability Indicators
- Urban environmental Monitoring

Papers must be original contributions, not previously published or submitted to other journals. Submissions based on previous published or submitted conference papers may be considered provided they are considerably improved and extended. Papers must follow the instructions for authors at <http://asprs-pers.edmgr.com/>.

Important Dates

- July 1, 2020 Submission system opening
- October 31, 2020 Submission system closing
- Planned publication date: Dec. 2020
- Submit your manuscript to <http://asprs-pers.edmgr.com/> by Oct. 31, 2020.

Guest Editors

Zhenfeng Shao, *Wuhan University, China*

Prof. Zhenfeng Shao, Professor at the State Key Laboratory of Information Engineering in Surveying, Mapping and Remote Sensing, Wuhan University, China. His research interests include urban remote sensing. He is now an associate editor of Email: shaozhenfeng@whu.edu.cn.

Orhan Altan, *Istanbul Technical University, Turkey*

Prof. Orhan ALTAN, Professor at the Department of Geomatics Engineering, Istanbul Technical University, Turkey. He is Past President and Honorary Member of ISPRS, Honorary Member of Science Academy. He has published more than 200 scientific papers in scientific journals and conferences, and editor or co-editor of more than 20 international books. Email: oaltan@itu.edu.tr

J.L.van Genderen, *University of Twente, Netherlands*

Professor J.L.van Genderen, Prof. at the Department of Earth Observation Science, Faculty of Geo-information Science and Earth Observation(ITC),University of Twente, Netherlands, he is an associate Editor of Geo-Spatial Information Science. His research interests include photogrammetry and remote sensing, urban remote sensing and computer vision. Email: Genderen@alumni.itc.nl.

Trajectory Drift-Compensated Solution of a Stereo RGB-D Mapping System

Shengjun Tang, Qing Zhu, You Li, Wu Chen, Bo Wu, Renzhong Guo, Xiaoming Li, Chisheng Wang, and Weixi Wang

Abstract

Multiple sensors are commonly used for three-dimensional (3D)-mapping or robotic-vision applications, as they provide a larger field of view and sufficient observations to fulfill frame-registration and map-updating tasks. However, the data sequences generated by multiple sensors can be inconsistent and contain significant time drift. In this paper, we describe the trajectory drift-compensated strategy that we designed to eliminate the influence of time drift between sensors, remove the inconsistency between the sequences from various sensors, and thereby generate a coarse-to-fine procedure for robust camera-tracking based on two-dimensional-3D observations from stereo sensors. We present the mathematical analysis of the iterative optimizations for pose tracking in a stereo red, green, blue plus depth (RGB-D) camera. Finally, complex indoor scenario experiments demonstrate the efficiency of the proposed stereo RGB-D simultaneous localization and mapping solution. The results verify that the proposed stereo RGB-D mapping solution effectively improves the accuracies of both camera-tracking and 3D reconstruction.

Introduction

Recently, the widespread availability of red, green, blue plus depth (RGB-D) sensors, such as Google Tango, Kinect V1, Kinect V2, and Structure Sensor has led to substantial progress in three-dimensional (3D) scanning for indoor mapping, as this sensor equipment is inexpensive, lightweight, and has high-quality 3D-perception capabilities (Endres *et al.* 2012; Mur-Artal and Tardos 2017; Newcombe *et al.* 2011). In effect, this technology can be regarded as a combination of laser and visual systems that enables synchronous, high-speed capture of depth and intensity data. Thus, due to financial constraint and accuracy requirements, RGB-D sensors are the optimal choice for indoor 3D reconstruction.

Many researchers have endeavoured to combine information from single RGB-D sensors (Henry *et al.* 2014; Kerl, Stuckler, and Cremers 2015; Mur-Artal and Tardos 2017; Newcombe *et al.* 2011; Olivier *et al.* 2018; Whelan *et al.* 2015). However, the accuracy and precision of indoor 3D reconstruction with RGB-D devices is highly dependent on the accuracy and robustness of the frame registration and

global-optimization processing. Moreover, the frame-matching procedures of single RGB-D mapping systems fail when insufficient features are present in the available fields-of-view of scenes (Chow *et al.* 2014).

One solution to this problem is the use of visual simultaneous location and mapping (SLAM) algorithms, which benefit from a large field of view (Davison, Cid, and Kita 2004). To achieve more robust locating and mapping during visual SLAM, robotics researchers' use of multiple cameras has recently grown, because multiple cameras enable a larger field of view and yield a greater number of observations for frame-registration and map-updating tasks. This implies that the robustness of camera-tracking can be improved by extending the SLAM solution from a monocular camera to multiple cameras (Mazaheri Tehrani 2015).

So far, multiple RGB-D mapping systems of different configurations have been developed. The researchers responsible concluded that accurate calibration and data synchronization of multiple RGB-D cameras are an important prerequisite for such systems (Chen *et al.* 2018; Yang *et al.* 2015; Yong *et al.* 2011). Typically, the calibration of a multiple camera systems is achieved using an optical approach or a geometric approach. The optical approach enables the location of the rigid transformation by minimizing the reprojection error of all correspondences in two-dimensional (2D) space, and the geometric approach obtains the calibration parameters by minimizing the residual error of all 3D correspondences. However, even after using a careful calibration method to reduce the influence of the depth error, the alignment from the global registration is inaccurate due to the inconsistencies of distance measurement-error spreading over the depth frames (Deng *et al.* 2014). Furthermore, because synchronization of multiple RGB-D sensors is not practical, significant trajectory drift exists between different sensors.

We address this problem by developing a trajectory drift-compensated (Td-C) solution for stereo RGB-D mapping, which enables the use of observations from multiple views for accurate camera-tracking. Thus, our Td-C model is used to eliminate the inconsistencies of measurements between the data from different sensors. After presenting a literature review on the RGB-D mapping solutions, we introduce a novel camera calibration procedure that incorporates intrinsic calibration for single sensors and a coarse-to-fine boresight calibration for stereo RGB-D sensors. A Td-C model is then presented in detail for accurate synchronization between data streams from different sensors, and a coarse-to-fine multiple camera-tracking method is introduced for map updating tasks. The performance and robustness of the proposed solution is validated using two sets of data sets collected in real scenes. Finally, conclusions and recommendations for future work are presented.

Shengjun Tang, You Li, Renzhong Guo, Xiaoming Li, Chisheng Wang, and Weixi Wang are with the Guangdong Key Laboratory of Urban Informatics & Shenzhen Key Laboratory of Spatial Smart Sensing and Services & Guangdong Laboratory of Artificial Intelligence and Digital Economy (SZ) & Research Institute for Smart Cities, School of Architecture and Urban Planning, Shenzhen University, Shenzhen, PR China.

Qing Zhu is with the Faculty of Geosciences and Environmental Engineering of Southwest Jiaotong University, Chengdu, P.R. China.

Wu Chen and Bo Wu are with the Department of Land Surveying and Geo-Informatics, Hong Kong Polytechnic University, Hung Hom, Kowloon, Hong Kong.

Corresponding authors: Chisheng Wang and Weixi Wang (sherwoodwang88@gmail.com; wangwx@szu.edu.cn)

Photogrammetric Engineering & Remote Sensing
Vol. 86, No. 6, June 2020, pp. 359–372.
0099-1112/20/359–372

© 2020 American Society for Photogrammetry
and Remote Sensing

doi: 10.14358/PERS.86.6.359

Related Work

In recent years, a great many 3D dense mapping and visual SLAM solutions based on RGB-D devices have been proposed. State-of-art RGB-D mapping studies usually use a single sensor to gather point clouds, and RGB-D SLAM systems can generally be categorized as dense, sparse, or direct according to their method of frame registration.

The first dense-tracking system, KinectFusion, was designed for single RGB-D modelling and functioned by registering the depth-frame and point-cloud streamed from the sensor into a single global volumetric model. To achieve real-time camera updating, the iterative closest points (ICP) algorithm was used to track the streamed RGB-D frame to a global surface model (Newcombe *et al.* 2011). However, the proposed SLAM system consumed a large amount of computer resources and its working range was limited to volumes of less than 7 m^3 . Moreover, the dense tracking system ignored the cumulative drift-error that occurs during processing of frame-by-frame tracking. Subsequently, extensive efforts were made to reduce the computational burden of dense tracking, as exemplified by the development of an improved KinectFusion system (Whelan *et al.* 2012; Whelan *et al.* 2016), a volumetric reconstruction based on a spatial hashing scheme (Nießner *et al.* 2013), and KinectFusion with Octree (Zeng *et al.* 2012). Nowadays, a global optimization method is used for reducing the drift error during SLAM (Dubbelman and Browning 2013; Grisetti *et al.* 2011). In addition, the depth measurements and RGB image sequence can be integrated to enable an extended mapping-range and coverage (Wu *et al.* 2019).

In another advance, sparse, feature-based SLAM systems can be used. As unlike dense RGB-D SLAM systems, the former use few feature-matching points for camera pose updating and mapping tasks. This greatly reduces the computational cost, meaning that the sparse, feature-based system can be used for scene mapping over a larger range. The early feature-based RGB-D SLAM system proposed by Engelhard *et al.* (2011) used speeded-up robust features for feature detection. The 2D feature-matches detected from the adjacent color frames were then mapped to the corresponding depth frames, which transformed the features from 2D to 3D. Then, all 3D matches were used for camera pose estimation and a vertex-edge graph optimization method was used to reduce the trajectory drift during pose-tracking. Extensive efforts were also made to enhance the robustness and accuracy of camera-tracking. These efforts involved investigation of the robustness, accuracy, and time-efficiency of various kinds of feature descriptors and matches (Endres *et al.* 2014;

Henry *et al.* 2012; Mur-Artal and Tardos 2017), estimation of the camera motion by integration of different types of features (Kerl *et al.* 2013; Kim, Coltin, and Kim 2018; Le and Kosecka 2017; Shi *et al.* 2018; Tang *et al.* 2018; Zeng *et al.* 2017), and exploration of the uncertainty of depth measurements (Park *et al.* 2012; Tang *et al.* 2019; Vestena *et al.* 2016).

To enhance the tracking performance in textureless regions, the direct sparse odometry (DSO) method was proposed by Alismail, Browning, and Lucey (2016) and Engel, Koltun, and Cremers (2017). The DSO method does not depend on keypoint detectors or descriptors; rather, it can naturally sample pixels from across all image regions that have intensity gradients, including edges or smooth intensity variations on essentially featureless walls. Gao *et al.* (2018) improved the DSO method, developing an extended DSO method with loop-closure handling. Furthermore, Schops, Sattler, and Pollefeys (2019) recently proposed a direct Bundle Adjustment approach to ensure global consistency during RGB-D SLAM; this approach enables simultaneous optimization of poses and geometry, thus limiting the size of the individual optimization problems.

However, the above-mentioned RGB-D mapping system is equipped with a single camera, which means that the camera pose tracking algorithm may easily fail in complex environments due to the very limited field of view of single camera, meaning it fails to identify a sufficient number of visual features (Chen *et al.* 2018). Furthermore, the 3D scenes obtained by a single RGB-D sensor are often incomplete due to occlusion and the sensor's limited scanning range. In another approach, the utilisation of multiple sensors has been a popular option in a variety of mapping applications as it can provide sufficient measurements to fulfill the requirements of frame-registration and map-updating tasks (He and Habib 2018). This means that it is possible to achieve better accuracy and more robust camera-tracking by using a multiple sensor setup. In their early research, Fuhrmann, Langguth, and Goesele (2014) and Pless (2003) constructed a multiple visual camera system for mapping. They presented the theoretical detail of utilisation of multi-camera systems in structure-from-motion studies. Kaess and Dellaert (2006) introduced an eight-camera rig system for better camera-tracking, and described a sparse SLAM approach for real-time reconstruction from multi-camera configurations. Hee Lee, Faundorfer, and Pollefeys (2013) presented a visual ego-motion estimation algorithm for a self-driving car, which was equipped with a multi-camera system. They also introduced a generalized camera model for a multi-camera system by using a two-point random-sample consensus (RANSAC)

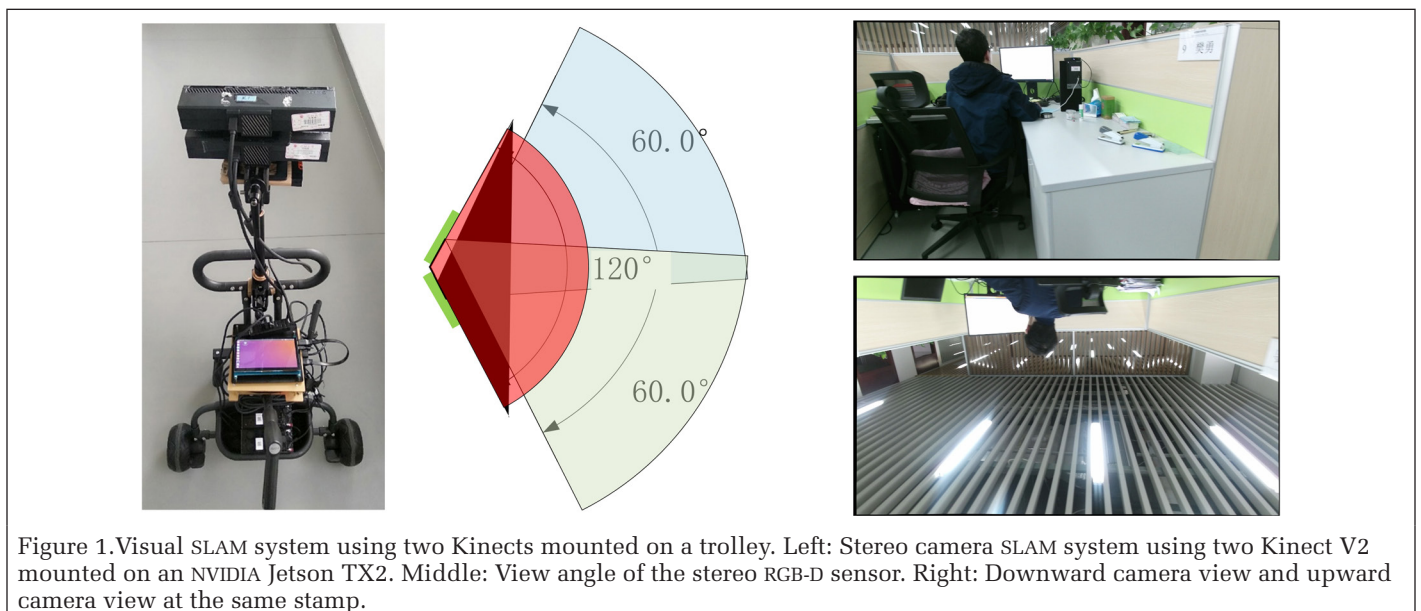


Figure 1. Visual SLAM system using two Kinects mounted on a trolley. Left: Stereo camera SLAM system using two Kinect V2 mounted on an NVIDIA Jetson TX2. Middle: View angle of the stereo RGB-D sensor. Right: Downward camera view and upward camera view at the same stamp.

scheme. Based on the parallel tracking and mapping system (Klein and Murray 2007), a stereo-camera visual SLAM system was proposed by Yang, Scherer, and Zell (2014), in which the iterative optimizations for pose tracking and map refinement that use the observations from stereo cameras were detailed and verified. The results of their experiments implied that their proposed system was more resistant to tracking failure than a monocular method. Furthermore, Yang, Scherer, and Zell (2016) presented a more robust SLAM solution for modular autonomous vehicle systems (MAVs) based on a dual-camera system, in which they used the integrated loop-closure detection and global optimization processes to achieve better tracking accuracy. The loop-closing method is especially important in multiple camera SLAM, and Lee, Fraundorfer, and Pollefeys (2013) introduced a structureless pose-graph loop-closure framework in which the relative pose was obtained from the epipolar geometry of the multiple camera system.

To the best of the authors' knowledge, multiple RGB-D mapping systems have rarely been investigated. Chow *et al.* (2014) constructed a hybrid mobile-mapping system with an inertial measurement unit, two Kinect sensors, and a laser scanner. However, instead of tracking with the observations from multiple views, a point-to-plane ICP algorithm was used for tracking each Kinect pose individually, and then integrated into an implicit iterative-extended Kalman filter. Yang *et al.* (2015) introduced a stereo RGB-D SLAM system, which involved all observations detected from the adjacent frames being streamed from multiple cameras for camera-tracking. They compared the results from a single-sensor and dual-Kinect system, and found that the latter provided better pose-tracking performance and achieve higher mapping-accuracy. However, there are two problems with the Yang *et al.* (2015) approach. First, the potential tracking error in SLAM was not considered in the external calibration procedure for stereo sensors, and thus loop-closure detection was not implemented. Second, the system ignored the significant time drift of data streamed from different sensors, which may result in inaccurate camera-tracking. Chen *et al.* (2018) introduced a triple RGB-D system mounted horizontally on a rig. In this system, sensors were driven with the opensource frame OpenKinect. However, instead of a SLAM framework, they concentrated on calibrations of single and multiple sensors, and verified the effectiveness of mapping using multiple RGB-D cameras. However, the external calibration in this work was

achieved with a global rigid transformation by minimizing the residual error of all correspondences, which ignored the inconsistencies in the accuracy of correspondences. Thus far, several multiple RGB-D mapping systems have been developed and introduced, and it has been found that accurate calibration and data synchronization of multiple RGB-D cameras are a prerequisite for these systems (Chen *et al.* 2018; Yang *et al.* 2015; Yong *et al.* 2011).

However, as mentioned above, existing multiple RGB-D mapping systems achieve extrinsic calibration based on the traditional chessboard, which may generate inaccurate registration due to the inconsistencies of distance measurement-error spreading over the depth frame. Meanwhile, the manipulation of data synchronization for data sequences from different sensors has not been addressed. Therefore, this study focuses on these problems and presents a Td-C solution for stereo RGB-D mapping.

Our work is innovative for two reasons. First, in consideration of the influences of depth errors on external calibration results, a careful calibration procedure is presented in detail. Second, a Td-C model specifically designed for data synchronization between multi-sensors is incorporated into a coarse-to-fine multiple camera-tracking procedure.

Coarse-to-Fine Stereo RGB-D Camera Tracking

Overview of Approach

Herein we present a Td-C solution for stereo RGB-D SLAM that eliminates the influence of time drift between cameras during motion-tracking. Figure 2 shows the framework of our Td-C solution for stereo RGB-D mapping, which consists of a calibration, a front-end, and a back-end. The calibration work is separated into two parts: calibration of a single RGB-D sensor, and calibration of the stereo-RGB-D sensors. First, the camera parameters for the single sensor are obtained with a standard camera calibration process. Second, we use a coarse-to-fine calibration scheme to calibrate the stereo-RGB-D sensors, solve the initial exterior orientation parameters (E_oPs) from sparse control markers, and further refine the initial value by an ICP variant that minimizes the distance between the RGB-D point clouds from the reference and the slave sensors.

Although a fixed rigid transformation should in theory be sufficient to register the frames with the same time stamp from

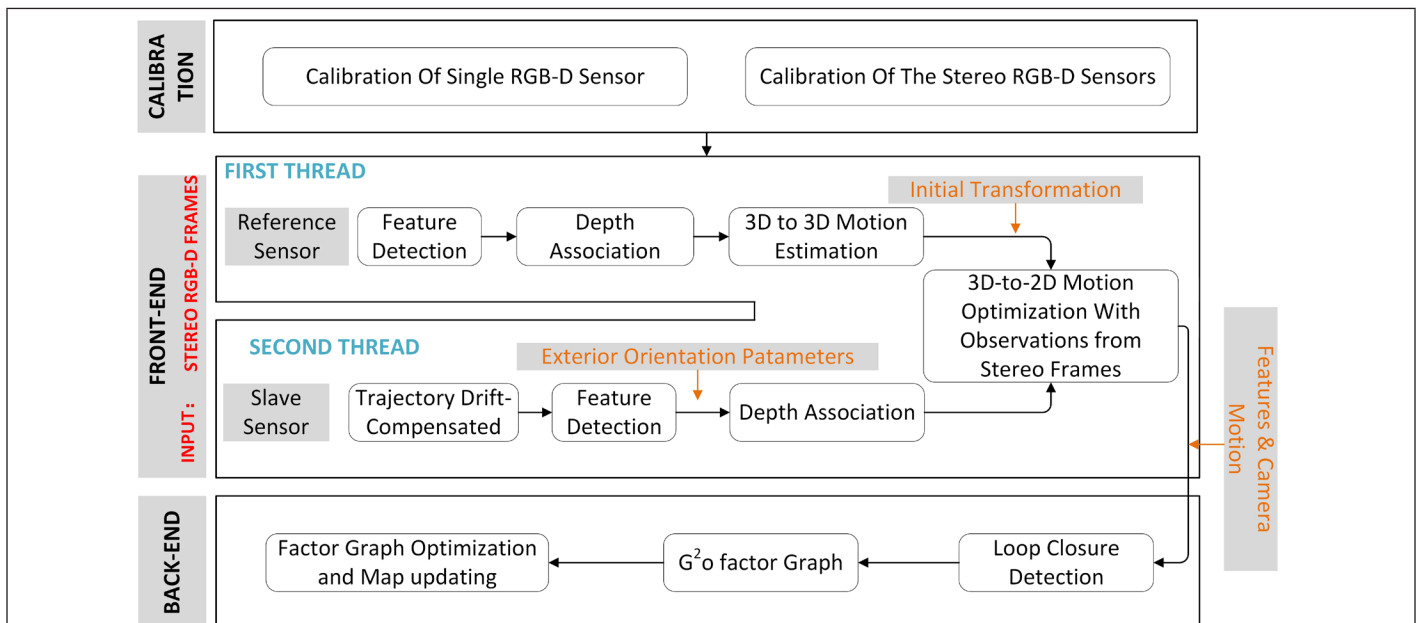


Figure 2. Framework of Td-C solution for stereo RGB-D mapping (where g2o stands for general (hyper)graph optimization).

two sensors, multiple Kinect sensors cannot be synchronized due to hardware limitations. This results in significant time drift between the published RGB-D streams of different sensors, which may cause inaccurate registration. To compensate for this time drift between data streams from different sensors and enable the use of observations from stereo sensors, we separate the stereo RGB-D tracking into two threads. In the first thread, reference camera pose tracking is conducted, and the 2D and 3D feature matches detected with adjacent RGB-D frames are used for pose-recovery. The second thread involves first integrating the trajectory drift-compensated strategy to avoid inconsistency between the streams from different sensors.

In particular, in this approach the frame streamed from the reference sensor is defined as the “reference frame” and the frame from the slave sensor is defined as the “slave frame”. To facilitate the use of stereo RGB-D tracking, we collectively define the frames captured with the same time stamp or a minimum time-difference in different sensors as a “bundle frame”, which is to be used for motion optimization by integrating all observations from stereo views. Therefore, to reduce the influence of time drift in bundle frames, a trajectory-compensated strategy is applied to translation, and rotation is introduced to recover an accurate relationship between the slave frame and the reference frame. It should be noted that the drift of the translation and rotation of each “bundle frame” depends on the time-difference and movement speed of the system. After this, the new compensated keyframes from the slave sensor are integrated for pose refinement and used to create new map points. Finally, experiments in complex indoor scenarios demonstrate the efficiency of our proposed multiple RGB-D SLAM algorithm.

RGB-D Sensor Calibration

The calibration procedure is divided into two threads. The first thread handles the intrinsic calibration of the RGB and depth cameras’ geometric parameters, namely focal length, principal point, and distortion parameters, and calibrates the RGB-D baseline. The core concept of intrinsic calibration of a single sensor is based on the pinhole camera model, which represents the relationship between the 2D image-point and the corresponding 3D ground point as a function of the camera’s internal and external parameters.

The second thread deals with the calibration for EoPs, which enables precise registration of the point cloud from different sensors. In this work, we derive the accurate EoPs by minimizing the residual errors of 3D correspondences; the 3D cone-markers shown in Figure 3a and 3b are used for calibration purposes to ensure the consistent measurement accuracy of correspondences. The feature matches are detected

from RGB images by a scale-invariant feature transform (SIFT) operator (Lowe 2004). The corresponding 3D point pairs are obtained by mapping feature-matches to depth images, in which P^r and P^s represent the peak points of 3D cones in the reference sensor and the slave sensor, respectively. Using RANSAC and the least-squares method, the optimal rigid transformation T_s^r between the downward and upward cameras can initially be calculated by minimizing the cost function according to Equation 1 below:

$$T_s^r = \underset{T}{\operatorname{argmin}} \left(\frac{1}{|A|} \sum_{i \in A} w_i |T(P_r^i) - P_s^i|^2 \right) \quad (1)$$

Here, $P_r^i \triangleq T_s^r \cdot P_s^i$, where T_s^r consists of a rotation matrix R and a translation t , A contains the associations between feature points of the frames from two sensors, and w_i is the weight for each point based on the theoretical error-of-depth measurement (Khoshelham and Elberink 2012). After that, we further refine the EoPs T_s^r with an ICP variant by minimizing the distance between the point cloud from two sensors. As shown in Figure 3c and 3d, the point clouds from the reference sensor and the slave sensor are captured at the same time and can thus be registered with high precision. Quantitatively, the recovered external parameter provides a 0.006-m root-mean-square error (RMSE).

Trajectory Drift-Compensated (Td-C) Approach

During the stereo RGB-D mapping, two sets of RGB-D data sets are streamed, and each frame is labeled with its corresponding time stamp. To facilitate the use of stereo RGB-D tracking, we collectively define the frames captured with the same time stamp or minimum time difference in different sensors as a “bundle frame”, which is to be used for motion optimization by integrating all observations from stereo views. Although a fixed rigid transformation obtained by the external calibration method in the section “RGB-D Sensor Calibration” should in theory be sufficient to register the frames in a bundle frame, multiple Kinect sensors cannot be synchronized, and a significant time drift can thus be seen in the frames of a bundle frame due to the unstable topic-publishing rate of sensors. As shown in Figure 4, this time drift in each bundle frame is plotted together with the sensor trajectory, in which the RGB-D data sets are streamed at 5 Hz. As measured, for each bundle frame there is an average 0.03 s time drift between the frames captured by different sensors.

As demonstrated in Figure 4, the sensors are synchronized with the network time protocol time service, which enables millisecond-level synchro error. This means that the starting

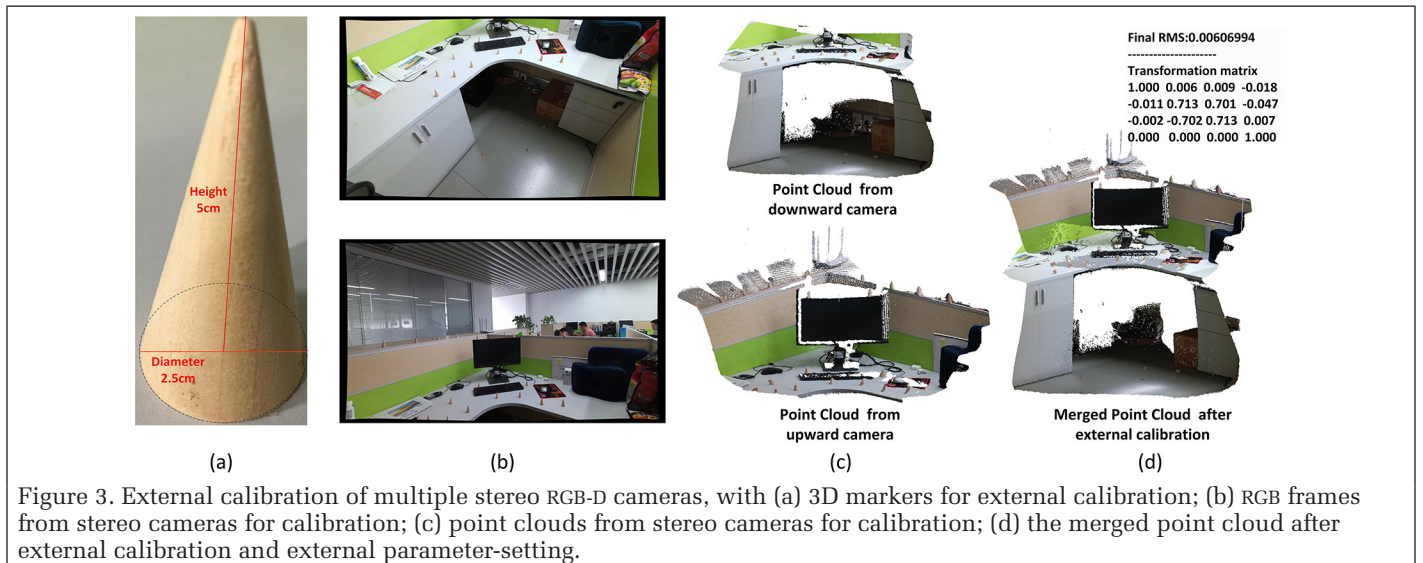


Figure 3. External calibration of multiple stereo RGB-D cameras, with (a) 3D markers for external calibration; (b) RGB frames from stereo cameras for calibration; (c) point clouds from stereo cameras for calibration; (d) the merged point cloud after external calibration and external parameter-setting.

frames that are captured by different sensors generally share the same time stamp and that the drift is negligible. As shown in Figure 5b, the blue box represents one bundle frame, which consists of one frame plotted with the blue dot and one frame plotted with the red dot, representing data captured by the reference sensor and slave sensor, respectively. In this condition, the frames from reference F^r and the slave sensor F^s can be precisely registered with the calibrated external parameter T_s^r , as shown in the left of Figure 5a.

As mentioned above, time drift in the frames of a bundle frame is inevitable. As shown in the right of Figure 5a, a significant time drift exists between F^r and F^s in condition 2. To enable accurate use of observations from multiple cameras, T^{drift} is applied to compensate for the drift of each bundle frame. A Td-C strategy is proposed to derive the compensating transformation and to eliminate the discrepancy of the data streams from the reference and the slave sensors.

In this Td-C strategy, we derive the accurate trajectory drift for each bundle frame in a spatially variant way. In Figure 5b, two bundle frames, $BF1$ and $BF2$, represent the adjacent key bundle frames captured by stereo sensors, which consist of $BF1^r$ and $BF1^s$, and $BF2^r$ and $BF2^s$, respectively. By mapping the time stamp of the slave frame $BF1^s$ to the timeline of the reference sensor, we hypothesize that one fictitious frame $BF1^f$ exists in the data stream of the reference sensor, which is denoted by the same time stamp of $BF1^s$ and plotted with a yellow dot in Figure 5b. Therefore, frame $BF1^s$ and frame $BF1^f$ can be precisely registered according to Equation 4 (below),

and the relation of $BF1^f$ and $BF1^r$ can be described by Equation 3 (below). Based on Equations 2 and 3, an accurate relative pose of the reference frame $BF1^r$ and the slave frame $BF1^s$ in $BF1$ can then be derived as Equation 4, below.

$$BF1^r = T_s^r \cdot BF1^s \quad (2)$$

$$BF1^r = T^{\text{drift}} \cdot BF1^f \quad (3)$$

$$BF1^r = T^{\text{drift}} \cdot T_s^r \cdot BF1^s \quad (4)$$

From a global perspective, the camera pose is in a nonlinear variant rule. In our method, only two adjacent key bundle frames are considered and used for trajectory drift compensation. Locally, we hypothesize that the translation and rotation vary linearly with time. Therefore, in our method, a linear basis is imposed on the translation and rotation to recover the accurate relative pose T^{drift} of the fictitious frame $BF1^f$ and the reference frame $BF1^r$. Using $\text{ts.interval} = ||\text{ts}^{BF2^r} - \text{ts}^{BF1^r}||$ to represent the time interval between $BF1^r$ and $BF2^r$, and $\text{ts.drift} = ||\text{ts}^{BF1^s} - \text{ts}^{BF1^r}||$ for the time drift in $BF1$, which is the time difference of the frame captured by the reference sensor and the frame captured by the slave sensor, a scale parameter S is computed using Equation 5, as follows:

$$S = \frac{\text{ts.drift}}{\text{ts.interval}} = \frac{||\text{ts}^{BF1^s} - \text{ts}^{BF1^r}||}{||\text{ts}^{BF2^r} - \text{ts}^{BF1^r}||}, \text{ with } S \in [0, 1] \quad (5)$$

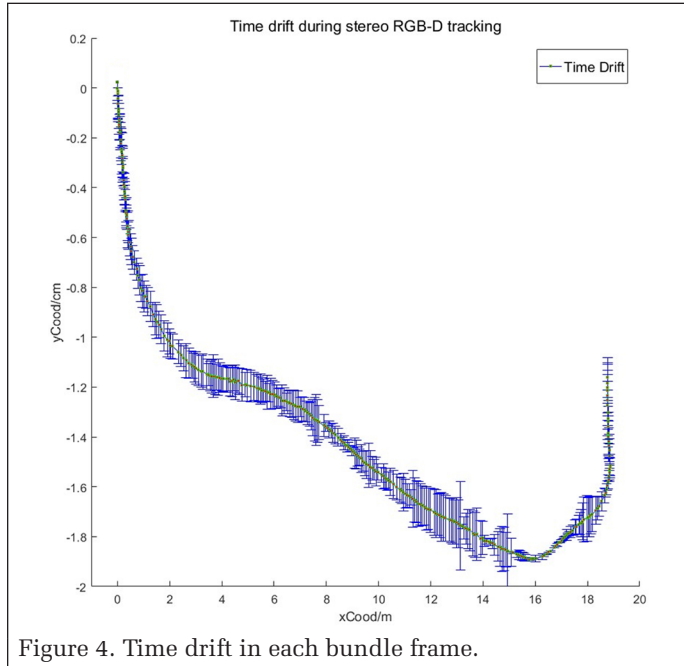


Figure 4. Time drift in each bundle frame.

where ts is the time stamp of a specific frame, ts^{BF1^r} is the time stamp of the reference frame in the i^{th} “bundle frame”, and similarly, ts^{BF1^s} is the time stamp of the slave frame in the i^{th} “bundle frame”. It should be noted that the acquisition time of the slave frame $BF1^s$ is always located between the time stamp of $BF2^r$ and $BF1^r$. Therefore, the value S always lies in interval $[0, 1]$. As the SLAM framework is separated into two threads, the camera motion $T_{BF1^r} = (t_{BF1^r}, \text{rot}_{BF1^r})$, $T_{BF2^r} = (t_{BF2^r}, \text{rot}_{BF2^r})$ of $BF1^r$ and $BF2^r$ is derived in the first thread. Using the linear basis, the camera position $t_{BF1^r}^T = (x_{BF1^r}, y_{BF1^r}, z_{BF1^r})^T$ of the fictitious frame $BF1^f$ can then be calculated using Equation 6, as follows:

$$t_{BF1^r}^T = t_{BF1^r}^T + S \cdot (t_{BF2^r}^T - t_{BF1^r}^T) \quad (6)$$

where $t_{BF1^r}^T = (x_{BF1^r}, y_{BF1^r}, z_{BF1^r})^T$ is the camera position of frame $BF1^r$, and $t_{BF2^r}^T = (x_{BF2^r}, y_{BF2^r}, z_{BF2^r})^T$ is the camera position of frame $BF2^r$.

Similarly, a linear basis is used to interpolate rotation quantities. This is achieved by the spherical linear interpolation (slerp) operation, which interpolates the rotation over the sphere, as shown in Equation 7:

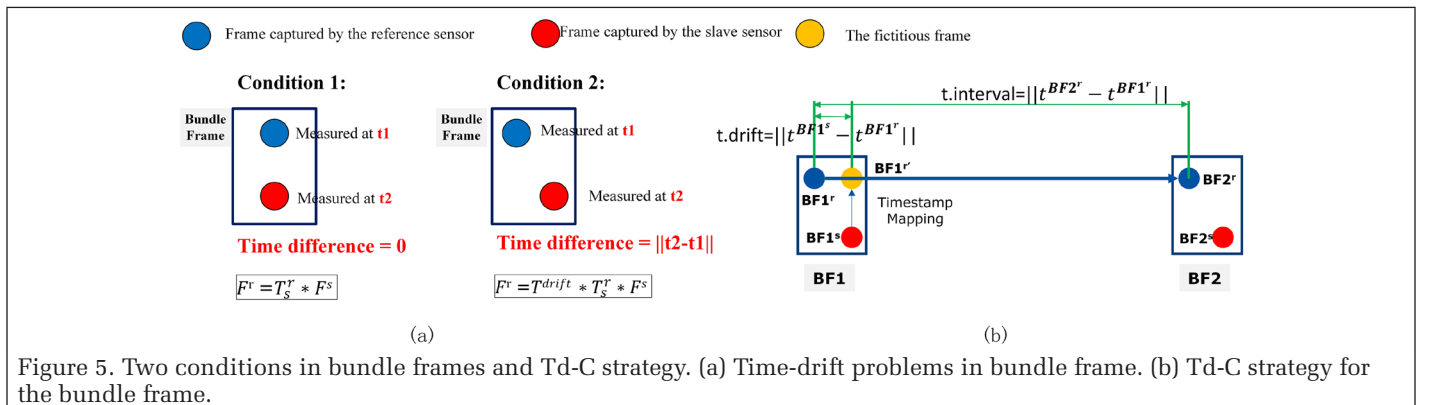


Figure 5. Two conditions in bundle frames and Td-C strategy. (a) Time-drift problems in bundle frame. (b) Td-C strategy for the bundle frame.

$$\begin{aligned} \text{rot}_{BF1^r} &= \text{slerp}(S, \text{rot}_{BF1^r}, \text{rot}_{BF2^r}) = \\ & \frac{\sin((1-S)\alpha)}{\sin(\alpha)} \cdot \text{rot}_{BF1^r} + \frac{\sin(S\alpha)}{\sin(\alpha)} \cdot \text{rot}_{BF2^r} \quad (7) \\ & \text{with } S \in [0, 1] \end{aligned}$$

which linearly interpolates between two quaternions rot_{BF1^r} , rot_{BF2^r} respectively, and where $\cos(\alpha) = \text{rot}_{BF1^r} \cdot (\text{rot}_{BF2^r})^T$. More information on the slerp operation was given by Shoemake (1985).

After that, the camera motion $T_{BF1^r} = (t_{BF1^r}, \text{rot}_{BF1^r})$ of the fictitious frame $BF1^r$ is obtained, and T^{drift} for each bundle-frame can be recovered as Equation 8, as below:

$$T^{\text{drift}} = T_{BF1^r}^{-1} \cdot T_{BF1^r} \quad (8)$$

Coarse-to-Fine Stereo RGB-D Tracking

In our stereo RGB-D visual SLAM system, the camera-tracking module consists of two separate threads. The first thread is responsible for key-frame detection and initial tracking with the data stream from the reference sensor. The second thread is then used for Td-C and pose optimization by integrating all observations from the stereo bundle frames.

Camera Projection Model and Pose Update

In our system, two camera projection models are used, a depth camera projection model, and a camera projection model for pose updating. The depth camera projection model describes the relationships of image space in the depth frame and in local object space. Based on the calibrated internal parameters, i.e., focal length, principle points, and distortions, each pixel with valid measurement information is projected to object space, which enables the corresponding 3D points to be calculated. The depth camera projection model is given by Equation 9, as follows:

$$u_j^i = \frac{1}{d} K^i P_j^i \quad (9)$$

where $u_j^i = (x, y)^T$ are the image coordinates of the j^{th} point of the sensor C_i ; $P_j^i = (X, Y, Z)^T$ are the 3D coordinate of the j^{th} point of the sensor C_i ; d is the corresponding depth value in the depth image, which is equal to the Z value of P_j^i ; and

$$K^i = \begin{bmatrix} f_{dx}^i & 0 & c_{dx}^i \\ 0 & f_{dy}^i & c_{dy}^i \\ 0 & 0 & 1 \end{bmatrix},$$

the interior matrix of the depth camera of sensor C_i .

The depth camera projection is used for 2D–3D mapping from the depth image to 3D space, which provides an absolute constraint during the pose update. Based on the calibrated RGB camera parameters, the camera projection model for the pose update is constructed per Equation 10, as follows:

$$u_j^i = \ell_{C_i}(T_{C_i}^k P_j^i) \quad (10)$$

where ℓ_{C_i} is the projection model of the RGB sensor of sensor C_i with consideration of lens distortion, and $T_{C_i}^k$ is the camera pose of the k^{th} key bundle frame of sensor C_i , which consists of a rotational and a translational component.

In the stereo RGB-D mapping system, the pose update is computed by integrating all observations from all cameras, in which the relative pose of sensors dynamically derived by the Td-C strategy is used as an absolute constraint. The pose update of the reference sensor can be expressed with one transformation matrix μ , where $T_{C_1}^k$ and $T_{C_1}^{k-1}$ are the

reference sensor pose of the k^{th} and $(k-1)^{\text{th}}$ key bundle frame, as described by Equation 11, below:

$$T_{C_1}^k = \mu T_{C_1}^{k-1} \quad (11)$$

The pose of the slave sensor is updated by applying the dynamically derived transformation relative to the reference sensor. The relations between the reference sensor and the slave sensor in the adjacent key-frame can be represented as Equations 12 and 13, as follows:

$$T_{C_1}^k = T^{\text{drift}}_k \cdot T_s^r \cdot T_{C_2}^k \quad (12)$$

$$T_{C_1}^{k-1} = T^{\text{drift}}_{k-1} \cdot T_s^r \cdot T_{C_2}^{k-1} \quad (13)$$

By combining Equations 11, 12, and 13, the pose update for the slave sensor can be derived as the following Equation 14:

$$T_{C_2}^k = (T^{\text{drift}}_k \cdot T_s^r)^{-1} \cdot \mu \cdot T^{\text{drift}}_{k-1} \cdot T_s^r \cdot T_{C_2}^{k-1} \quad (14)$$

Therefore, the problem of the SLAM system now mainly consists of how to obtain an optimized pose update for the stereo RGB-D system.

Initial Camera Tracking with Reference Sensor

In the first thread, initial poses of the reference sensor are derived by minimizing the reprojection error of all observations detected from the adjacent key-frames. In our system, all key points detected by SIFT descriptor and feature matches are obtained with the graphics processing unit (GPU)-SIFT algorithm (Wu 2011). In the initial pose tracking stage, only feature points with valid depth information are used. Therefore, each feature point with valid depth information is projected to object space based on the depth camera projection model. The corresponding 3D coordinates are subsequently used as an absolute constraint during the pose-update calculation. According to Equation 15, the objective function with respect to the reprojection error of all observations (O_j) can be derived and the camera pose update can be achieved by an iterative least squares calculation:

$$F(P_j^i, T_{C_1}^k) = \underset{u}{\text{argmin}} \sum_{i=1} \sum_{j \in O_i} (E_{ji})^T \cdot \Omega_{ji} \cdot (E_{ji}) \quad (15)$$

where $E_{ji} = u_j^i - \bar{u}_j^i$ is the residual error of each feature point, in which u_j^i are the image coordinates detected from the color image, and \bar{u}_j^i are the image coordinates of the reprojection points. Specifically, Ω_{ji} is defined for weight representation, which is related to the reliability of the feature point and represented as an information matrix. It should be noted that the accuracy of depth measurement determines the weight of each correspondence, and in our solution, a feature with a depth less than 5 m is fixed during bundle adjustment to provide an absolute constraint.

In this work, the initial pose of the reference sensor is derived by iteratively solving the problem using a nonlinear least-squares method. To estimate the rotational and translational parameters and optimize the position of correspondences, the corresponding Jacobians related to $T_{C_1}^k$ and P_j^i are derived by differentiating the error model. To enable convenient mathematical computation, quaternions are used to represent roll, yaw, and pitch rotations. Thus, in this solution, for each feature point j in the k^{th} keyframe, the Jacobian matrix of E_{ji} with respect to the parameters of translation and rotation $T_{C_1}^k$ can be derived by using a chain rule, as in Equation 16 below:

$$\mathcal{J}_{T_{C_1}^k} = \frac{\partial(E_{ji})}{\partial(T_{C_1}^k)} = \frac{\partial(E_{ji})}{\partial(C)} \Big|_{C=T_{C_1}^k, P_j^i} \cdot \frac{\partial(C)}{\partial(T_{C_1}^k)} \quad (16)$$

where the first item of the above equation represents the Jacobian matrix of the camera projection function, and the second item is the Jacobian related to the translational and rotational components. The second item is also given by Equation 17, as follows:

$$\begin{aligned} & \frac{\partial(E_{jix})}{\partial(q_0)} \quad \frac{\partial(E_{jix})}{\partial(q_1)} \quad \frac{\partial(E_{jix})}{\partial(q_2)} \quad \frac{\partial(E_{jix})}{\partial(q_3)} \quad \frac{\partial(E_{jix})}{\partial(t_x)} \quad \frac{\partial(E_{jix})}{\partial(t_y)} \quad \frac{\partial(E_{jix})}{\partial(t_z)} \\ & \frac{\partial(E_{jyx})}{\partial(q_0)} \quad \frac{\partial(E_{jyx})}{\partial(q_1)} \quad \frac{\partial(E_{jyx})}{\partial(q_2)} \quad \frac{\partial(E_{jyx})}{\partial(q_3)} \quad \frac{\partial(E_{jyx})}{\partial(t_x)} \quad \frac{\partial(E_{jyx})}{\partial(t_y)} \quad \frac{\partial(E_{jyx})}{\partial(t_z)} \end{aligned} \quad (17)$$

Simultaneously, the 3D position of each map point is also optimized during this iterative processing. We derive the Jacobian matrix of E_{ji} relative to the position P_j^i in a similar way, according to Equation 18:

$$\mathcal{J}_{P_j^i} = \frac{\partial(E_{ji})}{\partial(P_j^i)} = \frac{\partial(E_{ji})}{\partial(C)} \Big|_{C=T_{C_i}^k \cdot P_j^i} \cdot \begin{bmatrix} \frac{\partial(E_{jix})}{\partial(X)} & \frac{\partial(E_{jix})}{\partial(Y)} & \frac{\partial(E_{jix})}{\partial(Z)} \\ \frac{\partial(E_{jyx})}{\partial(X)} & \frac{\partial(E_{jyx})}{\partial(Y)} & \frac{\partial(E_{jyx})}{\partial(Z)} \end{bmatrix} \quad (18)$$

Pose Refinement with a Drift-Compensated "Bundle Frame"

As shown in Figure 6, the poses of the reference frames can be obtained by the initial camera-tracking progress. The trajectory drift in the bundle frame is then compensated for, and the accurate relations between the frames in the bundle frame are recovered.

When stereo RGB-D cameras are used, we use all observations detected from the adjacent bundle frame for bundle adjustment and pose refinement. As defined previously, each bundle frame consists of one frame BF_k^r from the reference sensor and one slave frame BF_k^s from the slave sensor, and the relationship between these can be represented by a rigid transformation as described in Equation 4. Therefore, for the adjacent bundle frames, two sets of 3D observations P_1^m and P_1^n of the corresponding image observations O_1 and O_2 are detected from the adjacent frames of the reference sensor and the slave sensor, respectively. The reprojection error for each set of observations can be represented by Equation 19, as shown below:

$$\begin{aligned} E_{1,k}^m &= \ell_{C_1} \cdot (T_{C_1}^k \cdot P_1^m) - u_{1,k}^m \\ E_{1,k-1}^m &= \ell_{C_1} \cdot (T_{C_1}^{k-1} \cdot P_1^m) - u_{1,k-1}^m \\ E_{2,k}^n &= \ell_{C_2} \cdot (T_{C_2}^k \cdot P_2^n) - u_{2,k}^n, \text{ in which } T_{C_2}^k = T^{\text{drift}} \cdot T_s^r \cdot T_{C_1}^k \\ E_{2,k-1}^n &= \ell_{C_2} \cdot (T_{C_2}^{k-1} \cdot P_2^n) - u_{2,k-1}^n, \text{ in which } T_{C_2}^{k-1} = T^{\text{drift}} \cdot T_s^r \cdot T_{C_1}^{k-1} \end{aligned} \quad (19)$$

Here, $E_{1,k}^m$, $E_{1,k-1}^m$, $E_{2,k}^n$, and $E_{2,k-1}^n$ are the reprojection errors of the feature points of the reference sensor and the slave sensor in the k^{th} and the $(k-1)^{\text{th}}$ key "bundle frame", $T_{C_1}^k$, $T_{C_1}^{k-1}$, $T_{C_2}^k$, and $T_{C_2}^{k-1}$ are the corresponding poses of the k^{th} and the $(k-1)^{\text{th}}$ key bundle frame of the reference and the slave sensor, respectively, in which the relations between the frames in each bundle frame are derived by external calibration and a Td-C processes, $u_{1,k}^m$, $u_{1,k-1}^m$, $u_{2,k}^n$, and $u_{2,k-1}^n$ are the image coordinates of the feature points of the reference sensor and the slave sensor in the k^{th} and the $(k-1)^{\text{th}}$ key bundle frame, and ℓ_{C_1} and ℓ_{C_2} are the projection functions of the RGB camera of sensor C_1 and C_2 , with consideration of lens distortion. Thus, a unified error function can be modelled in Equation 20, as follows below. This method allows the full integration of 2D and 3D observations in O_1 and O_2 .

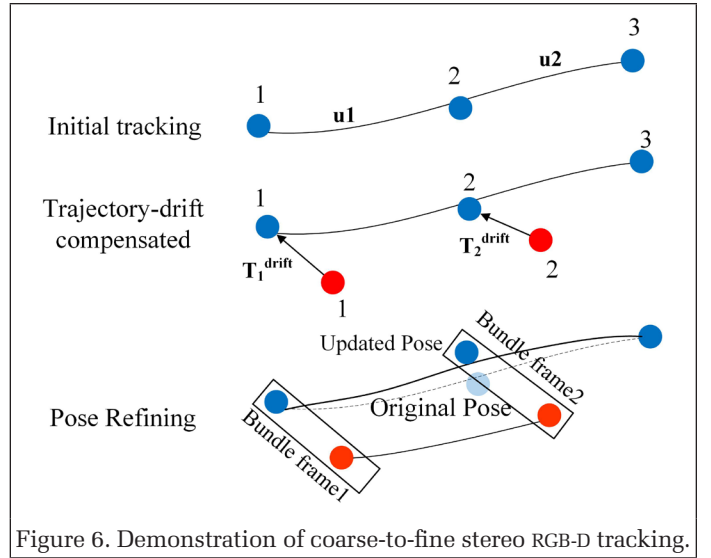


Figure 6. Demonstration of coarse-to-fine stereo RGB-D tracking.

$$\begin{aligned} & F(P_1^m, P_2^n, T_{C_1}^k, T_{C_1}^{k-1}) = \\ & F(P_1^m, P_2^n, T_{C_1}^k, T_{C_1}^{k-1}) = \\ & F(P_1^m, P_2^n, T_{C_1}^k, T_{C_1}^{k-1}) = \\ & + \sum_{n \in O_2} \sum (E_{2,k}^n)^T \cdot \Omega_{j_1} \cdot E_{2,k}^n + \sum_{n \in O_2} \sum (E_{2,k-1}^n)^T \cdot \Omega_{j_1} \cdot E_{2,k-1}^n \end{aligned} \quad (20)$$

For the pose-tracking of stereo sensors, the optimization problem is to find the optimal pose update μ for the system between the $(k-1)^{\text{th}}$ key bundle-frame and the k^{th} key bundle-frame, with reference to Equation 21:

$$\mu = \underset{\mu}{\operatorname{argmin}} (P_1^m, P_2^n, T_{C_1}^k, T_{C_1}^{k-1}) \quad (21)$$

In this condition, the problem is solved iteratively by a nonlinear least-squares method. Thus, the pose updates related to the next key frame can be refined and improved, and the pose of the reference and slave cameras can then be derived by Equations 10 and 13.

The abovementioned work enables robust camera-tracking by integrating all of the observations from the stereo-RGB-D sensors. However, drift-error inevitably occurs during successive frame-registration, which then accumulates over trajectory length and time. In this solution, we use a bag-of-words-based technique (Gálvez-López and Tardos 2012) for loop-closure detection. After that, a vertex-edge pose graph proposed by Grisetti *et al.* (2011) is used to represent the loop-closure constraint, in which vertices contain poses of all key frames, and the edges are the corresponding relations between the key frames obtained during frame alignment. Therefore, the core idea of the global optimization problem is to distribute the error over the whole loop, which is then solved by a nonlinear least-squares optimization.

Experimental Analysis

Data Acquisition and Error Metrics

In our system, all sensors are locked on a stable stem and connected to an NVIDIA nano-development board running Ubuntu 16.04 and ROS Kinetic via a USB 3.0 interface mounted on a trolley, as shown in Figure 1. As the official software development kit for Kinect V2 can only support a single sensor, the open-source driver OpenKinect is used to power the stereo Kinect v2s system for data collection. The RGB-D sensor

comprises a depth camera and an RGB camera, and the raw streamed depth and color images are initially not aligned. We use the OpenNI-driver to guarantee pixel-level alignment of depth and color images.

To obtain the absolute camera pose of the RGB-D system, we use an external laser system, GeoSLAM ZEB-REVO (Cadge 2016), which provides 1–3 cm relative mapping-accuracy. To ensure the consistency of mapping results from RGB-D and ZEB-REVO systems, a GeoSLAM ZEB-REVO system is fixed on the platform, as shown in Figure 7a. Careful extrinsic calibration is conducted between the RGB-D sensor and the ZEB-REVO sensor. In our system, the initial transformation between each RGB-D sensor and the ZEB-REVO system is calculated with dozens of markers attached on the wall. An accurate rigid transformation is then derived from their respective ICP progress. Figure 7b shows the sample point-cloud collected by the stereo RGB-D system and ZEB-REVO system.

In our experiments, two data sets are collected to verify the performance of the proposed stereo RGB-D mapping solution. Figure 8 depicts the RGB and depth images taken at various camera poses for various trajectories in the office and hall-space scenes, respectively. All frames are recorded at 640×480 resolution and streamed at a 10 Hz frame rate. Correspondingly, the point cloud and trajectory from the ZEB-REVO system is used for accuracy evaluation, as shown in Figure 9.

Generally, an RGB-D SLAM system generates the camera pose and the corresponding 3D point cloud. While it is necessary to evaluate the quality of the generated point cloud and

camera trajectories for algorithm verification, for each set of data, the results from a single RGB-D sensor and from the stereo RGB-D sensors are both evaluated. Therefore, two kinds of metrics are used to quantify the accuracy of camera-tracking and 3D mapping, as described below.

1. Our trajectory estimation statistics are inspired by previous studies (Handa *et al.* 2014; Sturm *et al.* 2012) that used an absolute trajectory error (ATE) to quantify the accuracy of an entire trajectory. This method involves calculation of the RMSE of the Euclidean distances between the estimated trajectory P_i and the ground truth trajectory obtained from the ZEB-REVO system Q_i . To unify the coordinate frames of both systems, we register the trajectory of the reference RGB-D sensor and the slave sensor to that of the ZEB-REVO system by a rigid-body transformation S^{ref} , S^{slave} calculated with a carefully extrinsic calibration process. Based on this transformation, the absolute error of the trajectory at time stamp i can be calculated by Equation 22, as below:

$$\text{RMSE}(e_i) \cdot \left(\frac{1}{n} \sum_{i=1}^n \text{trans}(e_i)^2 \right)^{\frac{1}{2}} \quad (22)$$

Thus, we evaluate the RMSE over all time indices of the translational components as Equation 23 as below, where $\text{trans}(e_i)$ refers to the translational components of the relative pose-error e_i :

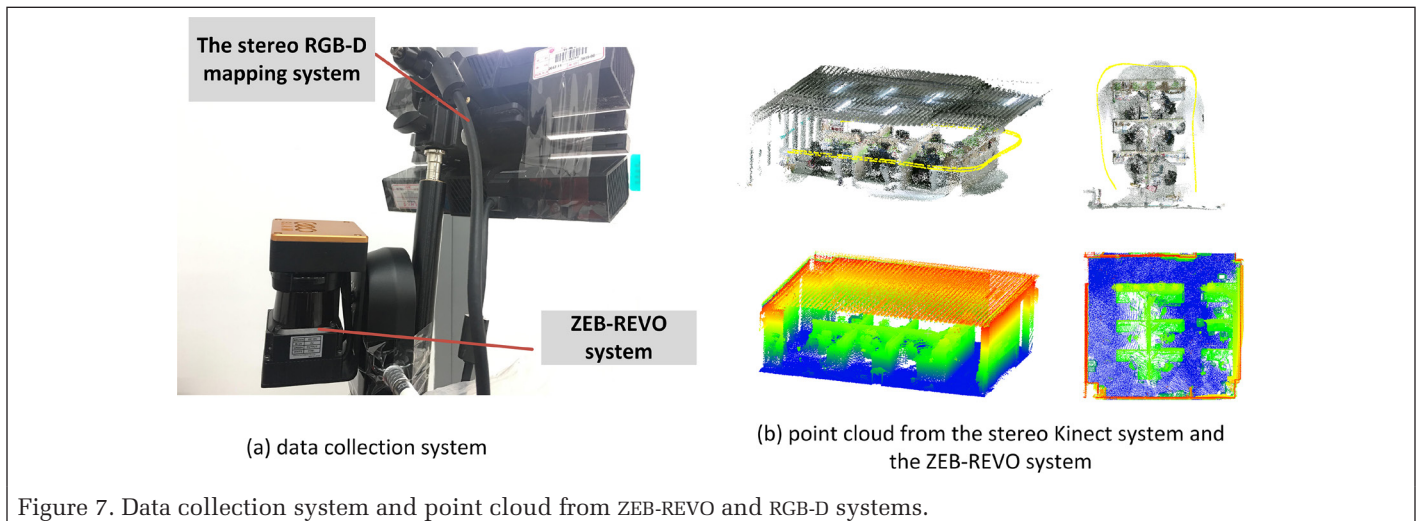


Figure 7. Data collection system and point cloud from ZEB-REVO and RGB-D systems.

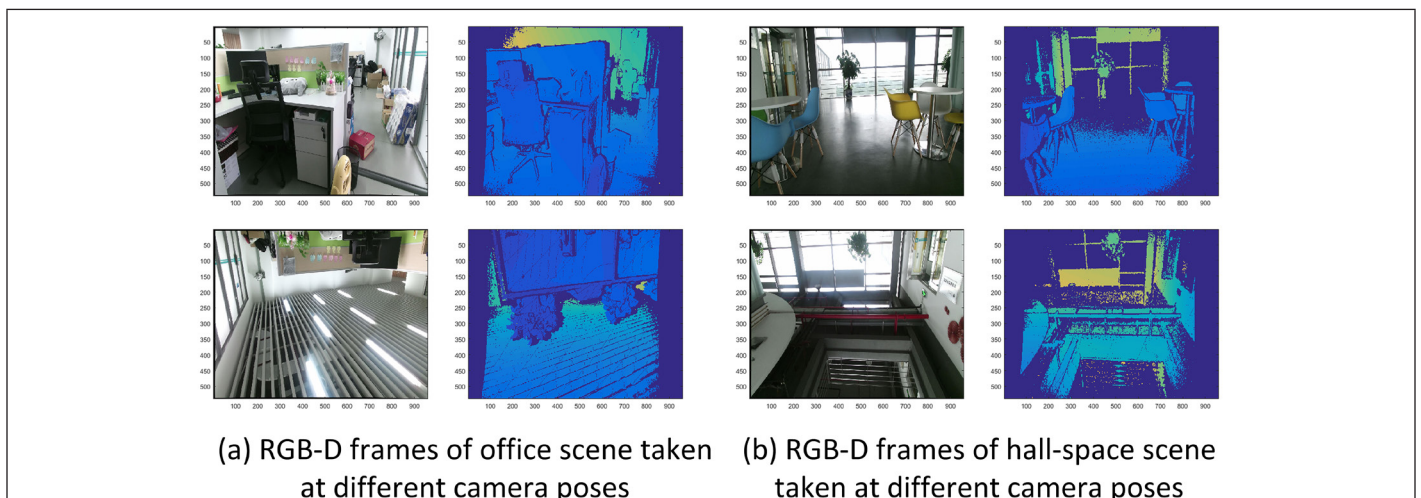


Figure 8. RGB-D frames of two scenes taken at different camera poses.

$$\text{RMSE}(e_i) \cdot \left(\frac{1}{n} \sum_{i=1}^n \text{trans}(e_i)^2 \right)^{\frac{1}{2}} \quad (23)$$

- To quantify the accuracy of 3D reconstruction, the reconstructed point cloud from the RGB-D system is first coarsely aligned with the point cloud from the ZEB-REVO system by manually selecting point correspondences. Point cloud from the RGB-D is then finely aligned to the point cloud from the ZEB-REVO via ICP. Finally, for each point, the closest point in the point cloud from the ZEB-REVO is located, as is the perpendicular distance between the point and the reference point cloud. The standard deviation is computed over the distances for all points.

Experimental Results

Office Scene

The office scene data sets contain two sets of RGB-D sequences recorded from the stereo RGB-D system. The stereo sensor works at 10 Hz with a resolution of 640×480 pixels after rectification. As discussed in the section “Trajectory- Drift- Compensated (Td-C) Approach”, each bundle frame consists of two frames, one from the reference sensor and one from the slave sensor, and a significant time drift was seen in each bundle frame due to the unstable topic-publish rate of the sensors. As shown in Figure 10a, the time drift of each bundle frame in the office scene is plotted together with the camera

trajectory, in which the red dots are the reference sensor’s position after camera-tracking, the yellow dot is the starting point of this scan, and the time drift is represented by the blue error bar. Except for the starting point, the time drift is randomly distributed over the whole trajectory.

Similarly, Figure 10b comprises a plot of the time drift together with the time stamp of the data stream. Quantitatively, the maximum time drift in this scene is approximately 55 ms, and the average drift is about 17.4 ms. Figure 10b shows that the time drift in each bundle frame is generally irregular and unpredictable, which is difficult to model with a unified mathematic model. This will have a large effect on the tracking accuracy of the stereo RGB-D system. Therefore, the time drift in each bundle frame is compensated for by adding an extra transformation to the relationship between the reference sensor and the slave sensor during stereo RGB-D tracking, as detailed in the section “Trajectory- Drift- Compensated (Td-C) Approach”.

In this experiment, the camera trajectory and the point cloud obtained by the ZEB-REVO device are used as the ground truth for accuracy evaluation. Camera tracking experiments were conducted and compared with the data set before and after the Td-C process.

The performance of the proposed Td-C stereo RGB-D mapping method was initially evaluated with the absolute translation RMSE of the camera trajectory. Based on the calibrated external parameters between the RGB-D sensor and the ZEB-REVO system, the estimated camera trajectories are transformed to the coordinate system of the ZEB-REVO system for comparison.

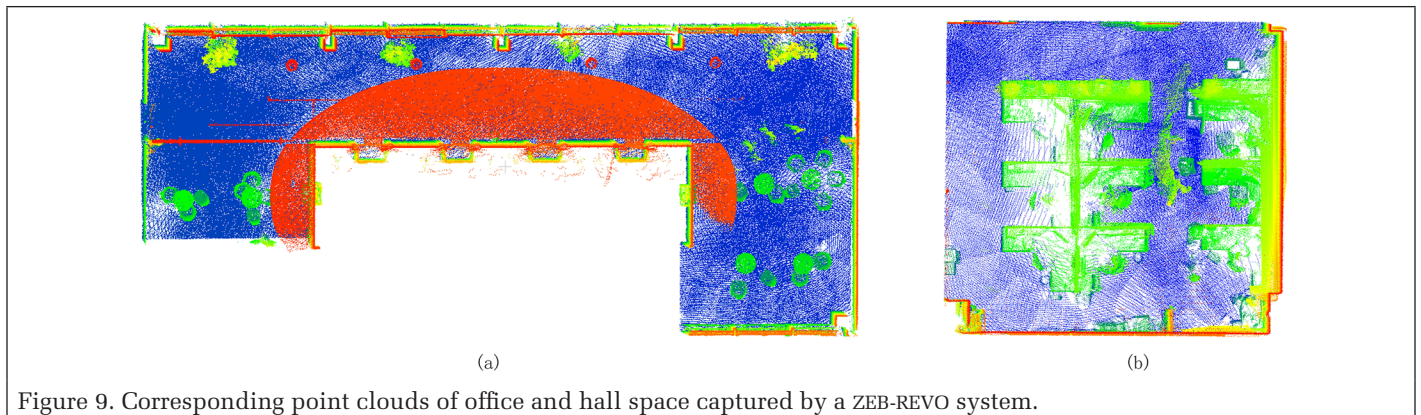


Figure 9. Corresponding point clouds of office and hall space captured by a ZEB-REVO system.

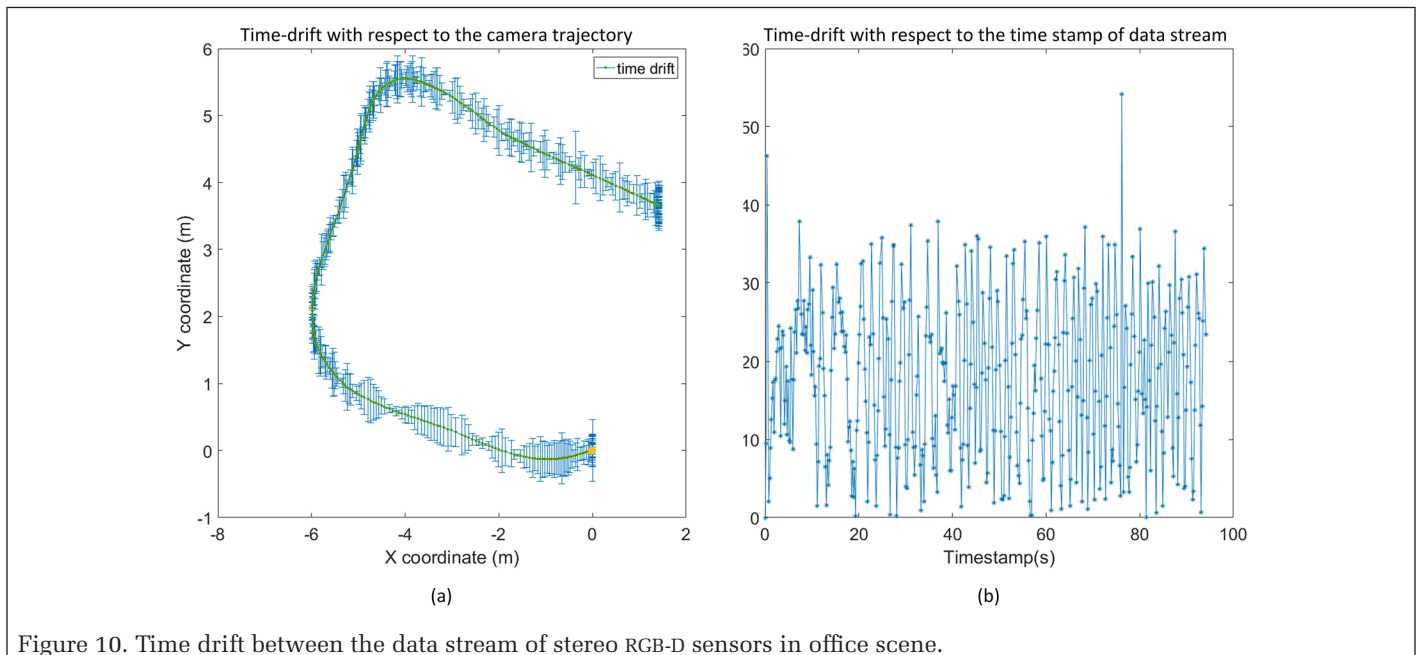


Figure 10. Time drift between the data stream of stereo RGB-D sensors in office scene.

As demonstrated in Figure 11, the estimate trajectories and the ground truth trajectories are plotted and the translation errors of all key bundle frames are represented, together with the trajectories. Table 1 lists all statistics for the accuracy of the reconstruction, including the RMSE in the X, Y, and Z directions, the RMSE of the translation error, and the relative error of the tracking length. As shown in Figure 11, the discrepancies represented by the red lines between the estimated trajectory and the ground truth are improved in the experiment with the data set after the Td-C process than before, perhaps due to more accurate relationships between the reference and the slave sensor.

Table 1 summarizes the RMSE of the translation error for the two conditions. The results after the Td-C process were better, again verifying the performance of the proposed method. The RMSE of the translation error is improved from 0.287 m to 0.335 m, and the relative error is improved from 1.42% to 1.66%. This can be explained by the fact that more reliable visual features can be obtained from the data stream after the Td-C process, which provide a better alignment. The inconsistency between the features from stereo frames before the Td-C process could introduce larger pose drifts, which will accumulate throughout the operation.

The trajectory error explains how the camera-tracking method performs in frame-to-frame tracking but does not imply a better reconstruction is possible. In addition, the absolute mapping error is calculated by comparison with the point cloud generated from the ZED-REVO system. The estimated point cloud from the stereo RGB-D sensor is first registered to the laser system, and ICP is used to refine the alignment. The standard deviation computed over the error for all reconstructed points is used as a metric. Figure 12 shows the estimated point cloud, the heat maps of errors for the 3D reconstructions, and a histogram of the approximate distances of the office scene. The heat maps highlight the least accurate areas of the reconstruction. The range of errors in the heat map of error and the histogram of approximate distances are scaled to a range of 0 to 0.2 m, for comparison purposes. As expected, the odometer without Td-C processing generates worse results and has a large proportion of least accurate areas. In the heat map, a sizable discrepancy can be found in the loop region in the 3D reconstruction result before the Td-C process, which is observed both at the start point and at the end point of this scanning. In the histogram of approximate distances (Figure 13), the accumulated percentage of the points within 5 cm error are calculated and the odometer with Td-C processing

and without Td-C processing achieves 88.539% and 87.897% accuracy respectively, which again verifies the performance of the proposed method. Table 2 lists the average error of the reconstruction before Td-C and after Td-C, and the data show that the average error of the reconstruction improves from 0.018 m to 0.014 m. Therefore, in these scenes, the Td-C strategy improves the tracking accuracy of the stereo system and the 3D reconstruction.

Hall-Space Scene

The stereo RGB-D sequences are recorded in a hall space with a 26.5-m trajectory length. Similarly, the stereo sensor operates at 10 Hz with a resolution after rectification of 640×480 pixels. The distribution of the time drift is shown in Figure 13. As expected, the value of the time drift is mainly distributed between 10 ms and 35 ms. Quantitatively, the maximum time drift in this scene is approximately 60 ms and the average drift is about 22 ms. A Td-C strategy is applied to each bundle frame during camera-tracking.

The performance of the proposed stereo RGB-D mapping approach was initially evaluated with the absolute translation RMSE of the camera trajectory. Figure 14 presents the estimate trajectories, the ground truth trajectories, and the translation errors of all key bundle frames with respect to the trajectories. Table 1 lists the statistics for the accuracy of the reconstruction, including the RMSE in the X, Y, and Z directions, the RMSE of the translation error, and the relative error of the tracking length. As Table 1 shows, the tracking accuracy is better in the experiment after Td-C than in the experiment before Td-C, confirming that the proposed Td-C solution improves the accuracies in all three directions. The RMSE of the translation error improves from 0.397 m to 0.443 m, and the relative error improves from 1.50% to 1.67%.

Figure 15 shows the estimated point cloud, heat maps of errors for 3D reconstructions, and a histogram of approximate distances of the hall-space scene. The error of the 3D

Table 1. Comparison of the ATE for incremental registration of the RGB-D sequences before and after Td-C processing.

Data set	Td-C used?	Length (m)	RMSE.X (m)	RMSE.Y (m)	RMSE.Z (m)	RMSE (m)	Proportion (%)
Office scene	No	20.2	0.213	0.242	0.092	0.335	1.66
	Yes	20.2	0.183	0.211	0.069	0.287	1.42
Hall space scene	No	26.5	0.323	0.277	0.124	0.443	1.67
	Yes	26.5	0.301	0.242	0.092	0.397	1.50

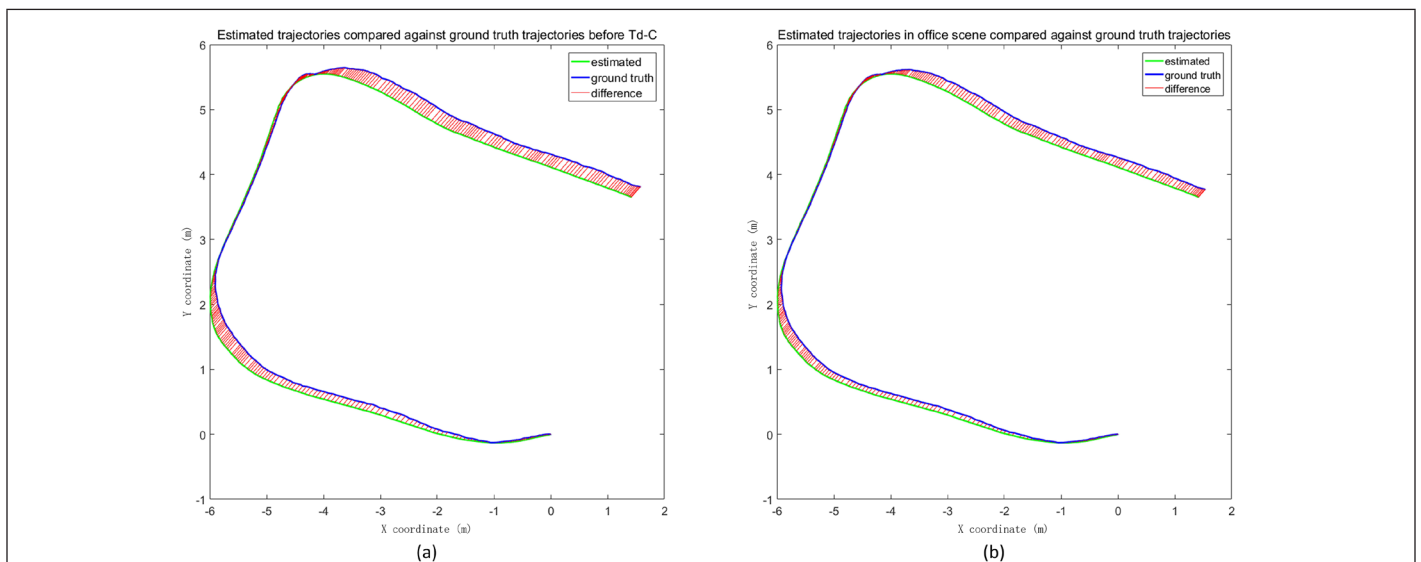


Figure 11. Estimated trajectories from the office scene compared against ground truth trajectories: (a) estimated trajectories before the Td-C strategy; (b) estimated trajectories after the Td-C strategy.

reconstruction is accumulated with the mapping distance, which is consistent with the trend of trajectory error. For comparison purposes, the range of errors in the heatmap of error and the histogram of approximate distances are unified, and the extent is set from 0 to 1.6 m. As expected, the mapping results without Td-C processing generate worse results with a large least-accurate area. In the histogram of approximate distances, the accumulated percentage of points with accuracy greater than 0.2 m is quantified. The odometer achieves 88.992% and 78.045% accuracy with Td-C processing and without Td-C, respectively. According to Table 2, the average error of the reconstruction improves from 0.094 m to 0.057 m, again verifying the performance of the proposed method.

Table 2. Comparison of absolute error for 3D reconstruction before and after Td-C.

Data Set	Td-C used?	Avg. error (m)
Office scene	No	0.018
	Yes	0.014
Hall-space scene	No	0.094
	Yes	0.057

Technical University of Munich Data Sets

As there are no stereo RGB-D data sets available for accuracy comparison, the Technical University of Munich (TUM) public data set, which is collected with a single RGB-D sensor, is used to further demonstrate the performance of our proposed SLAM

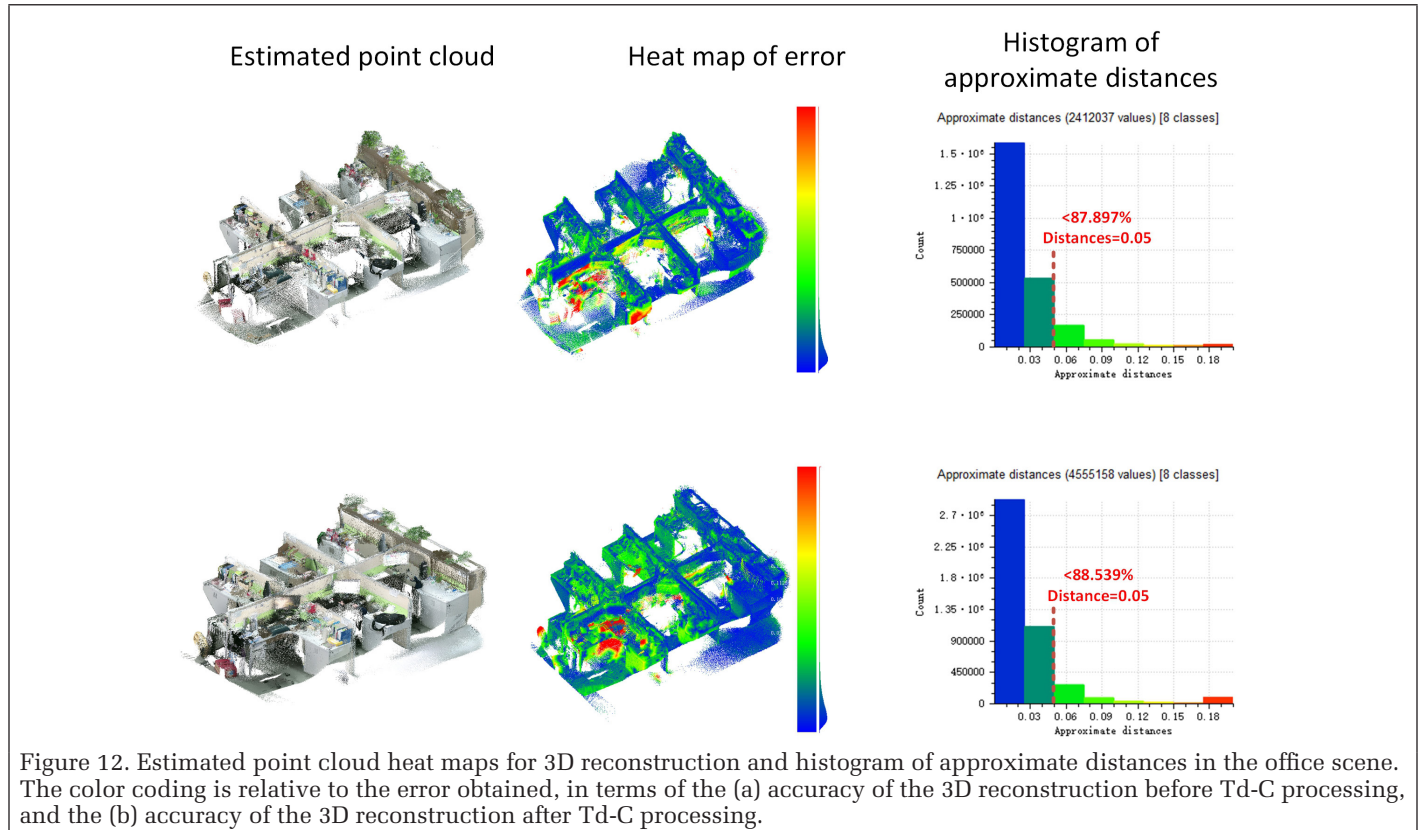


Figure 12. Estimated point cloud heat maps for 3D reconstruction and histogram of approximate distances in the office scene. The color coding is relative to the error obtained, in terms of the (a) accuracy of the 3D reconstruction before Td-C processing, and the (b) accuracy of the 3D reconstruction after Td-C processing.

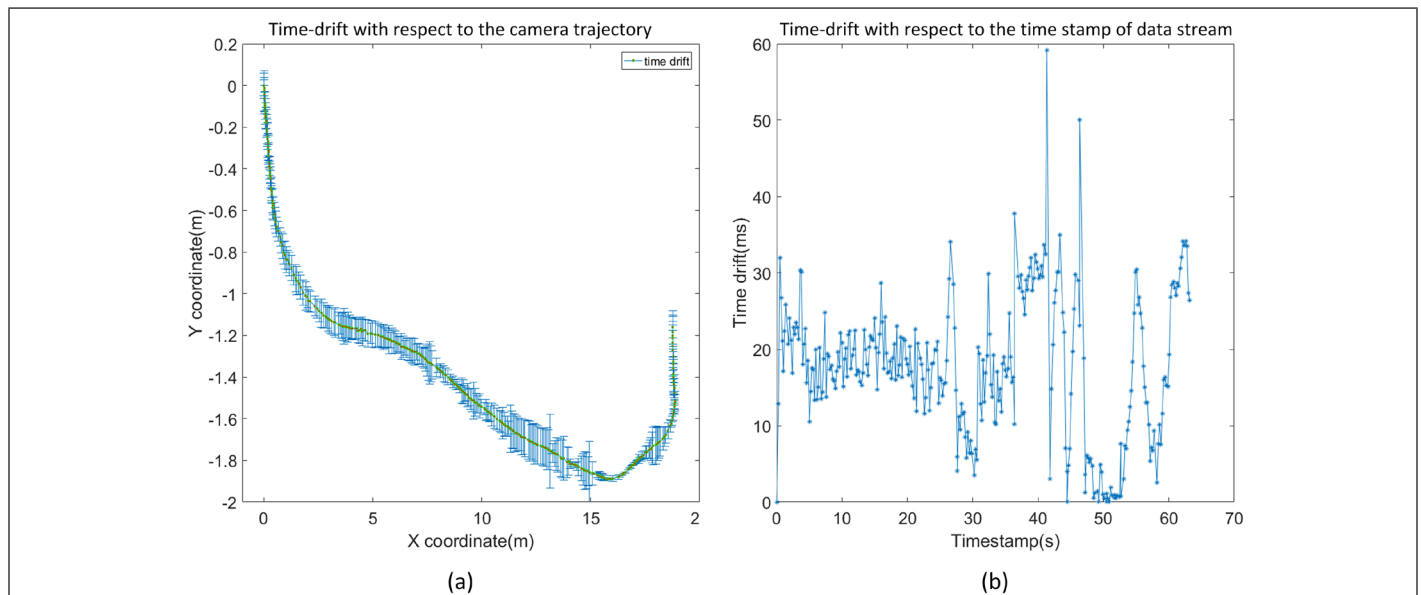


Figure 13. Time drift between data stream of stereo RGB-D sensors in the hall-space scene.

pipeline. We apply our solution on four sequences with different texture, illumination and structure conditions, and compare the experimental results of our system with the following state-of-the-art SLAM methods: Kintinuous (Whelan *et al.* 2012), dense visual odometry (DVO)-SLAM (Kerl *et al.* 2013), and RGB-D SLAM (Endres *et al.* 2014). As shown in Table 3, the proposed RGB-D SLAM system achieves the best performance in two sequences, namely fr1/room, fr2/xyz. In addition, Figure 16 shows the point clouds that result from back-projecting the sensor-depth maps from the computed keyframe poses in four sequences. The good definition and the straight contours of the point clouds prove the highly accurate localization of our approach.

Conclusions and Discussion

In this study, we propose the use of stereo RGB-D cameras in visual SLAM for better pose tracking performance and more

Table 3. Comparisons of the RMSE of ATE, (in m) for incremental registration of RGB-D sequences of the TUM benchmark data set.^a

Sequences	Our SLAM	Kintinuous Fusion	DVO SLAM	RGB-D SLAM
fr1/desk	0.03	0.037	0.021	0.026
fr1/room	0.042	0.075	0.043	0.087
fr2/desk	0.062	0.34	0.017	0.057
fr2/xyz	0.011	0.029	0.018	/

^aThe best results are indicated in bold.

detailed indoor environment mapping. In the stereo RGB-D system, a time drift in each bundle frame is inevitable and changes irregularly, which cannot be mathematically modelled against time drift. We propose a Td-C method to eliminate the influence of time drift during stereo camera motion tracking, which imposes an extra transformation upon the relationships of the reference sensor and the slave sensor in each bundle frame. To enable the use of observations from stereo sensors, a coarse-to-fine stereo RGB-D tracking method is proposed. A detailed mathematical analysis is presented to explain how to fuse the measurements from stereo camera for pose tracking. Via theoretical analysis and experimental validation, we conclude that the proposed Td-C stereo RGB-D mapping solution can eliminate the inconsistency between the data sequence obtained from the stereo sensors and can achieve better pose performance in both camera-tracking and 3D reconstruction.

The Td-C stereo RGB-D mapping method discussed here enables the synchronization of sequences from multiple sensors and the integration of observations from multiple sensors. This permits the full comparative and synergistic use of different data streams from different sensors, even though the system cannot synchronize them precisely. The proposed Td-C strategy can also be used in other similar systems, such as integrated processing of RGB-D sensors and laser systems.

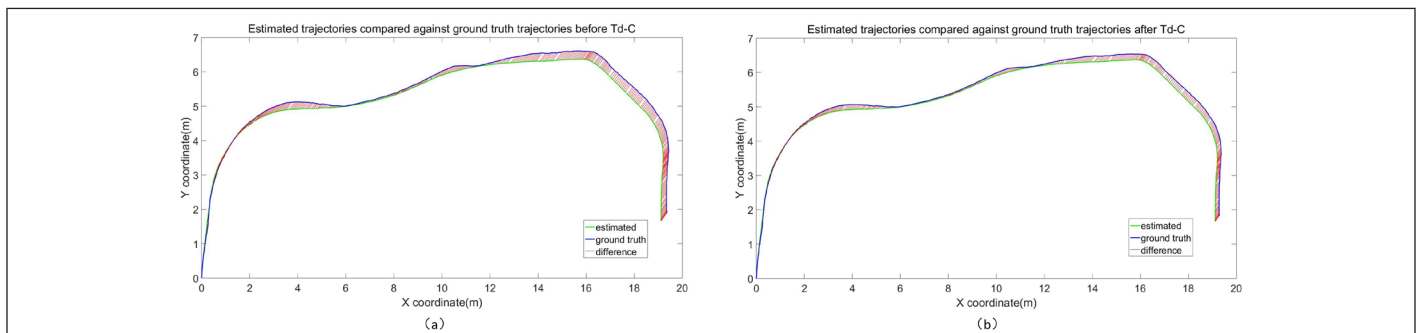


Figure 14. Estimated trajectories from hall-space scene compared against ground truth trajectories: (a) estimated trajectories before Td-C strategy, (b) estimated trajectories after Td-C strategy.

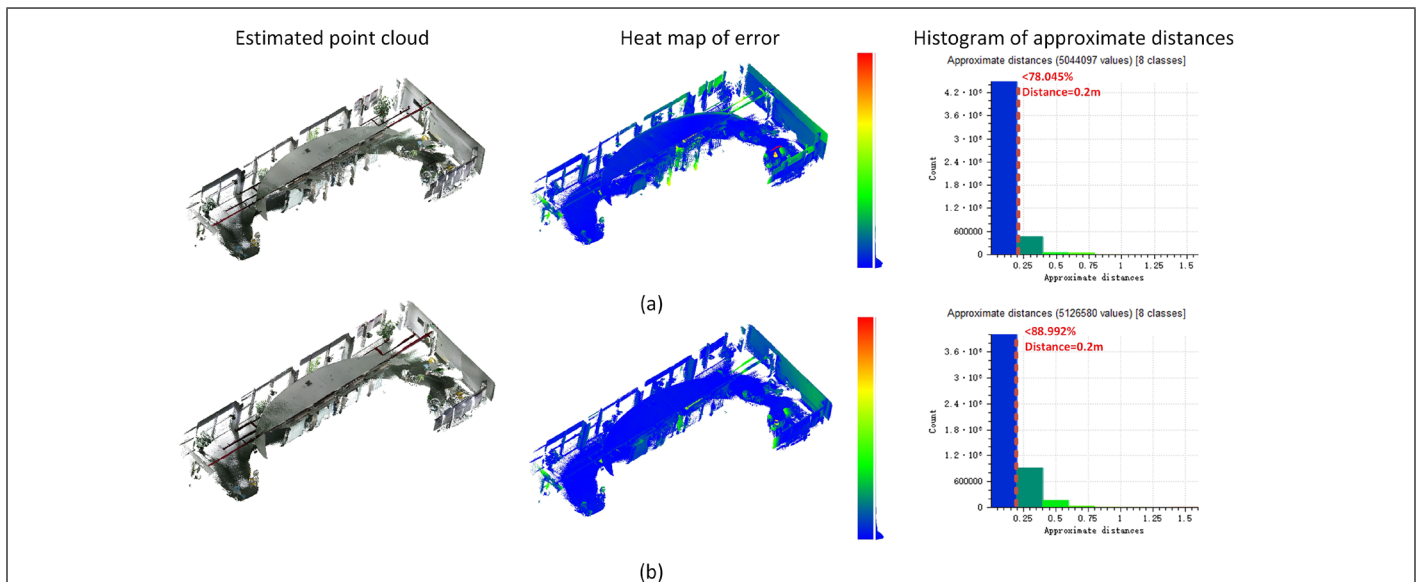


Figure 15. Estimated point cloud, heat maps for 3D reconstructions, and histogram of approximate distances in hall-space scene. The color-coding is relative to the error obtained, where (a) is the accuracy of 3D reconstruction before the Td-C strategy and (b) is the accuracy of 3D reconstruction after the Td-C strategy.

Acknowledgments

This work was supported in part by the National Natural Science Foundation of China under Grant (Projects Nos. 41801392, 41901329, 41971354, and 41971341), and in part by the Research Program of Shenzhen S and T Innovation Committee under Grant (Project Nos. JCYJ20180305125131482).

References

- Alismail, H., B. Browning and S. Lucey. 2016. Photometric bundle adjustment for vision-based SLAM. Pages 324–341 in *Proceedings of the Asian Conference on Computer Vision*.
- Cadge, S. 2016. Welcome to the ZEB REVOLUTION. *GEOmedia* 20 (3).
- Chen, C., B. Yang, S. Song, M. Tian, J. Li, W. Dai and L. Fang. 2018. Calibrate multiple consumer RGB-D cameras for low-cost and efficient 3D indoor mapping. *Remote Sensing* 10 (2):328.
- Chow, J.C.K., D. D. Lichti, J. D. Hol, G. Bellusci and H. Luinge. 2014. IMU and Multiple RGB-D camera fusion for assisting indoor stop-and-go 3D terrestrial laser scanning. *Robotics* 3 (3):247.
- Davison, A. J., Y. G. Cid and N. Kita. 2004. Real-time 3D SLAM with wide-angle vision. *IFAC Proceedings Volumes* 37 (8):868–873.
- Deng, T., J.-C. Bazin, T. Martin, C. Kuster, J. Cai, T. Popa and M. Gross. 2014. Registration of multiple RGBD cameras via local rigid transformations. Pages 1–6 in *Proceedings of the 2014 IEEE International Conference on Multimedia and Expo (ICME)*.
- Dubbelman, G. and B. Browning. 2013. Closed-form online pose-chain SLAM. Pages 5190–5197 in *Proceedings of the 2013 IEEE International Conference on Robotics and Automation*, 6–10 May 2013.
- Endres, F., J. Hess, N. Engelhard, J. Sturm, D. Cremers and W. Burgard. 2012. An evaluation of the RGB-D SLAM system. Pages 1691–1696 in *Proceedings of the 2012 IEEE International Conference on Robotics and Automation (ICRA)*, 14–18 May 2012.
- Endres, F., J. Hess, J. Sturm, D. Cremers and W. Burgard. 2014. 3-D mapping with an RGB-D camera. *IEEE Transactions on Robotics* 30 (1):177–187.
- Engel, J., V. Koltun and D. Cremers. 2017. Direct sparse odometry. *IEEE Transactions on Pattern Analysis and Machine Intelligence* 40 (3):611–625.
- Engelhard, N., F. Endres, J. Hess, J. Sturm and W. Burgard. 2011. Real-time 3D visual SLAM with a hand-held RGB-D camera. Pages 1–15 in *Proceedings of the RGB-D Workshop on 3D Perception in Robotics at the European Robotics Forum*, held in Vasteras, Sweden.
- Fuhrmann, S., F. Langguth and M. Goesele. 2014. MVE-A multi-view reconstruction environment. Pages 11–18 in *Proceedings of the GCH*.
- Gálvez-López, D. and J. D. Tardos. 2012. Bags of binary words for fast place recognition in image sequences. *IEEE Transactions on Robotics* 28 (5):1188–1197.
- Gao, X., R. Wang, N. Demmel and D. Cremers. 2018. LDSO: Direct sparse odometry with loop closure. 2018. Pages 2198–2204 in *Proceedings of the 2018 IEEE/RSJ International Conference on Intelligent Robots and Systems (IROS)*.
- Grisetti, G., R. Kümmerle, H. Strasdat and K. Konolige. 2011. g2o: A general framework for (hyper)graph optimization. Pages 9–13 in *Proceedings of the IEEE International Conference on Robotics and Automation (ICRA)*, held in Shanghai, China.
- Handa, A., T. Whelan, J. McDonald and A. J. Davison. 2014. A benchmark for RGB-D visual odometry, 3D reconstruction and SLAM. Pages 1524–1531 in *Proceedings of the 2014 IEEE International Conference on Robotics and Automation (ICRA)*, 31 May —7 June 2014.
- He, F. and A., Habib. 2018. Three-point-based solution for automated motion parameter estimation of a multi-camera indoor mapping system with planar motion constraint. *ISPRS Journal of Photogrammetry and Remote Sensing* 142:278–291.
- Hee Lee, G., F. Faundorfer and M. Pollefeys. 2013. Motion estimation for self-driving cars with a generalized camera. Pages 2746–2753 in *Proceedings of the IEEE Conference on Computer Vision and Pattern Recognition*.

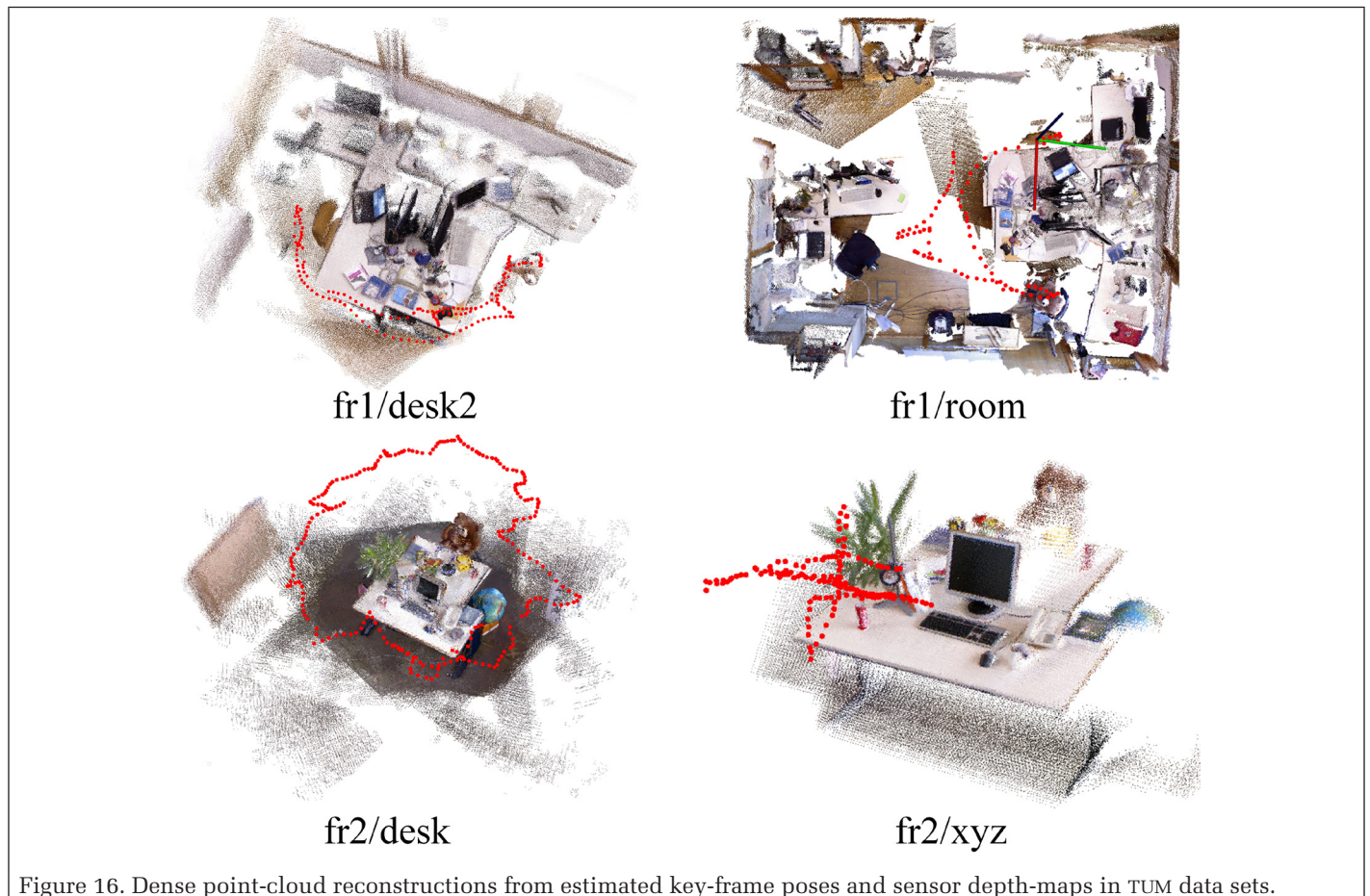


Figure 16. Dense point-cloud reconstructions from estimated key-frame poses and sensor depth-maps in TUM data sets.

- Henry, P., M. Krainin, E. Herbst, X. Ren and D. Fox. 2012. RGB-D mapping: Using Kinect-style depth cameras for dense 3D modeling of indoor environments. *The International Journal of Robotics Research* 31 (5):647–663.
- Henry, P., M. Krainin, E. Herbst, X. Ren and D. Fox. 2014. RGB-D mapping: Using depth cameras for dense 3D modeling of indoor environments. In *Experimental Robotics*, edited by O. Khatib, V. Kumar and G. Sukhatme, 477–491. Heidelberg/Berlin, Germany: Springer.
- Kaess, M. and F. Dellaert. 2006. Visual SLAM with a multi-camera rig. Georgia Institute of Technology. <<http://hdl.handle.net/1853/8726>> Accessed 19 February 2020.
- Kerl, C., J. Sturm and D. Cremers. 2013. Dense visual SLAM for RGB-D cameras. Pages 2100–2106 in *Proceedings of the 2013 IEEE/RSJ International Conference on Intelligent Robots and Systems (IROS)*, 3–7 November 2013.
- Kerl, C., J. Sturm and D. Cremers. 2013. Robust odometry estimation for RGB-D cameras. Pages 3748–3754 in *Proceedings of the 2013 IEEE International Conference on Robotics and Automation (ICRA)*, 6–10 May 2013.
- Kerl, C., J. Stuckler and D. Cremers. 2015. Dense continuous-time tracking and mapping with rolling shutter RGB-D cameras. Pages 2264–2272 in *Proceedings of the IEEE International Conference on Computer Vision*.
- Khoshelham, K. and S. Elberink. 2012. Accuracy and resolution of Kinect depth data for indoor mapping applications. *Sensors* 12 (2):1437–1454.
- Kim, P., B. Coltin and H. Jin Kim. 2018. Linear RGB-D SLAM for planar environments. Pages 333–348 in *Proceedings of the European Conference on Computer Vision (ECCV)*.
- Klein, G. and D. Murray. 2007. Parallel tracking and mapping for small AR workspaces. Pages 1–10 in *Proceedings of the 2007 6th IEEE and ACM International Symposium on Mixed and Augmented Reality*.
- Le, P.-H. and J. Kosecka. 2017. Dense piecewise planar RGB-D SLAM for indoor environments. *arXiv preprint arXiv:1708.00514*.
- Lee, G. H., F. Fraundorfer and M. Pollefeys. 2013. Structureless pose-graph loop-closure with a multi-camera system on a self-driving car. Pages 564–571 in *Proceedings of the 2013 IEEE/RSJ International Conference on Intelligent Robots and Systems*.
- Lowe, D. G. 2004. Distinctive image features from scale-invariant keypoints. *International Journal of Computer Vision* 60 (2):91–110.
- Mazaheri Tehrani, M. 2015. *Constrained Motion Estimation for a Multi-Camera System*. Master's Thesis, University of Calgary, 105 pp.
- Mur-Artal, R. and J. D. Tardos. 2017. ORB-SLAM2: An open-source SLAM system for monocular, stereo, and RGB-D cameras. *IEEE Transactions on Robotics* PP (99):1–8.
- Newcombe, R. A., S. Izadi, O. Hilliges, D. Molyneaux, D. Kim, A. J. Davison, P. Kohi, J. Shotton, S. Hodges and A. Fitzgibbon. 2011. KinectFusion: Real-time dense surface mapping and tracking. Pages 127–136 in *Proceedings of the 2011 10th IEEE International Symposium on Mixed and Augmented Reality (ISMAR)*, 26–29 October 2011.
- Newcombe, R. A., S. J. Lovegrove and A. J. Davison. 2011. DTAM: Dense tracking and mapping in real-time. Pages 2320–2327 in *Proceedings of the 2011 IEEE International Conference on Computer Vision (ICCV)*.
- Nießner, M., M. Zollhöfer, S. Izadi and M. Stamminger. 2013. Real-time 3D reconstruction at scale using voxel hashing. *ACM Transactions on Graphics (TOG)* 32 (6):169.
- Olivier, N., H. Uchiyama, M. Mishima, D. Thomas, R. Taniguchi, R. Roberto, J. P. Lima and V. Teichrieb. 2018. Live structural modeling using RGB-D SLAM. Pages 6352–6358 in *Proceedings of the 2018 IEEE International Conference on Robotics and Automation (ICRA)*, 21–25 May 2018.
- Park, J.-H., Y.-D. Shin, J.-H. Bae and M.-H. Baeg. 2012. Spatial uncertainty model for visual features using a Kinect™ sensor. *Sensors* 12 (7):8640.
- Pless, R. 2003. Using many cameras as one. Page II-587 in *Proceedings of the 2003 IEEE Computer Society Conference on Computer Vision and Pattern Recognition*.
- Schops, T., T. Sattler and M. Pollefeys. 2019. BAD SLAM: Bundle adjusted direct RGB-D SLAM. Pages 134–144 in *Proceedings of the IEEE Conference on Computer Vision and Pattern Recognition*.
- Shi, Y., K. Xu, M. Nießner, S. Rusinkiewicz and T. Funkhouser. 2018. Planematch: Patch coplanarity prediction for robust RGB-D reconstruction. Pages 750–766 in *Proceedings of the European Conference on Computer Vision (ECCV)*.
- Shoemake, K. 1985. Animating rotation with quaternion curves. Pages 245–254 in *Proceedings of the ACM SIGGRAPH Computer Graphics*.
- Sturm, J., N. Engelhard, F. Endres, W. Burgard and D. Cremers. 2012. A benchmark for the evaluation of RGB-D SLAM systems. Pages 573–580 in *Proceedings of the 2012 IEEE/RSJ International Conference on Intelligent Robots and Systems*, 7–12 October 2012.
- Tang, S., W. Chen, W. Wang, X. Li, W. Darwish, W. Li, Z. Huang, H. Hu and R. Guo. 2018. Geometric integration of hybrid correspondences for RGB-D unidirectional tracking. *Sensors* 18 (5):1385.
- Tang, S., Y. Li, Z. Yuan, X. Li, R. Guo, Y. Zhang and W. Wang. 2019. A vertex-to-edge weighted closed-form method for dense RGB-D indoor SLAM. *IEEE Access* 7:32019–32029.
- Vestena, K., D. Dos Santos, E. Oliveira Jr., N. Pavan and K. Khoshelham. 2016. A weighted closed-form solution for RGB-D data registration. *ISPRS-International Archives of the Photogrammetry, Remote Sensing and Spatial Information Sciences*: 403–409.
- Whelan, T., M. Kaess, M. Fallon, H. Johannsson, J. J. Leonard and J. McDonald. 2012. Kintinuous: spatially extended KinectFusion. Pages 1–8 in *RSS Workshop on RGB-D: Advanced Reasoning with Depth Cameras*, held in Sydney, Australia.
- Whelan, T., M. Kaess, H. Johannsson, M. Fallon, J. J. Leonard and J. McDonald. 2015. Real-time large-scale dense RGB-D SLAM with volumetric fusion. *The International Journal of Robotics Research* 34 (4–5):598–626.
- Whelan, T., R. F. Salas-Moreno, B. Glocker, A. J. Davison and S. Leutenegger. 2016. ElasticFusion: Real-time dense SLAM and light source estimation. *The International Journal of Robotics Research* 35 (14):1697–1716.
- Wu, B., X. Ge, L. Xie and W. Chen. 2019. Enhanced 3D mapping with an RGB-D sensor via integration of depth measurements and image sequences. *Photogrammetric Engineering & Remote Sensing* 85 (9):633–642.
- Wu, C. 2007. SiftGPU: A GPU implementation of scale invariant feature transform. *SIFT*. <<http://cs.unc.edu/~ccwu/siftgpu>>.
- Yang, S., S. A. Scherer and A. Zell. 2014. Visual SLAM for autonomous MAVs with dual cameras. Pages 5227–5232 in *Proceedings of the 2014 IEEE International Conference on Robotics and Automation (ICRA)*.
- Yang, S., S. A. Scherer and A. Zell. 2016. Robust onboard visual SLAM for autonomous MAVs. In *Intelligent Autonomous Systems 13*, 361–373. Springer.
- Yang, S., X. Yi, Z. Wang, Y. Wang and X. Yang. 2015. Visual SLAM using multiple RGB-D cameras. Pages 1389–1395 in *Proceedings of the 2015 IEEE International Conference on Robotics and Biomimetics (ROBIO)*.
- Yong, D., C. Lei, W. Yucheng, Y. Min, Q. Xiameng, H. Shaoyang and J. Yunde. 2011. A real-time system for 3D recovery of dynamic scene with multiple RGBD imagers. Pages 1–8 in *Proceedings of the 2011 IEEE Computer Society Conference on Computer Vision and Pattern Recognition Workshops (CVPRW)*.
- Zeng, A., S. Song, M. Nießner, M. Fisher, J. Xiao and T. Funkhouser. 2017. 3DMatch: Learning local geometric descriptors from RGB-D reconstructions. Pages 1802–1811 in *Proceedings of the IEEE Conference on Computer Vision and Pattern Recognition*.
- Zeng, M., F. Zhao, J. Zheng and X. Liu. 2012. A memory-efficient KinectFusion using Octree. In *Computational Visual Media*, edited by S.-M. Hu and R. Martin, 234–241. Berlin/Heidelberg, Germany: Springer.

The Geometric Imaging Model for High-Resolution Optical Remote Sensing Satellites Considering Light Aberration and Atmospheric Refraction Errors

Mi Wang, Ying Zhu, Yanli Wang, and Yufeng Cheng

Abstract

With advances in satellite maneuvering imaging capability, stereoscopic images with large roll and pitch angles can be captured to improve the efficiency of observations. At the same time, the influences of light aberration and atmospheric refraction on image positioning accuracy will be more significant. However, these errors are not accounted for in the traditional imaging and calibration model for optical agile satellites. In this study, the formation mechanisms of the aberration and atmospheric refraction errors in optical remote sensing satellite Earth observation imaging were analyzed quantitatively, and correction models were constructed. From this, the traditional geometric imaging model was refined by introducing a correction model for aberration and atmospheric refraction errors to create a more comprehensive geometric imaging model. The feasibility of an extended rational function model, based on the constructed more comprehensive geometric imaging model, was verified quantitatively.

Introduction

With advances in industrial manufacturing capabilities, increasingly more optical remote sensing satellites are equipped with agile imaging functionality. At present, the traditional geometric imaging model and geometric calibration model are based on an ideal collinear equation; specifically, the image point, the imaging object point, and the projection center satisfy the three-point collinearity principle (Wang *et al.* 2014; Wang *et al.* 2017; Zhang *et al.* 2014). With enhancements in satellite maneuvering imaging, more and more satellites have agile imaging functionality. Agile imaging offers both large-angle and multiangle imaging capabilities. Large-angle imaging can capture images that deviate greatly from the subaerial point (+40–50°). Multiangle imaging captures continuous images of the same sensitive area. However, the influence of environmental factors on imaging light propagation increases with the imaging angle. Compared with traditional three-point collinear imaging, agile imaging is inevitably affected by atmospheric refraction and light aberration (Greslou *et al.* 2008; Greslou *et al.* 2012; Noerdlinger 1999). The light aberration error changes with the imaging angle due to the high-speed relative motion between the satellite platform and the imaging object point. At the same time, the atmospheric refraction error also changes with the imaging angle, as the line of sight

(LOS) passes through the Earth's atmosphere. Because the imaging angles of traditional push-broom satellites are relatively stable, the influence of atmospheric refraction and light aberration can be approximated as systematic errors and compensated for by the installation angle; thus, these errors are usually not taken into account in traditional satellite geometric imaging models or geometric calibration models (Cao, Yuan, and Gong 2015; Chen *et al.* 2015). However, with satellite agile imaging, unsystematic errors for multiscene images and the interior of single-scene images caused by atmospheric refraction and aberration errors increase with geometric resolution and imaging range. With continuous improvement in satellite attitude determination accuracy, the errors of the imaging model gradually become an important component of the positioning errors. Therefore, further improvements in image positioning accuracy of optical remote sensing satellites require that these errors be compensated for with high accuracy modeling.

In traditional imaging and calibration models, light aberration and atmospheric refraction errors are neglected or taken as systematic errors; however, these errors change continuously with the imaging roll and pitch angles (Greslou *et al.* 2008; Greslou *et al.* 2012; Noerdlinger 1999). The geometric calibration of high-resolution linear push-broom satellites usually includes both external and internal calibration systems, involving the determination of the installation angles of the satellite camera and the internal distortion of the satellite camera, respectively. The geometric quality of satellite images should be improved by the combination of camera installation angles and internal distortion parameters (Baltsavias, Li, and Eisenbeiss 2006; De Lussy *et al.* 2012; Delvit *et al.* 2012; Di *et al.* 2014; Fraser and Hanley 2003). Therefore, the traditional calibration model, which doesn't consider light aberration and atmospheric refraction errors, can't also achieve the optimal calibration effect. Based on the comprehensive analysis of previous studies, although the light aberration has been discussed preliminarily in the reference Greslou *et al.* (2012), and the atmospheric refraction has been discussed preliminarily in the reference Yan *et al.* (2015), in a more realistic situation, light aberration and atmospheric refraction errors exist simultaneously. Therefore, the more comprehensive geometric imaging model with light aberration and atmospheric refraction errors compensation capability is necessary for the optical remote sensing satellite. This paper is aimed at building this imaging model and making a more comprehensive analysis.

Mi Wang, Ying Zhu, Yanli Wang, and Yufeng Cheng are with the State Key Laboratory of Information Engineering in Surveying, Mapping and Remote Sensing, Wuhan University, Wuhan 430079, China.

Yufeng Cheng is the correspondence author, and also with China Aerospace Science & Industry Corp 8511 Research Institute, Nanjing 210007, China. (cyf_w hu@126.com)

Photogrammetric Engineering & Remote Sensing
Vol. 86, No. 6, June 2020, pp. 373–382.
0099-1112/20/373–382

© 2020 American Society for Photogrammetry
and Remote Sensing
doi: 10.14358/PERS.86.6.373

In this study, we developed a more comprehensive geometric imaging model to account for light aberration and atmospheric refraction errors. Starting from the formation mechanism of light aberration and atmospheric refraction error, the error models of light aberration and atmospheric refraction were built and modified. The effects of light aberration and atmospheric refraction errors on absolute geometric positioning accuracy and relative geometric positioning accuracy of satellite images were qualitatively and quantitatively analyzed. On this basis, a more comprehensive geometric imaging model considering atmospheric refraction and light aberration error correction was constructed, and the fitting accuracy of the general rational function model (RFM) is analyzed, which further expands the application scope of the proposed model.

The More Comprehensive Geometric Imaging Model

Traditional Geometric Imaging Model

The linear-array push-broom imaging mode is a common imaging method for high-resolution optical remote sensing satellites. The traditional geometric imaging model defaults such that each scanning line satisfies the collinear equation of the central projection; i.e., the image points, the corresponding ground object points, and the camera photographic center satisfy the collinear relationship. Therefore, the traditional geometric imaging and calibration model can be described as follows:

$$\begin{bmatrix} \tan \varphi_x \\ \tan \varphi_y \\ 1 \end{bmatrix} = \lambda R_{\text{body}}^{\text{camera}} R_{\text{J2000}}^{\text{body}} R_{\text{WGS84}}^{\text{J2000}} \begin{bmatrix} X \\ Y \\ Z \end{bmatrix}_{\text{WGS84}} - \begin{bmatrix} X_s \\ Y_s \\ Z_s \end{bmatrix}_{\text{WGS84}} \quad (1)$$

$$\begin{cases} \tan \varphi_x = a_0 + a_1 s + \dots + a_n s^m \\ \tan \varphi_y = b_0 + b_1 s + \dots + b_n s^m \end{cases} \quad (2)$$

where φ_x and φ_y represent the directional angles along and across the charge-coupled device (CCD) (Wang *et al.* 2014; Zhang *et al.* 2014), respectively; s represents the identification number of each CCD detector; a_0, a_1, \dots, a_m and b_0, b_1, \dots, b_m represent the internal calibration parameters of each single CCD; m represents the orders of the polynomial model; $[X \ Y \ Z]_{\text{WGS84}}^T$ represents the object space coordinates of the corresponding image point (s, l) in the WGS84 coordinate system; $[X_s \ Y_s \ Z_s]_{\text{WGS84}}^T$ represents the object space coordinates of the projection center in the WGS84 coordinate system, and can be interpolated from the orbit measurements by observation time; $R_{\text{body}}^{\text{camera}}$ (camera_α, camera_β, camera_γ) represents the installation matrix from the satellite body coordinate system to the camera coordinate system, camera_α, camera_β, camera_γ represent the installation angles; $R_{\text{J2000}}^{\text{body}}$ represents the attitude matrix from the J2000 coordinate system to the satellite body coordinate system, and can be interpolated from the attitude measurements by observation time; and $R_{\text{WGS84}}^{\text{J2000}}$ represents the transformation matrix from the WGS84 coordinate system to the J2000 coordinate system. In the traditional calibration process, the installation matrix $R_{\text{body}}^{\text{camera}}$ (camera_α, camera_β, camera_γ) and the internal parameters $\tan \varphi_x(a_0, a_1, \dots, a_m)$ and $\tan \varphi_y(a_0, a_1, \dots, a_m)$ are the calibration parameters.

Light aberration and atmospheric refraction are not taken into consideration in the traditional geometric imaging model or calibration process (Gruen, Kocaman, and Wolff 2007; Jiang *et al.* 2014; Poli and Toutin 2012). These errors are neglected, i.e., treated as systematic errors and are compensated

for by the installation angles. In fact, these errors are actually unsystematic when the imaging angles change. Compensating for these errors using the installation angles can only guarantee the accuracy of the calibration image, and for the other test images, the calibrated parameters most likely introduce new systematic error. To build a more comprehensive geometric imaging model, light aberration and atmospheric refraction errors should be taken into consideration as dynamic entities.

Light Aberration Error

In the optical remote sensing satellite imaging system, the satellite has high-speed motion relative to the ground, so that the direction of light observed by the satellite also deviates from the actual direction of light (Greslou *et al.* 2008; Greslou *et al.* 2012). In Figure 1a, δ represents the angle between the real direction of the light (\vec{w}) and the observed direction of the light (\vec{u}). δ is caused by the speed of relative movement (\vec{V}) between the satellite and the observed object. In Figure 1b, we define the pitch angle of the observed light relative to the orbital coordinate system as pitch = ψ_y and the roll angle of the observed light relative to the orbital coordinate system as roll = ψ_x . The speed component of the observed light in the orbital coordinate system can be represented as follows:

$$\vec{u} = c \begin{bmatrix} \tan(\psi_y) \\ \tan(\psi_x) \\ 1 \end{bmatrix} = \frac{c}{\sqrt{1 + \tan^2(\psi_x) + \tan^2(\psi_y)}} \begin{bmatrix} \tan(\psi_y) \\ \tan(\psi_x) \\ 1 \end{bmatrix} \quad (3)$$

Because $\|\vec{V}(P)\| \ll c$, and to compensate for light aberration to obtain the real direction of the observed light, we can use the traditional Galilean transformation to recalculate the speed component of the observed light in the orbital coordinate system. The real direction of the light (\vec{w}) is described in the orbital coordinate system, as follows:

$$\vec{w} = \vec{u} + \vec{V}(P) = c \begin{bmatrix} \tan(\psi_y) \\ \tan(\psi_x) \\ 1 \end{bmatrix} + \begin{bmatrix} V_x \\ V_y \\ 0 \end{bmatrix} \quad (4)$$

$\vec{V}(P)$ is given by

$$\vec{V}(P) = \begin{bmatrix} V_x \\ V_y \\ V_z \end{bmatrix} \approx \begin{bmatrix} V_{\text{sat}} - V_{\text{earth}} \cos(i) \\ -V_{\text{earth}} \sin(i) \\ 0 \end{bmatrix} = \begin{bmatrix} (R+H)w_{\text{sat}} - R w_{\text{earth}} \cos(\beta) \cos(i) \\ -R w_{\text{earth}} \cos(\beta) \sin(i) \\ 0 \end{bmatrix} \quad (5)$$

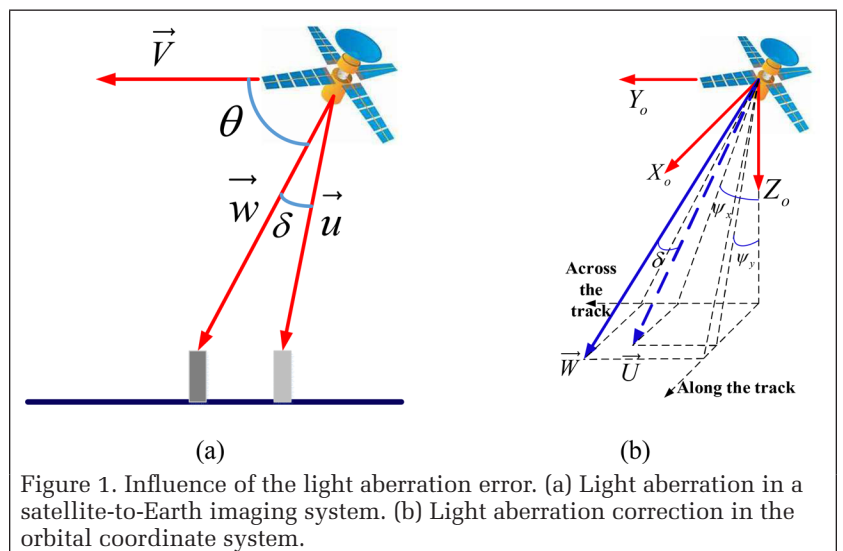


Figure 1. Influence of the light aberration error. (a) Light aberration in a satellite-to-Earth imaging system. (b) Light aberration correction in the orbital coordinate system.

where V_{sat} represents the velocity of the satellite, V_{earth} represents the Earth's rotation velocity at the equator, i represents the inclination of the orbit, R represents the Earth's radius, H represents the orbit altitude, β represents the angle between the equatorial plane and the vector from the center of the Earth to the satellite, ω_{earth} represents the angular speed of the Earth's rotation, and ω_{sat} represents the angular speed of the satellite around the Earth.

Because ψ_y and ψ_x are the pitch and roll angles, respectively, of the observed light relative to the orbital coordinate system, they can be obtained by the LOS of the camera coordinate system, based on the following:

$$\begin{bmatrix} \tan(\psi_y) \\ \tan(\psi_x) \\ 1 \end{bmatrix} = \lambda R_{\text{body}}^{\text{orbit}} R_{\text{camera}}^{\text{orbit}} (\text{camera_}\alpha, \text{camera_}\beta, \text{camera_}\gamma) \begin{bmatrix} \tan(\varphi_y) \\ \tan(\varphi_x) \\ 1 \end{bmatrix} \quad (6)$$

where λ is a scale factor, $R_{\text{body}}^{\text{camera}}$ (camera_ α , camera_ β , camera_ γ) represents the installation matrix from the camera coordinate system to the satellite body coordinate system and $R_{\text{body}}^{\text{orbit}}$ represents the transformation matrix from the satellite body coordinate system to the orbital coordinate system.

Atmospheric Refraction Error

The optical remote sensing satellite obtains images of the Earth by receiving sunlight reflected from ground objects. When the reflected sunlight from ground objects passes through the stratified atmosphere and enters the satellite's camera in a vacuum environment, the path of the reflected sunlight is bent. As such, the image point in the image space, the ground point in the object space, and the projection center are not in the same LOS (Yan *et al.* 2015); therefore, the traditional geometric imaging model is not rigorous.

In Figure 2a, α is the view angle offset from the subastral point (side view angle), and it can be calculated in terms of the pitch angle ψ_y and the roll angle ψ_x :

$$\tan \alpha = \sqrt{\tan^2 \psi_x + \tan^2 \psi_y} \quad (7)$$

In Figure 2b, we can take the atmosphere as uniform to simplify the analysis. If we assume that the image point (p) emits a beam of light to the object point (Q), the view angle offset the subastral point is α . Q_0 is the intersection of the

emitted light and the top of the atmosphere. With atmospheric refraction, Q_1 is the intersection of the refracted light and the ground. The distance between Q and Q_1 is the positioning deviation caused by atmospheric refraction. χ is the real view angle offset of the subastral point, which is determined by Q_1 and the projection center (s). H is the orbital altitude of the satellite, R is the average radius of the Earth, h is the thickness of the atmosphere, n is the refractive index, and f is the focal length of the camera. β is the incidence angle of the emitted light from p and the top of the atmosphere, as follows:

$$\beta = \arcsin\left(\frac{R+H}{R+h} \sin \alpha\right) \quad (8)$$

A vacuum environment exists outside of the atmosphere, with a refractive index of $n = 1$. Based on the law of refraction, the refraction angle γ of the emitted light is as follows:

$$\gamma = \arcsin\left(\frac{\sin \beta}{n}\right) \quad (9)$$

When there is no atmospheric refraction effect, φ is the incidence angle of the emitted light from p , and the Earth ellipsoid, $\theta = \angle QOS$, $\theta_0 = \angle Q_0OS$, $\theta_1 = \angle Q_1OQ_0$, then

$$\theta = \varphi - \alpha \quad (10)$$

$$\theta_0 = \varphi - \alpha \quad (11)$$

$$\theta_1 = \arcsin\left[\frac{(R+h)\sin \gamma}{R}\right] - \gamma \quad (12)$$

The geocentric angle error $\Delta\theta$ caused by the single atmosphere can be calculated as $\Delta\theta = \theta - \theta_0 - \theta_1$. When the atmosphere is divided into multilayered atmospheres, the geocentric angle error can be calculated as $\Delta\theta = \theta - \theta_0 - \theta_1 - \dots - \theta_i$ and i is the number of layers. We define $\delta\theta = \theta_0 + \theta_1 + \dots + \theta_i$. Then

$$\frac{\sin \chi}{R} = \frac{\sin(\delta\theta + \chi)}{R+H} \quad (13)$$

$$\chi = \arctan\left(\frac{R \sin(\delta\theta)}{R+H - R \cos(\delta\theta)}\right) \quad (14)$$

To compensate for the atmospheric refraction error, χ is the updated view angle offset from the subastral point. In most cases, such as $\alpha < 50^\circ$, $\alpha \approx \sqrt{\psi_x^2 + \psi_y^2}$. Then in the orbital coordinate system, the updated pitch and roll angles can be represented as follows:

$$\begin{aligned} \psi_y^r &= FUN_n(\psi_y) = \frac{\psi_y}{\alpha} \cdot \chi \\ \psi_x^r &= FUN_n(\psi_x) = \frac{\psi_x}{\alpha} \cdot \chi \end{aligned} \quad (15)$$

More Comprehensive Geometric Imaging Model

From the previous analysis, we can rebuild the relationship of the image points, the corresponding ground object points, and the camera photographic center, which considers the light aberration and atmospheric refraction, as follows:

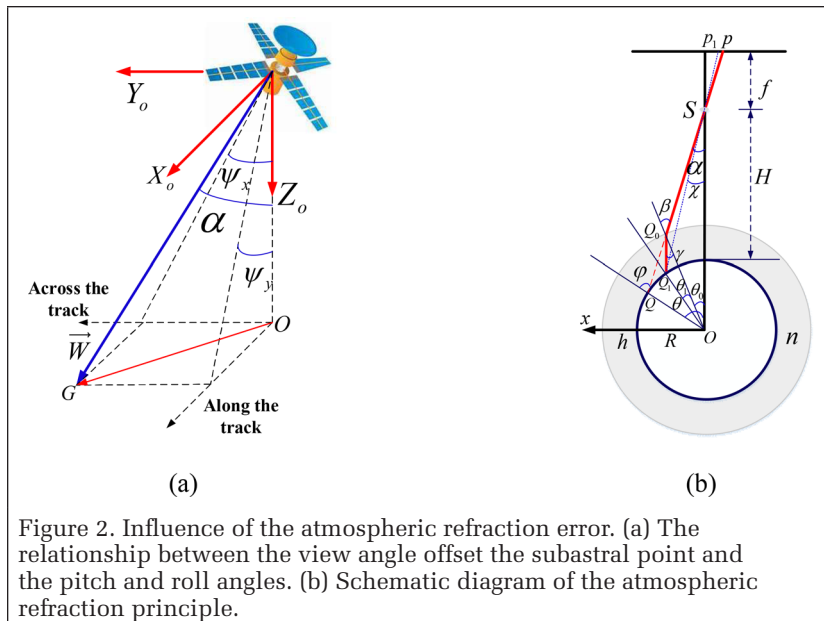


Figure 2. Influence of the atmospheric refraction error. (a) The relationship between the view angle offset the subastral point and the pitch and roll angles. (b) Schematic diagram of the atmospheric refraction principle.

$$\lambda R_{\text{body}}^{\text{orbit}} R_{\text{body}}^{\text{body}} R_{\text{WGS84}}^{\text{J2000}} \begin{pmatrix} [X] \\ [Y] \\ [Z] \end{pmatrix}_{\text{WGS84}} - \begin{pmatrix} [X_s] \\ [Y_s] \\ [Z_s] \end{pmatrix}_{\text{WGS84}} = \begin{pmatrix} V_{\text{xorbit_aberration_refraction}} \\ V_{\text{yorbit_aberration_refraction}} \\ V_{\text{zorbit_aberration_refraction}} \end{pmatrix} \quad (16)$$

where

$$\begin{pmatrix} V_{\text{xorbit_aberration_refraction}} \\ V_{\text{yorbit_aberration_refraction}} \\ V_{\text{zorbit_aberration_refraction}} \end{pmatrix} = \begin{pmatrix} \tan(FUN_n(\arctan(V_{\text{xorbit_aberration}}/V_{\text{zorbit_aberration}}))) \\ \tan(FUN_n(\arctan(V_{\text{yorbit_aberration}}/V_{\text{zorbit_aberration}}))) \\ 1 \end{pmatrix} \quad (17)$$

$$\begin{pmatrix} V_{\text{xorbit_aberration}} \\ V_{\text{yorbit_aberration}} \\ V_{\text{zorbit_aberration}} \end{pmatrix} = \left\| \left\| R_{\text{body}}^{\text{orbit}} R_{\text{camera}}^{\text{body}} \begin{pmatrix} \tan \varphi_x \\ \tan \varphi_y \\ 1 \end{pmatrix} + \begin{pmatrix} V_x \\ V_y \\ 0 \end{pmatrix} \right\| \right\| \quad (18)$$

First, we use Equation 18 to compensate for the light aberration error. Equation 18 can be obtained by combining Equation 4 and Equation 6. $[\tan \varphi_x \ \tan \varphi_y \ 1]^T$ in Equation 18 is the observed LOS in the camera coordinate system, and it is the original measurement input parameter. $\| \|$ is the operation of calculating unit vector. $[V_{\text{xorbit_aberration}} \ V_{\text{yorbit_aberration}} \ V_{\text{zorbit_aberration}}]^T$ in Equation 18 is the observed LOS in the orbit coordinate system after light aberration error correction, and it is the input parameter of Equation 17. Second, we use Equation 17 to compensate for the atmospheric refraction error. Equation 17 can be obtained from Equation 15. $[V_{\text{xorbit_aberration_refraction}} \ V_{\text{yorbit_aberration_refraction}} \ V_{\text{zorbit_aberration_refraction}}]^T$ in Equation 17 is the observed LOS in the orbit coordinate system after light aberration error correction and atmospheric refraction error correction, and it is the input parameter of Equation 16. Thus, in this form, the orbital coordinate system is the reference coordinate system.

In some cases, the light aberration error can be taken as a systematic error for individual pixels of one image. Under these conditions, Equation 18 can be simplified as follows:

$$\begin{pmatrix} V_{\text{xorbit_aberration}} \\ V_{\text{yorbit_aberration}} \\ V_{\text{zorbit_aberration}} \end{pmatrix} = \left\| \left\| R_{\text{aberration}} R_{\text{body}}^{\text{orbit}} R_{\text{camera}}^{\text{body}} \begin{pmatrix} \tan \varphi_x \\ \tan \varphi_y \\ 1 \end{pmatrix} \right\| \right\| \quad (19)$$

where $R_{\text{aberration}}$ represents the correction matrix of the light aberration error.

Under the same circumstances for the atmospheric refraction error, Equation 17 can be simplified as follows:

$$\begin{pmatrix} V_{\text{xorbit_aberration_refraction}} \\ V_{\text{yorbit_aberration_refraction}} \\ V_{\text{zorbit_aberration_refraction}} \end{pmatrix} = R_{\text{refraction}} \begin{pmatrix} V_{\text{xorbit_aberration}} \\ V_{\text{yorbit_aberration}} \\ V_{\text{zorbit_aberration}} \end{pmatrix} \quad (20)$$

where $R_{\text{refraction}}$ represents the correction matrix of the atmospheric refraction error.

Equation 16 is then given by

$$\lambda R_{\text{body}}^{\text{orbit}} R_{\text{body}}^{\text{body}} R_{\text{WGS84}}^{\text{J2000}} \begin{pmatrix} [X] \\ [Y] \\ [Z] \end{pmatrix}_{\text{WGS84}} - \begin{pmatrix} [X_s] \\ [Y_s] \\ [Z_s] \end{pmatrix}_{\text{WGS84}} = R_{\text{refraction}} R_{\text{aberration}} R_{\text{body}}^{\text{orbit}} R_{\text{camera}}^{\text{body}} \begin{pmatrix} \tan \varphi_x \\ \tan \varphi_y \\ 1 \end{pmatrix} \quad (21)$$

Because $R_{\text{refraction}}$ and $R_{\text{aberration}}$ are totally correlated with $R_{\text{camera}}^{\text{body}}$, they can be compensated for by the installation angles based on the traditional calibration model and method. Therefore, Equation 21 has no essential differences with respect to the traditional geometric imaging model, as described by Equation 1, when treating the light aberration and

atmospheric refraction errors as systematic errors for each pixel of one image.

In fact, the light aberration and the atmospheric refraction occur simultaneously, and there is no absolute sequence. Because the LOS errors caused by the light aberration and the atmospheric refraction are small, the LOS errors have limited impact on the pitch and roll angles (side view angle). Then the pitch and roll angles with small error caused by the light aberration will have small impact on the estimation of the atmospheric refraction error. Similarly, the pitch and roll angles with small error caused by the atmospheric refraction will have small impact on the estimation of the light aberration error. Therefore, either correcting the light aberration error first or correcting the atmospheric refraction error first will be reasonable.

Experiments and Discussion

Absolute Positioning Accuracy Analysis of the Light Aberration and Atmospheric Refraction Error

Light Aberration Error

According to the above analysis, the influence of the light aberration on the accuracy of satellite absolute geometric positioning depends mainly on the relative velocity between the satellite and the observation point, and the angle between the relative velocity direction and the LOS vector. However, the satellite flight speed depends on the orbital altitude; the rotation speed of the observation points depends on the latitude; and the angle between the relative velocity direction and the LOS vector depends on the pitch and roll angles of the LOS vector in the satellite orbital coordinate system. Here, we examine the influence of the light aberration on the absolute positioning accuracy from three aspects: the satellite orbital altitude, the latitude of the observation point, and the pitch and roll angles.

Orbital altitude: Table 1 shows the effect of different orbital altitudes on the light aberration deviation angle and positioning error.

Table 1. Effect of different orbital altitudes on light aberration and positioning error.

Orbital altitude (km)	Flight Speed (km/s)	Deviation Angle (arcsec)	Positioning Error (m)
250	7.75	5.34	6.47
350	7.69	5.30	8.99
450	7.63	5.26	11.48
550	7.58	5.22	13.93
650	7.53	5.19	16.35

Both satellite flight velocity and earth rotation velocity will affect the light aberration error at the same time based on Equation 5. When we analyze the effect of different satellite flight velocities on the light aberration error in Table 1, we fix the observation point (equatorial position), then the earth rotation velocity is invariant (465 m/s). From Table 1, the satellite's flight speed decreases as altitude increases. Thus, the corresponding light aberration deviation angle of subsatellite points decreases; however, the geometric positioning error increases with imaging distance.

Latitude of the observation point: With an increase in the latitude of observation points, the rotational linear velocity of the Earth decreases gradually, which makes the relative velocity of the satellite and the observation points change, thus causing variations in the light aberration.

When we analyze the effect of different earth rotation velocity on the light aberration error in Table 2, we fix the orbital altitude of 650 km, then the satellite flight velocity is invariant (7530 m/s). Given an orbital altitude of 650 km, an increase in the observation latitude reduced the ground velocity. This, in turn, lowered the relative velocity of the satellite with respect to the observed ground object point, leading to a reduction in the light aberration deviation angle (Table 2). Notably, this phenomenon is symmetrical for the Southern and Northern Hemispheres.

Table 2. Influence of different observation latitudes on light aberration (for an orbital altitude of 650 km).

Latitude	Ground Velocity (m/s)	Deviation Angle (arcsec)
90°	0	5.178
60°	233	5.180
30°	403	5.185
0°	465	5.188
-30°	403	5.185
-60°	233	5.180
-90°	0	5.178

Pitch and roll angles: To analyze the variation law of light aberration under different pitch and roll angles, we considered a polar orbit satellite with an orbital altitude of 650 km. When the satellite is over the equator, the variation in the light aberration under different pitch and roll angles in the orbital coordinate system can be calculated.

The relative velocity of the satellite can be expressed as

$$\vec{V}(P) = \begin{bmatrix} V_x \\ V_y \\ 0 \end{bmatrix} \approx \begin{bmatrix} 7530 \\ -465 \\ 0 \end{bmatrix} \text{ m/s} \quad (22)$$

Figure 3a shows the variation in the light aberration deviation angle of the satellite over the equator with different pitch and roll angles. The variation with respect to the roll angle was small, whereas that with the pitch angle was more significant. The distribution of the geometric positioning error caused by light aberration with changes in the roll and pitch angles is shown in Figure 3b. Because the imaging distance between the satellite and the ground point changes significantly under different conditions of roll and pitch, the variation law of geometric positioning error differed significantly from that of the light aberration deviation angle. The geometric positioning error increased gradually with the absolute values of the roll and pitch angles.

Atmospheric Refraction Error

According to the analysis in the first section called “Light Aberration Error”, the deviation of the LOS in the orbital coordinate system caused by the atmospheric refraction error is related to the atmospheric refraction coefficient, the ground

elevation value, the orbital altitude, and the pitch and roll angles of the LOS in the orbital coordinate system, as discussed below.

Atmospheric refraction coefficient: Optical remote sensing satellites obtain panchromatic images over the spectral range of 0.45–0.8 μm. For multispectral images, the spectral range of the blue band is 0.45–0.52 μm (central wavelength: 0.485 μm), the green band is 0.53–0.60 μm (central wavelength: 0.565 μm), the red band is 0.63–0.69 μm (central wavelength: 0.66 μm), and the near-infrared band is 0.76–0.90 μm (central wavelength: 0.83 μm). When monochromatic light passes through the atmosphere, shorter wavelengths result in larger calculated atmospheric refractive indexes. Different refractive indices cause different positioning errors. We divided the atmosphere into 26 layers based on data from the National Centers for Environmental Prediction (NCEP) Final (FNL) Operational Model Global Tropospheric Analyses, continuing from July 1999 (<https://doi.org/10.5065/D6M043C6>) (Owens *et al.* 1967; Stone *et al.* 1996; Thomas, Herring, and Quinn 2012). In the reference (Yan *et al.* 2015), the atmospheric refraction error has not been combined with the imaging model. We did this work and made more rigorous quantitative analysis by dividing the atmosphere into 26 layers. The refractive index of different bands was calculated based on the atmospheric parameters at 6:00 A.M. on 1 June 2016. Assuming an orbital altitude of 630 km and a side view angle of 30°, the positioning error caused by atmospheric refraction of four central wavelengths of different bands at each latitude and longitude (unit: degree) are shown in Figure 4.

From Figure 4, shorter wavelengths were associated with greater atmospheric refraction positioning error under the same conditions. With respect to the central wavelength, this deviation was on the order of a centimeter.

To analyze the influence of different atmospheric conditions on atmospheric refraction offset at different periods, the atmospheric parameters at 6:00 A.M. on 1 December 2016, were acquired by the NCEP, from which the atmospheric refraction positioning errors at different latitudes and longitudes were calculated. A blue central wavelength was assumed, and the orbital altitude and side view angle were held constant. The results are shown in Figure 5.

Based on Figure 5, the influence of different atmospheric conditions on the calculation of the refractive index of the same band and the corresponding positioning error was limited (<0.1 m). Thus, atmospheric condition does not play a key role in the positioning error caused by atmospheric refraction.

Ground elevation value: To analyze the influence of the ground elevation on the accuracy of geometric positioning error caused by atmospheric refraction, the atmospheric conditions of the central wavelength (0.675 μm) of panchromatic images obtained at 6:00 A.M. on 1 June 2016 were used, from which the geometric positioning error for an orbital altitude

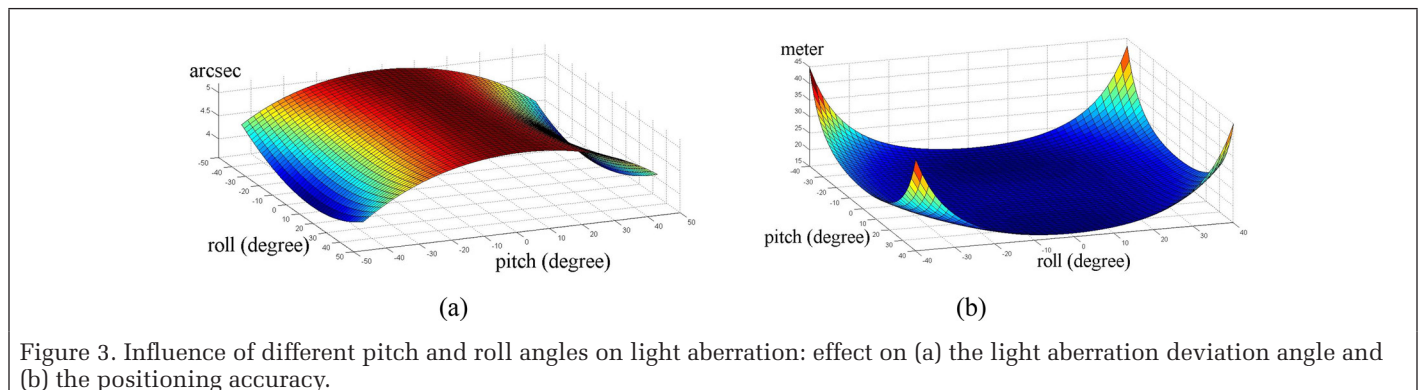


Figure 3. Influence of different pitch and roll angles on light aberration: effect on (a) the light aberration deviation angle and (b) the positioning accuracy.

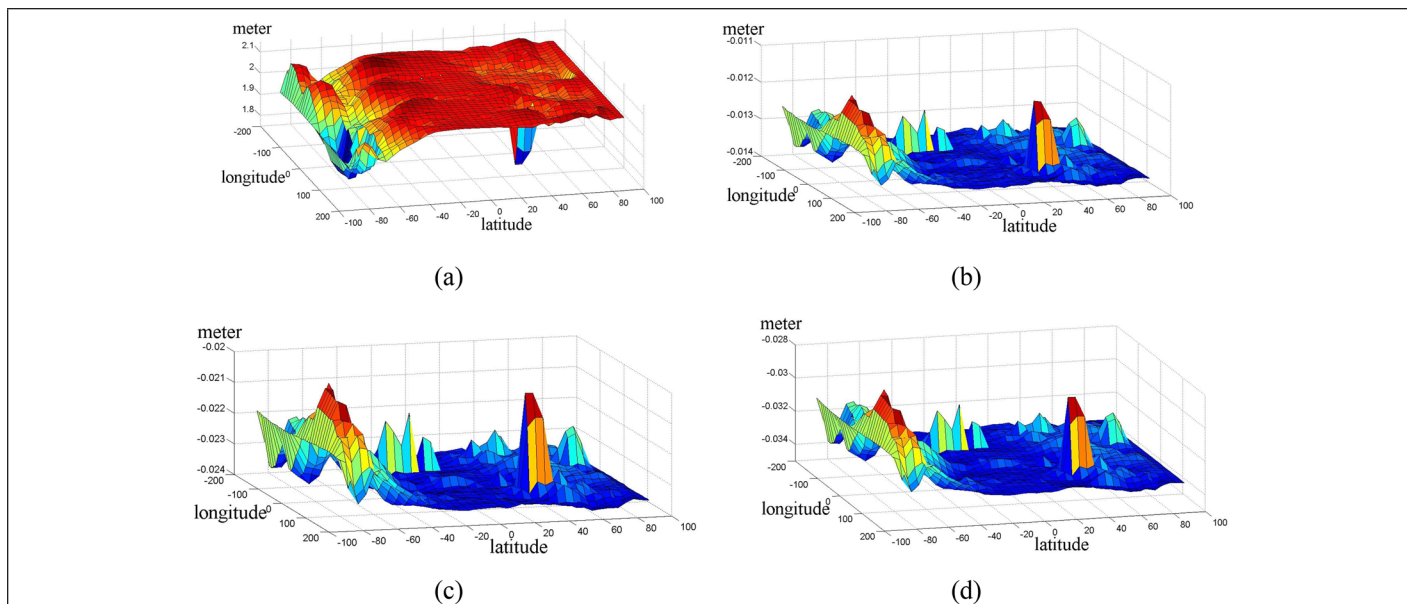


Figure 4. Positioning error caused by atmospheric refraction of four central wavelengths of different bands at each latitude and longitude: (a) blue central wavelength and the differences in the positioning errors between (b) green and blue, (c) red and blue, and (d) near-infrared and blue central wavelengths.

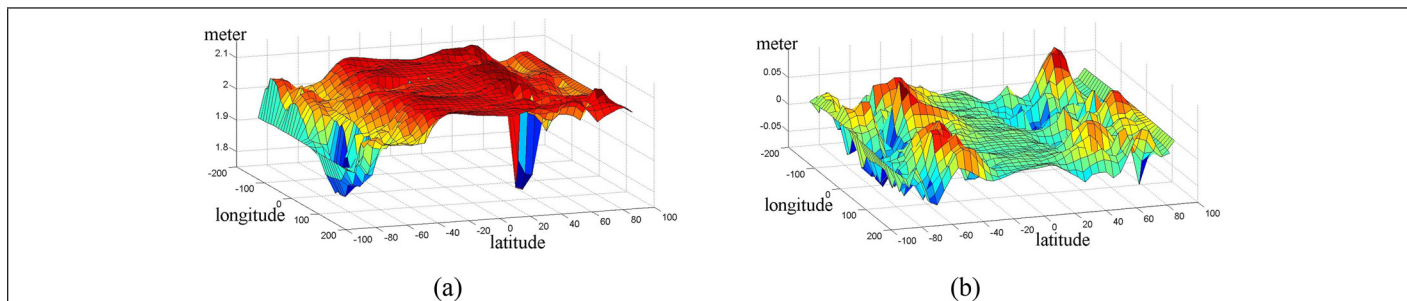


Figure 5. Positioning error caused by atmospheric refraction of the blue central wavelength at each latitude and longitude. (a) Blue central wavelength. (b) Difference in the positioning error at 6:00 A.M. on 1 December 2016 and 6:00 A.M. on 1 June 2016.

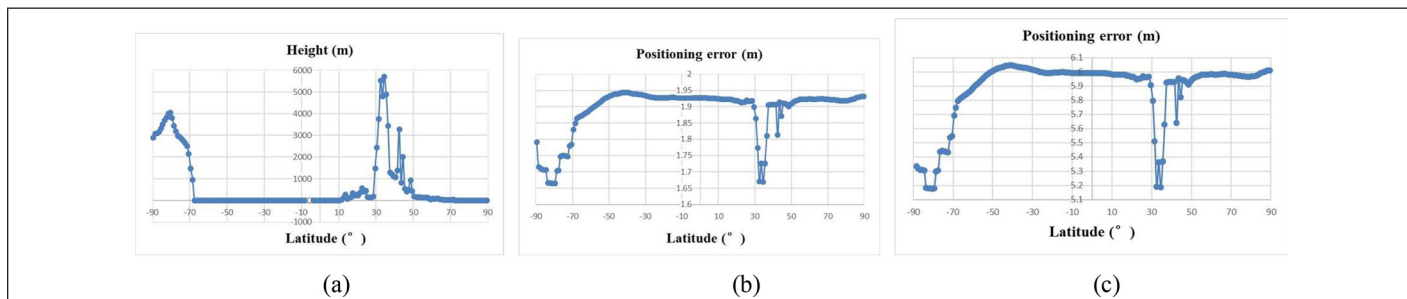


Figure 6. Positioning error caused by atmospheric refraction at 79.5° longitude and different latitudes. (a) The ground elevation value at 79.5° longitude. (b) Positioning error with a side view angle of 30° . (c) Positioning error with a side view angle of 45° .

of 500 km at 79.5° longitude was calculated with respect to the latitude. Figures 6a and 6b show the elevation information and the atmospheric refraction positioning error, respectively, at different latitudes along the 79.5° longitude line with a side view angle of 30° . Comparing Figures 6a and 6b, the geometric positioning error curve caused by atmospheric refraction is nearly opposite to the longitudinal trend of the ground elevation curve. That is, under certain conditions, the magnitude of the geometric positioning error caused by atmospheric refraction is approximately inversely correlated with the corresponding ground elevation. Figure 6c shows the geometric positioning error caused by atmospheric refraction at different latitudes along the 79.5° longitude line when the side view angle is 45° . Comparing Figures 6b and 6c, the variation trend of the geometric positioning error caused by

atmospheric refraction is still the same with different side view angles; larger side view angles are associated with larger geometric positioning errors caused by atmospheric refraction. Thus, the ground elevation of observation points and the side view angle are important factors for atmospheric refraction, with regard to positioning accuracy.

Orbital altitude: We examined the influence of the orbital altitude on positioning accuracy caused by atmospheric refraction, using the following conditions:

- a visible-light center wavelength of $0.675 \mu\text{m}$;
- atmospheric parameters from 6:00 A.M. on 1 June 2016;
- an imaging area with longitude, latitude, and elevation readings of 117.5° , 38.5° , and 2 m , respectively;

- orbital altitudes of 500 km (blue trend line) and 650 km (red trend line).

In Figure 7, under the same imaging conditions, higher orbital height was associated with greater atmospheric refraction offset caused by the side view angle. Additionally, the atmospheric refraction positioning error increased with side view angle.

Pitch and roll angles (side view angle):

From the analysis of subsections “Ground Elevation Value” and “Orbital Altitude”, the positioning error associated with atmospheric refraction becomes more significant as the side view angle increases. To further verify this conclusion, the atmospheric parameters of 6:00 A.M. on 1 June 2016 in subsection “Atmospheric Refraction Coefficient” were applied. The central wavelength of the blue band of 0.485 μm was set as the light wavelength, and the orbital altitude was 630 km. The atmospheric refraction positioning error at different latitudes and longitudes with different side view angles is shown in Figure 8. Comparing Figures 8a and 8b, the geometric positioning error caused by atmospheric refraction increased significantly with side view angle.

Relative Positioning Accuracy Analysis of the Light Aberration and Atmospheric Refraction Error

Light Aberration Error

The positioning error in one image caused by light aberration (Figure 3) is, most likely, an unsystematic error due to the different pitch and roll angles of different pixels. In this research, we examined the relative geometric positioning accuracy of satellite imagery of the Tangshan area, China, taken by three satellites: GaoFen2, ZiYuan302, and GaoFen6. The data information of the three test images is given in Table 3.

The LOS angle error of each image point caused by light aberration in three images of the Tangshan area is shown in Figure 9. The relative positioning errors in one image caused

by light aberration was far, <0.1 pixels. Therefore, the positioning errors caused by light aberration can be regarded as a systematic error for the entire image, without reducing the relative positioning accuracy in the single scene.

Figure 10a shows a maximum relative LOS angle error in the single scene of ~ 0.018 arcsec (~ 0.05 pixels) for pitch, roll, and yaw angles of -20.02° , -20.48° , and 2.73° , respectively. As shown in Figure 10b, the maximum relative LOS angle error in the single scene was ~ 0.025 arcsec (~ 0.07 pixels) when the pitch, roll, and yaw angles were -30.47° , -30.02° , and 2.73° , respectively. Therefore, the relative positioning error of one image from light aberration increases with the pitch and roll angles. When the relative LOS angle error caused by light aberration can be taken as a systematic error, we can use Equation 19 to compensate.

Atmospheric Refraction Error

As shown in Figure 11a, for traditional passive push-broom imaging modality, the field-of-view (FOV) angle cannot be neglected. Different CCD detectors have different roll angles, ψ_x , whereas the pitch angles, ψ_y , are nearly the same. Therefore, the size and direction of the atmospheric refraction error

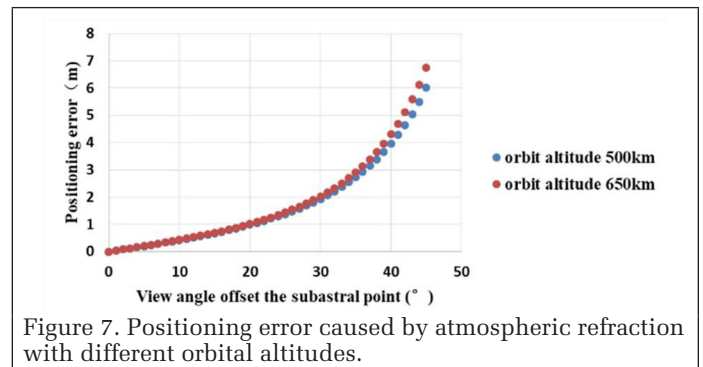


Figure 7. Positioning error caused by atmospheric refraction with different orbital altitudes.

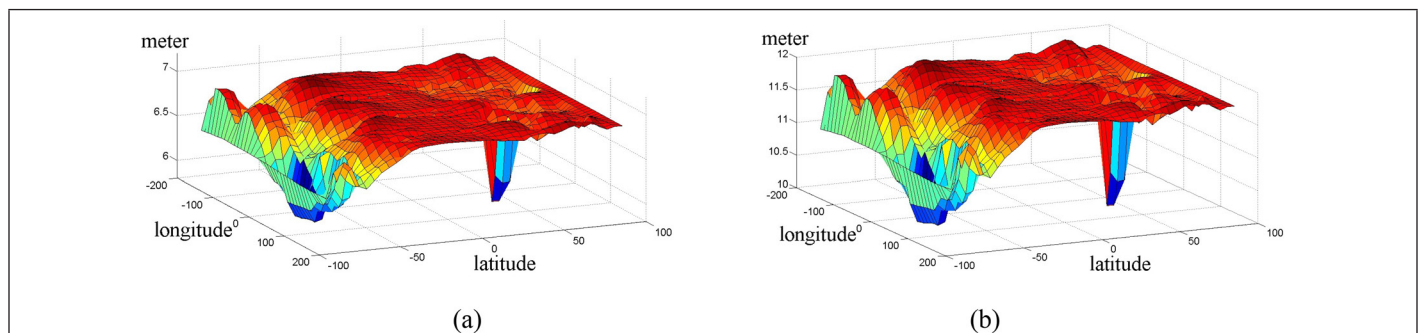


Figure 8. Positioning error caused by atmospheric refraction with different side view angles. Side view angle of (a) 45° and (b) 50° .

Table 3. Data information of the three test images.

Satellite	Resolution (m)	Image Width (km)	Altitude (km)	FOV ($^\circ$)	Pitch ($^\circ$)	Roll ($^\circ$)	Yaw ($^\circ$)
GaoFen2	0.8	23	about 630	2.15	0.0010	-8.9948	2.8488
ZiYuan302	2.1	50	about 505	5.79	-0.0011	-12.4992	2.7339
GaoFen6	2.0	90	about 630	8.6	-0.0206	4.9915	2.8813

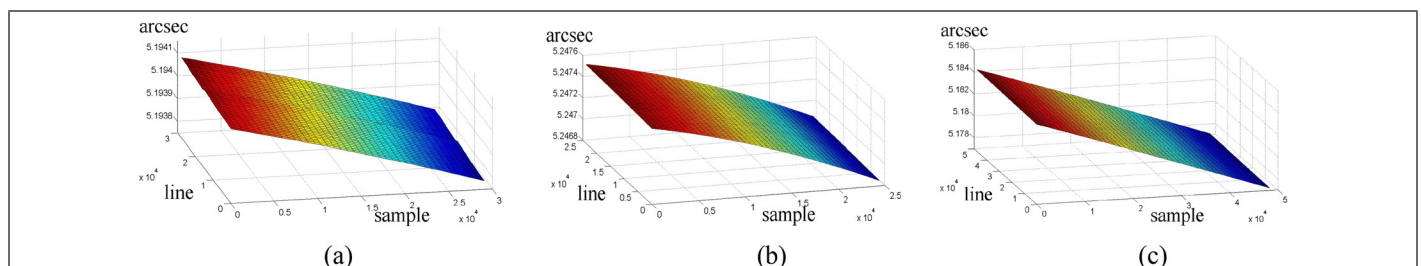


Figure 9. Line of sight (LOS) angle error caused by the light aberration in one image. (a) GaoFen2 image. (b) ZiYuan302 image. (c) GaoFen6 image.

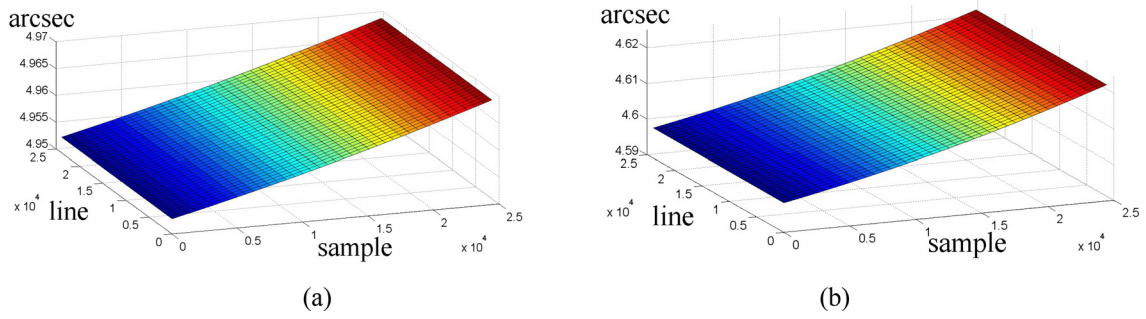


Figure 10. LOS angle error caused by light aberration in simulated ZiYuan302 image. (a) Imaging condition 1. (b) Imaging condition 2.

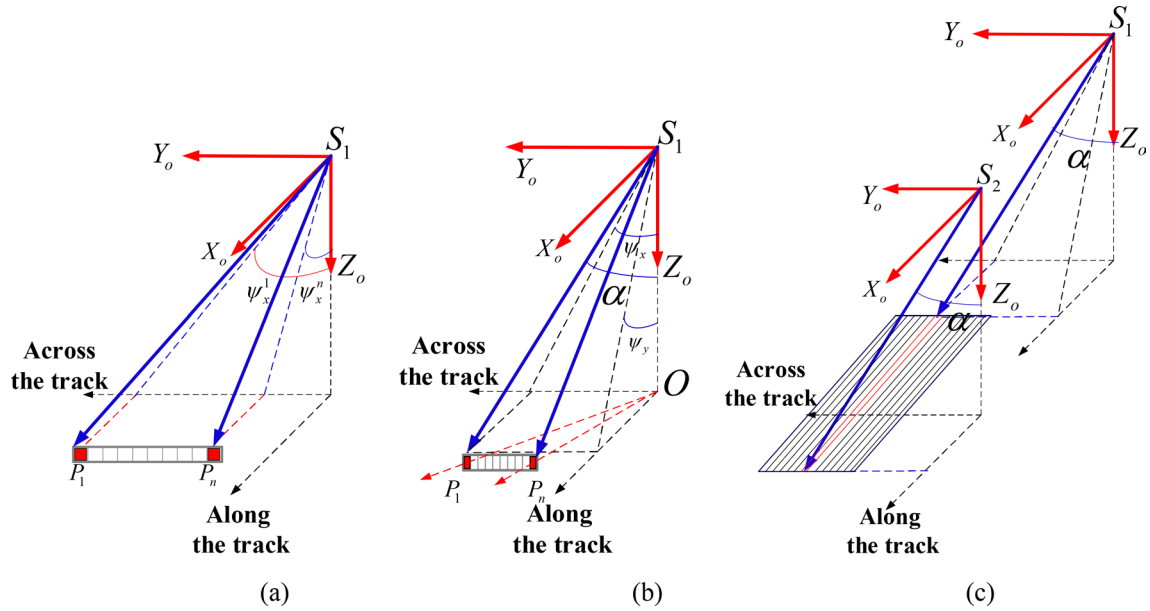


Figure 11. Different roll and pitch angles in one image.

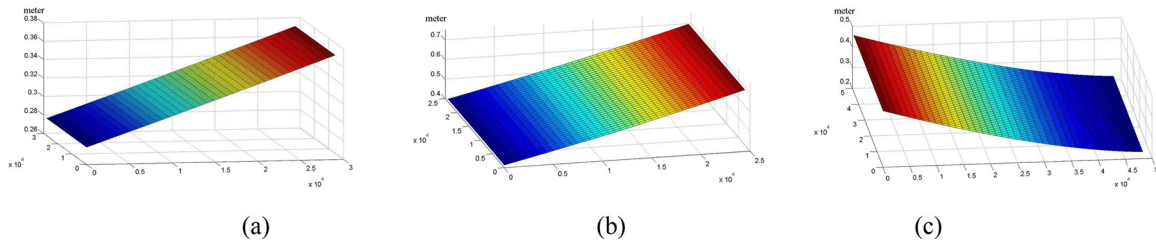


Figure 12. LOS angle error caused by the atmospheric refraction in one image. (a) GaoFen2 image. (b) ZiYuan302 image. (c) GaoFen6 image.

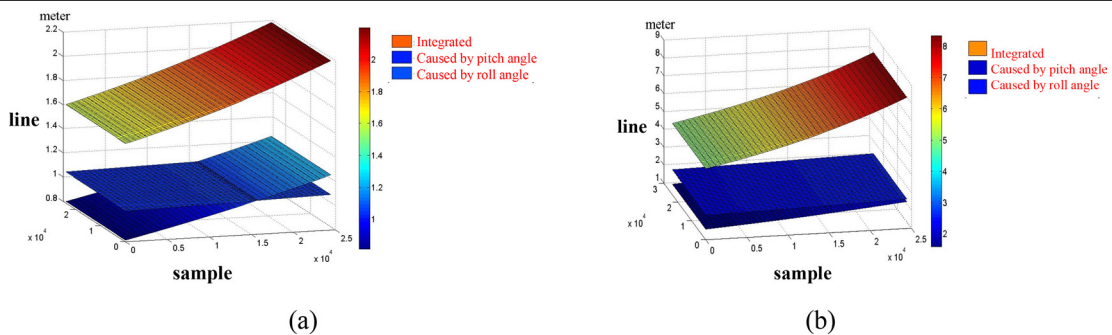


Figure 13. Atmospheric refraction errors under different pitch and roll angle imaging conditions for the simulated ZiYuan302 image. (a) Imaging condition 1. (b) Imaging condition 2.

of different CCD detectors also differ, as shown in Figure 11b, which causes unsystematic error and influences the internal relative positioning accuracy. From this, we can conclude that unsystematic error is also caused mainly by the FOV of the satellite camera. For passive push-broom imaging modality, the side view angles of the pixels in the same column are nearly the same; the atmospheric refraction relative error mainly embodies across the track in one image, as shown in Figure 11c. Thus, the unsystematic characteristics of the error become more obvious as the absolute value of the side view angle increases (Figure 6).

Figure 12 shows the LOS angle error caused by the atmospheric refraction in one image, and the atmospheric conditions of the central wavelength (0.675 μm) of panchromatic images obtained at 6:00 A.M. on 1 June 2016 were used. When $\alpha < 50^\circ$, $\alpha \approx \sqrt{\psi_x^2 + \psi_y^2}$ and the resulting relative geometric positioning errors of GaoFen2, ZiYuan302, and GaoFen6 images in Table 3 were < 0.1 m (~ 0.12 pixels), < 0.3 m (~ 0.15 pixels), and < 0.2 m (~ 0.1 pixels), respectively. The difference in the relative positioning error was mainly reflected across the track direction, which agrees well with the theoretical analysis.

Under the same atmospheric conditions, in Figure 13a, the pitch, roll, and yaw angles of the LOS in the scene center of the image were set to -21.25° , -20.48° , and 2.73° , respectively; in Figure 13b, the pitch, roll, and yaw angles of the LOS in the scene center of the image were -33.84° , -30.48° , and 2.73° , respectively. From Figures 13a and 13b, the relative positioning error caused by atmospheric refraction increased with side view angle, given the same FOV angle. In Figures 13a and 13b, the variations in integrated atmospheric refraction error in one image were ~ 0.6 m (~ 0.3 pixels) and 4 m (~ 2 pixels), respectively. Notably, the relationship between the atmospheric refraction error caused by the pitch and roll angles separately and the integrated atmospheric refraction error is not a simple Pythagorean relationship. When the geometric resolution of the satellite image is relatively low, and the side view angle is relatively small or the FOV angle is relatively small, the variation in the positioning error in one image caused by atmospheric refraction can be neglected. However, with improvements in the geometric resolution of satellite imagery and the capabilities of satellite agile imaging, the relative geometric positioning error caused by atmospheric refraction in one image must be accounted for carefully.

Analysis of RFM Fitting Accuracy

To determine whether the more comprehensive geometric imaging model constructed in this paper, which takes into account atmospheric refraction and aberration correction, can be extended to compensate for the accuracy of a single scene based on the RFM, we examined the ability to fit the more comprehensive geometric imaging model. The three images listed in Table 3 were used to calculate the RFM parameters via the virtual control point method (Hanley, Yamakawa, and

Fraser 2002; Tao and Hu 2001). The fitting accuracy of the RFM was evaluated by setting uniformly distributed virtual checkpoints; the corresponding residual error report was the output. The results are shown in Table 4. In addition, we simulated the agile satellite images with large pitch and roll angles to evaluate the applicability and generality of the RFM, and the results are shown in Table 5.

In Table 4, the maximum residual error and root-mean-square error of RFM fitting were both < 0.001 pixels. In Table 5, the RFM fitting error were also small enough to replace the more comprehensive geometric imaging model constructed in this paper, even when the pitch and roll angles were relatively large. We can conclude that the applicability of RFM for the proposed imaging model is the same as the one of RFM for the traditional imaging model. Therefore, the RFM can effectively replace the more comprehensive imaging geometric model constructed in this paper. This will greatly expand the application scope of the more comprehensive imaging geometric model, which can be used as the core model in high-precision geometric preprocessing of agile satellite images, and completely replaces the traditional geometric imaging model.

Discussion

In a real scenario, the light aberration and the atmospheric refraction both bring some errors to the real LOS angle. At the same time, the LOS angle is the main influencing factor of the light aberration error and atmospheric refraction error. Therefore, the light aberration and atmospheric refraction will interact with each other by drawing different errors into the LOS angle. However, their caused LOS angle errors are actually

Table 4. Fitting errors of RFM for different real satellite images.

Satellite	Checkpoint Number	Maximum Residual Error		Root-mean-square Error	
		X (pixel)	Y (pixel)	X (pixel)	Y (pixel)
Gaofen2	114 005	0.000086	0.000170	0.000019	0.000075
Ziyuan302	81 920	0.000598	0.000071	0.000063	0.000029
Gaofen6	305 045	0.000801	0.000346	0.000117	0.000063

Table 5. Fitting errors of RFM for simulated agile GaoJing-A satellite images.

Pitch (degree)	Roll (degree)	Maximum Residual Error		Root-mean-square Error	
		X (pixel)	Y (pixel)	X (pixel)	Y (pixel)
0	0	0.00786	0.000176	0.000092	0.000045
10	10	0.008282	0.000720	0.001139	0.000116
20	20	0.010239	0.001261	0.001381	0.000180
30	30	0.010562	0.002669	0.001976	0.000343
40	40	0.009229	0.008960	0.002529	0.001565

Table 6. Some preliminary suggestions on when the caused positioning error can be treated as systematic error.

Light Aberration	Orbital Altitude	Latitude of the Observation Point	Imaging Angles	
Absolute positioning	When the orbital altitude is constant	Have no significant impact	When the variation range of imaging angles is less than 10 degree	
Relative positioning	Have no significant impact	Have no significant impact	Have no significant impact	
Atmospheric Refraction	Atmospheric Refraction Coefficient	Ground Elevation Value	Orbital Altitude	Imaging Angles
Absolute positioning	Have no significant impact	Have no significant impact	When the orbital altitude is constant	When the variation range of imaging angles is less than 10 degree
Relative positioning	Have no significant impact	When the variation range of ground elevation value is less than 1000 m	Have no significant impact	When the imaging angles is less than 30 degree

small values compared with the real LOS angle based on the quantitative analysis. Thus, the mutual influence between the light aberration and the atmospheric refraction is so limited that can be ignored.

The light aberration and atmospheric refraction are naturally present in the imaging processes of the optical remote sensing satellite. The orbital altitude, latitude of the observation point, and imaging angles are three key factors of the light aberration. The atmospheric refraction coefficient, ground elevation value, orbital altitude, and imaging angles are four key factors of the atmospheric refraction. We give some preliminary suggestions on when the caused positioning error can be treated as systematic error in Table 6.

As can be seen in Table 6, in some cases, the positioning error caused by the light aberration and the atmospheric refraction error can be taken as the systematic error, and then can be compensated for by the calibrated installation angles based on the traditional imaging model. However, high resolution and flexible mobility are the characteristics of more and more optical remote sensing satellites; thus, the optical aberration and atmospheric refraction should better be compensated for by the proposed more comprehensive geometric imaging model. Therefore, it is necessary to select the reasonable imaging model based on the actual imaging condition of the optical remote sensing satellite.

Conclusions

In this paper, we introduce a more comprehensive geometric imaging model for an optical satellite that considers atmospheric refraction and aberration corrections for a more precise mapping relationship between image point coordinates and ground point coordinates of high-resolution remote sensing satellite imagery:

1. The formation mechanisms and characteristics of the light aberration error and atmospheric refraction error in optical remote sensing satellite imaging systems were systematically studied and discussed. Correction models were constructed based on our analysis results.
2. The traditional geometric imaging model of the optical remote sensing satellite was refined, and correction models for light aberration and atmospheric refraction were introduced into the traditional geometric imaging model to construct a more comprehensive geometric imaging model. The simplified more comprehensive geometric imaging model was then built under specific imaging conditions.
3. The feasibility of an extended RFM based on the constructed, more comprehensive, geometric imaging model was verified quantitatively, thus the applicability of the more comprehensive geometric imaging model was extended.

Acknowledgments

The authors would like to thank the editors and anonymous reviewers for their valuable comments, which helped improve this paper. Gaofen2, Gaofen6, and Ziyuan302 data were provided by CRESDA. This work was substantially supported by the National Science Fund for Distinguished Young Scholars (61825103) and the National Key Research and Development Program of China (2016YFB0501402). This support was valuable.

References

Baltsavias, E., Z. Li and H. Eisenbeiss. 2006. DSM generation and interior orientation determination of IKONOS images using a testfield in Switzerland. *Photogrammetrie Fernerkundung Geoinformation* 2006:41–54.

Cao, J., X. Yuan and J. Gong. 2015. In-orbit geometric calibration and validation of ZY-3 three-line cameras based on CCD-detector look angles. *The Photogrammetric Record* 30:211–226.

Chen, Y., Z. Xie, Z. Qiu, Q. Zhang and Z. Hu. 2015. Calibration and validation of ZY-3 optical sensors. *IEEE Transactions on Geoscience and Remote Sensing* 53 (8):4616–4626.

De Lussy, F., D. Greslou, C. Dechoz, V. Amberg, V.; J. M. Delvit, J. M.; L. Lebegue, L.; G. Blanchet, and G.; S. Fourest., S. 2012. Pleiades HR in flight geometrical calibration: Location and mapping of the focal plane. *ISPRS International Archives of the Photogrammetry, Remote Sensing and Spatial Information Sciences* 39:519–523.

Delvit, J., D. Greslou, V. Amberg, C. Dechoz, F. De Lussy, L. Lebegue, C. Lamy, S. Artigues and L. Bernard. 2012. Attitude assessment using Pleiades-HR capabilities. Pages 525–530 in *Proceedings of the International Archives of the Photogrammetry, Remote Sensing and Spatial Information Sciences*, Vol. 25, held in Melbourne, Australia.

Di, K., Y. Liu, B. Liu, M. Peng and W. Hu. 2014. A self-calibration bundle adjustment method for photogrammetric processing of Chang E-2 stereo lunar imagery. *IEEE Transactions on Geoscience and Remote Sensing* 52 (9):5432–5442.

Fraser, C. S. and H. B. Hanley. 2003. Bias compensation in rational functions for IKONOS satellite imagery. *Photogrammetric Engineering & Remote Sensing* 69 (1):53–57.

Gruen, A., S. Kocaman and K. Wolff. 2007. Calibration and validation of early ALOS/PRISM images. *The Journal of the Japan Society of Photogrammetry and Remote Sensing* 46:24–38.

Hanley, H. B., T. Yamakawa and C. S. Fraser. 2002. Sensor orientation for high-resolution satellite imagery. *International Archives of Photogrammetry Remote Sensing and Spatial Information Sciences* 34:69–75.

Jiang, Y., G. Zhang, X. Tang, D. Li, W. Huang and H. Pan. 2014. Geometric calibration and accuracy assessment of ZiYuan-3 multispectral images. *IEEE Transactions on Geoscience and Remote Sensing* 52 (7):4161–4172.

Noerdlinger, P. D. 1999. Atmospheric refraction effects in earth remote sensing. *ISPRS Journal of Photogrammetry & Remote Sensing* 54 (5–6):360–373.

Owens, J. C. 1967. Optical refractive index of air: Dependence on pressure, temperature and composition. *Applied Optics* 6 (1):51–59.

Stone, R. C. 1996. An accurate method for computing atmospheric refraction. *Publications of the Astronomical Society of the Pacific* 108 (729):1051.

Tao, C. V. and Y. Hu. 2001. A comprehensive study of the rational function model for photogrammetric processing. *Photogrammetric Engineering and Remote Sensing* 67 (12):1347–1358.

Thomas, A. H. and K. J. Quinn. 2012. The algorithm theoretical basis document for the atmospheric delay correction. NASA/TM–2012-208641, Vol. 8.

Poli, D. and T. Toutin. 2012. Review of developments in geometric modelling for high resolution satellite pushbroom sensors. *The Photogrammetric Record* 27 (137):58–73.

Wang, M., B. Yang, F. Hu and X. Zang. 2014. On-orbit geometric calibration model and its applications for high-resolution optical satellite imagery. *Remote Sensing* 6 (5):4391–4408.

Wang, M., Y. Cheng, X. Chang, S. Jin and Y. Zhu. 2017. On-orbit geometric calibration and geometric quality assessment for the high-resolution geostationary optical satellite GaoFen4. *ISPRS Journal of Photogrammetry and Remote Sensing* 125:63–77.

Yan, M., Z. Wang, Zhiyong, C. Wang and Chengyi, B. Yu. Bingyang 2015. Atmosphere refraction effects in object locating for optical satellite remote sensing images. *Acta Geodaetica et Cartographica Sinica* 44 (9):995–1002.

Zhang, Y., M. Zheng, J. Xiong, Y. Lu and X. Xiong. 2014. On-orbit geometric calibration of ZY-3 three-line array imagery with multistrip data sets. *IEEE Transactions on Geoscience and Remote Sensing* 52 (1):224–234.

Using 250-m MODIS Data for Enhancing Spatiotemporal Fusion by Sparse Representation

Liguo Wang, Xiaoyi Wang, and Qunming Wang

Abstract

Spatiotemporal fusion is an important technique to solve the problem of incompatibility between the temporal and spatial resolution of remote sensing data. In this article, we studied the fusion of Landsat data with fine spatial resolution but coarse temporal resolution and Moderate Resolution Imaging Spectroradiometer (MODIS) data with coarse spatial resolution but fine temporal resolution. The goal of fusion is to produce time-series data with the fine spatial resolution of Landsat and the fine temporal resolution of MODIS. In recent years, learning-based spatiotemporal fusion methods, in particular the sparse representation-based spatiotemporal reflectance fusion model (SPSTFM), have gained increasing attention because of their great restoration ability for heterogeneous landscapes. However, remote sensing data from different sensors differ greatly on spatial resolution, which limits the performance of the spatiotemporal fusion methods (including SPSTFM) to some extent. In order to increase the accuracy of spatiotemporal fusion, in this article we used existing 250-m MODIS bands (i.e., red and near-infrared bands) to downscale the observed 500-m MODIS bands to 250 m before SPSTFM-based fusion of MODIS and Landsat data. The experimental results show that the fusion accuracy of SPSTFM is increased when using 250-m MODIS data, and the accuracy of SPSTFM coupled with 250-m MODIS data is greater than the compared benchmark methods.

Introduction

Due to the power limitations of satellite sensors, it is difficult to acquire remote sensing data with both fine spatial and fine temporal resolutions. The Landsat satellite is capable of acquiring multispectral data with 30-m fine spatial resolution, and based on this characteristic, Landsat data have been widely applied to exploration of earth resources, agricultural, forestry and livestock management, and monitoring of natural disasters and environmental pollution at local scale (Goetz 2007; Anderson *et al.* 2012; van der Meer *et al.* 2012). However, the 16-day Landsat revisit cycle and cloud contamination limit its potential in monitoring dynamic changes on the Earth's surface. On the other hand, the Moderate Resolution Imaging Spectroradiometer (MODIS) on the *Terra/Aqua* platform can revisit the same scene once or twice per day, which can be applied to dynamic monitoring of vegetation phenology (Zhang *et al.* 2003; Ganguly *et al.* 2010) and land cover and land use (Hansen *et al.* 2000). However, the spatial resolution of MODIS data is 250–1000 m, and the ability to characterize the details of ground objects is very limited, especially for heterogeneous landscapes. In order to obtain remote sensing images with both fine spatial resolution and fine temporal

resolution for precise and timely monitoring, spatiotemporal fusion methods have been developed. Spatiotemporal fusion takes advantages of the spatial features of fine-spatial-resolution remote sensing data (e.g., Landsat data) and the temporal features of fine-temporal-resolution remote sensing data (e.g., MODIS data). The current spatiotemporal fusion methods can be divided into three main groups: weighting function-based, unmixing-based, and learning-based.

Among weighting function-based methods, Gao *et al.* (2006) first proposed a spatial and temporal adaptive reflectance fusion model (STARFM), which considers the differences in spectral, temporal, and spatial features between similar neighboring pixels. Hilker *et al.* (2009) proposed a spatial temporal adaptive algorithm for mapping reflectance change (STAARCH). That method introduces a tasseled cap transform to increase the prediction accuracy. On the basis of STARFM, Zhu *et al.* (2010) proposed enhanced STARFM (ESTARFM), which introduced a transfer coefficient to more reliably characterize the change rate of different land cover classes and has greater fusion accuracy for complex and heterogeneous regions. Wang and Atkinson (2018) proposed a three-step spatiotemporal fusion model called FIT-FC, which consists of regression model fitting, spatial filtering, and residual compensation. This method is especially advantageous for phenological changes.

With respect to unmixing-based methods, Zhukov *et al.* (1999) first proposed an unmixing-based multisensor multiresolution fusion model, which produces fine-spatial-resolution predictions directly according to the unmixing result from observed coarse-spatial-resolution images. Cherchali, Amram, and Flouzat (2000) and Fortin *et al.* (2000) proposed an approach to calculate fine-spatial-resolution pixel reflectance from coarse-spatial-resolution pixel reflectance based on a linear spectral mixture model. These methods fail to consider the intraclass spatial variability of land cover. Roy *et al.* (2008) proposed a semi-physical fusion model based on the assumption that the time variation of Landsat Enhanced Thematic Mapper and MODIS reflectance images are consistent. Wu *et al.* (2012) proposed a spatial and temporal data fusion approach to fuse MODIS and Landsat data based on the assumption that the temporal-change characteristics of the same land cover class within a coarse pixel are consistent. Wu *et al.* (2015) considered the spatial and temporal variations of pixel reflectivity jointly on the basis of this approach and proposed an improved method. This method is suitable for the cases involving missing remote sensing data. Zhu *et al.* (2016) proposed a flexible spatiotemporal data fusion (FSDAF) method, which integrates spatial unmixing and weighting schemes into one framework.

In recent years, sparse-representation theory has been applied widely in the field of image processing. For natural image processing, Yang *et al.* (2010) proposed an approach for image superresolution via sparse representation, which is one

Liguo Wang and Xiaoyi Wang are with the College of Information and Communication Engineering Harbin Engineering University, Harbin, China.

Qunming Wang (corresponding author) is with the College of Surveying and Geo-Informatics, Tongji University, Shanghai, China (wqm11111@126.com).

Photogrammetric Engineering & Remote Sensing
Vol. 86, No. 6, June 2020, pp. 383–392.
0099-1112/20/383–392

© 2020 American Society for Photogrammetry
and Remote Sensing
doi: 10.14358/PERS.86.6.383

of the earliest studies applying sparse-representation theory to image superresolution. Sparse representation has also been used in spatiotemporal fusion, in what can be called the learning-based models. Specifically, the approach utilizes dictionary learning to train feature vectors which are capable of representing high-frequency details of fine- and coarse-spatial-resolution images. These vectors constitute a matrix which is also referred to as an overcomplete dictionary. Based on the assumption that remote sensing images acquired by adjacent phases have similar spatial features, it is considered that the predicted fine-spatial-resolution image can be linearly represented by a small number of characteristic atoms in a fine-spatial-resolution patch-by-patch overcomplete dictionary. Huang and Song (2012) proposed the sparse representation-based spatiotemporal reflectance fusion model (SPSTFM). The model utilizes the image pairs (composed of differences in reflectance of data at different times) of MODIS and Landsat images before and after the prediction time to train fine- and coarse-spatial-resolution dictionaries representing temporal-change features. Subsequently, Song and Huang (2013) proposed a sparse representation-based spatiotemporal fusion model using only one known image pair. First, the sparse-representation algorithm is used to downscale a MODIS image to an intermediate spatial resolution and produce a transition image. High-pass modulation is then applied to fuse the observed Landsat Enhanced Thematic Mapper image and the transition image. The model reduces the number of required known image pairs, so that it can be applied in cases where only one image pair is available. The learning-based spatiotemporal fusion approaches including SPSTFM consider the spatial-feature information of land cover changes, and have shown superior performance for reproducing heterogeneous regions (Huang and Song 2012).

Spatiotemporal fusion is generally applied to images from different sensors, and the difference in spatial resolution is usually larger than 10 in zoom ratio. Specifically, the difference between the spatial resolutions of MODIS and Landsat data is about 16, which is a great challenge for spatiotemporal fusion. First, the large resolution difference exerts considerable influence on preprocessing such as registration. For example, a 10×10 patch in a Landsat image corresponds to a patch of less than 1×1 in a MODIS image. There exists great uncertainty in registration between MODIS and Landsat data. Second, the overcoarse-spatial-resolution images fail to provide sufficient spatial details relative to fine-spatial-resolution data, which imposes great uncertainty in the fusion process.

To solve these issues, Wang, Zhang *et al.* (2017) proposed area-to-point regression kriging (ATPRK; Wang, Shi, Atkinson and Zhao 2015) to generate 250-m intermediate-spatial-resolution MODIS data that are used as input in STARFM-based spatiotemporal fusion. It has been demonstrated that the use of 250-m MODIS data can increase the accuracy of STARFM to a certain extent. However, STARFM is inferior in restoring heterogeneous landscape and strong temporal changes (i.e., phenological changes of vegetation; Zhu *et al.* 2010). Instead, compared with several mainstream methods (such as STARFM, ESTARFM, Fit-FC, and FSDAF) which use only the information of neighboring pixels, SPSTFM fully considers the structural information of the entire image and extracts a large number of image patches for reconstruction. Obviously, SPSTFM uses more spatial information to predict fine-resolution images, and thus its predictions tend to have greater accuracy, especially for restoring heterogeneous landscape (Huang and Song 2012). In this article, we utilize ATPRK to fuse 250-m MODIS bands 1–2 with 500-m bands 3–7 to create the interim 250-m MODIS bands 1–7. Based on the learning-based spatiotemporal fusion algorithm SPSTFM, the 30-m *Landsat 8* Operational Land Imager (OLI) data are blended with the 250-m fused MODIS time series to produce 30-m Landsat-like time-series data.

The rest of this article is divided into four sections. In the first, we briefly introduce the theoretical knowledge of ATPRK for fusion of 500-m and 250-m MODIS bands and SPSTFM for fusion of 250-m ATPRK-derived MODIS data and 30-m Landsat data. The experimental results based on two data sets are provided in the next section. In the following section, the sparse representation-based method and results are further discussed. In the final section, we conclude this article.

Methods

In this section, the principles of ATPRK and SPSTFM are briefly introduced.

ATPRK

ATPRK has shown to be an advanced pan-sharpening (or more general multiresolution image fusion) approach (Wang, Shi, Atkinson and Zhao 2015; Wang, Shi and Atkinson 2016; Wang, Zhang *et al.* 2017). It can be divided into two parts: regression modeling and area-to-point kriging (ATPK)-based residual downscaling. In this article, we apply this approach to merge the 250-m bands and 500-m bands of MODIS data. ATPRK is performed for each 500-m band separately. The two specific parts of MODIS image fusion are described next.

Regression Modeling

The regression modeling includes three steps. First, according to the spectral similarity between 250-m and 500-m MODIS bands (measured by correlation coefficient [CC]), a band with a larger CC is selected from 250-m band 1 or 2 for each observed 500-m band. Second, the selected 250-m band is upsampled to 500 m. Third, a regression model between the observed 500-m band and the upsampled 500-m band in the second step is built, where the parameters are estimated by the ordinary least-squares method. It is assumed that the linear relationship is universal at different spatial resolutions. Thus, the linear relationship established at 500 m can be applied to 250 m (Wang, Shi, Atkinson and Zhao 2015).

Downscaling Residuals Based on ATPK

Normally, there is residual between regression prediction and original data, that is, a 500-m residual in the constructed regression model. In the second part, the 500-m residual is downsampled to 250 m by ATPK, and the estimated 250-m residual is added to the 250-m data predicted in the first step to produce the final 250-m fusion data. Since the iterative process of ATPK will increase the computing time, in this article we utilized simple and fast bicubic interpolation to achieve residual downscaling. The experimental result of bicubic interpolation not only is approximate to the predicted result by ATPK but also greatly reduces the computing time. More details on ATPRK can be found in our previous research (Wang, Shi, Atkinson and Zhao 2015; Wang, Shi and Atkinson 2016).

SPSTFM

In this article, the input for SPSTFM is the 250-m MODIS data set predicted by ATPRK, rather than the observed 500-m MODIS data in the original SPSTFM. The flowchart of the proposed scheme is shown in Figure 1; further details of ATPRK are given by Wang, Shi, Atkinson, and Zhao (2015, figure 1). We denote the Landsat and MODIS images at t_i as \mathbf{L}_i and \mathbf{M}_i , respectively, and their corresponding k th patches as \mathbf{l}_i^k and \mathbf{m}_i^k . Let \mathbf{L}_{ij} and \mathbf{M}_{ij} represent the fine- and coarse-spatial-resolution difference images between t_i and t_j , and \mathbf{l}_{ij}^k and \mathbf{m}_{ij}^k their corresponding k th patches. Consistent with the requirements of input data for ESTARFM (Zhu *et al.* 2010), SPSTFM needs two known Landsat-MODIS image pairs at t_1 and t_3 , and the goal is to predict the Landsat-like image at t_2 based on the corresponding MODIS image. In sparse representation, the dictionary-updating algorithm is used to train fine- and coarse-spatial-resolution overcomplete dictionaries which represent the similarity-structure information. Then the

sparse-representation coefficients are calculated to predict the Landsat-like image. The details are summarized as follows.

The fine- and coarse-spatial-resolution difference images \mathbf{L}_{31} and \mathbf{M}_{31} are divided into overlapped patches. From the patch set, the fine- and coarse-spatial-resolution samples are randomly selected to form the training-sample matrices \mathbf{Y} and \mathbf{X} , where the same column of \mathbf{Y} and \mathbf{X} corresponds to the same training sample. Considering the large difference between fine- and coarse-spatial-resolution difference images in each band, \mathbf{Y} and \mathbf{X} need to be normalized for each band:

$$\mathbf{Y}_i = \frac{\mathbf{Y}_i - \mu_{x_i}}{\sigma_{x_i}}, \mathbf{X}_i = \frac{\mathbf{X}_i - \mu_{x_i}}{\sigma_{x_i}}, \quad (1)$$

where μ_{x_i} and σ_{x_i} are the mean and variance of the i th band \mathbf{X}_i , respectively.

By optimizing the following objective function, the K-SVD algorithm (Aharon, Elad and Bruckstein 2006) is applied to train the coarse-spatial-resolution dictionary \mathbf{D}_i using \mathbf{X} :

$$\{\mathbf{D}_i, \Lambda\} = \arg \min_{\mathbf{D}_i, \Lambda} \left\{ \|\mathbf{X} - \mathbf{D}_i \Lambda\|_F^2 \right\}$$

subject to

$$\forall i, \|\mathbf{a}_i\|_0 \leq K_0, \quad (2)$$

where Λ is the column combination of the sparse-representation coefficients for each patch in \mathbf{X} , \mathbf{a}_i is the row vector in Λ , and K_0 is the maximum value of the number of nonzero components in \mathbf{a}_i . The mapping relationship between the fine- and coarse-spatial-resolution training samples is established by assuming that the sparse-representation coefficient set Λ is the same at different spatial resolutions. Thus, the fine-spatial-resolution dictionary \mathbf{D}_h can be directly calculated by applying the pseudoinverse expression:

$$\mathbf{D}_h = \mathbf{Y}(\Lambda)^+ = \mathbf{Y}\Lambda^T(\Lambda\Lambda^T)^{-1}. \quad (3)$$

Taking the coarse-spatial-resolution difference image \mathbf{M}_{21} as the input, the sparse coefficient \mathbf{a}_k of dictionary \mathbf{D}_i for the k th patch \mathbf{m}_{21}^k is calculated by using the sparse-coding technique of orthogonal matching pursuit (Davis, Mallat and Avelaneda 1997). Since the sparse-representation coefficients for dictionaries at fine and coarse spatial resolutions are assumed to be identical, the corresponding k th fine-spatial-resolution difference-image patch can be calculated by $\mathbf{l}_{21}^k = \mathbf{D}_h * \mathbf{a}_k$.

Similarly, \mathbf{l}_{32}^k can be estimated in the same way. Considering the difference in the degree of change between different periods, corresponding temporal weights are calculated when reconstructing the fine-spatial-resolution patch. Finally, the k th fine-spatial-resolution patch at t_2 is predicted:

$$\mathbf{l}_2^k = \omega_1^k * (\mathbf{l}_1^k + \mathbf{l}_{21}^k) + \omega_3^k * (\mathbf{l}_3^k - \mathbf{l}_{32}^k), \quad (4)$$

where ω_1^k and ω_3^k are the weights of two separate predictions, respectively, and the weights are determined by

$$\omega_i^k = \frac{1/v_i^k}{1/v_1^k + 1/v_3^k}, \quad (i = 1, 3). \quad (5)$$

In Equation 5, v_i^k represents the absolute average change between MODIS images at two times (denoted as U) for patch \mathbf{m}_{ij}^k . The value of U is calculated based on the sum of the normalized vegetation index, the normalized difference built-up index (He *et al.* 2010), and the modified normalized difference water index (Xu 2005). The reconstructed patches are sequentially combined to restore the entire image. Note that there is overlap between neighboring patches. In order to ensure the continuity of the entire reconstructed image, the pixel values on the overlapped parts are averaged.

Experiments

In this section, two data sets of *Landsat 8* OLI and MODIS surface reflectance images covering two areas (i.e., Coleambally and Lower Gwydir Catchments, Australia) were used for experimental verification. The MODIS data were from the 8-day composite surface reflectance products of MOD09A1 (500 m) and MOD09Q1 (250 m). We took the original 500-m MODIS data and the ATRPK-fused 250-m data as input for SPSTFM, and the two schemes were compared. Moreover, using the same input of 250-m fused MODIS data, SPSTFM was compared with the well-known STARFM and ESTARFM methods, and the results are described explicitly in the following sections.

Experiment on the Coleambally Data Set

Three pairs of *Landsat 8* OLI and MODIS surface reflectance images covering a 28×28 km region of Coleambally were used in this experiment. The data sets are characterized by seasonal changes and were acquired on July 6, 2013, August 14, 2013, and September 8, 2013. Figure 2 shows the images with near-infrared (NIR)-red-green as red-green-blue composite

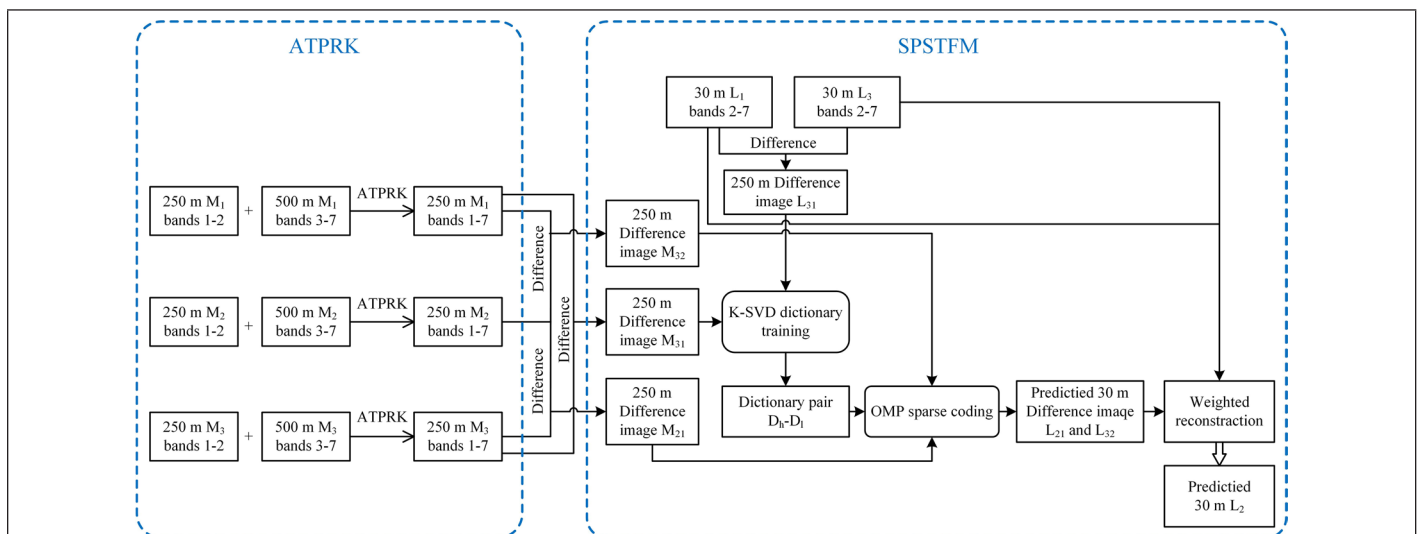


Figure 1. Flowchart illustrating the proposed scheme of using 250-m MODIS data for enhancing spatiotemporal fusion of MODIS and Landsat data by sparse representation. (Further details on area-to-point regression kriging are given by Q. Wang, Shi, Atkinson and Zhao 2015; Q. Wang, Shi and Atkinson 2016).

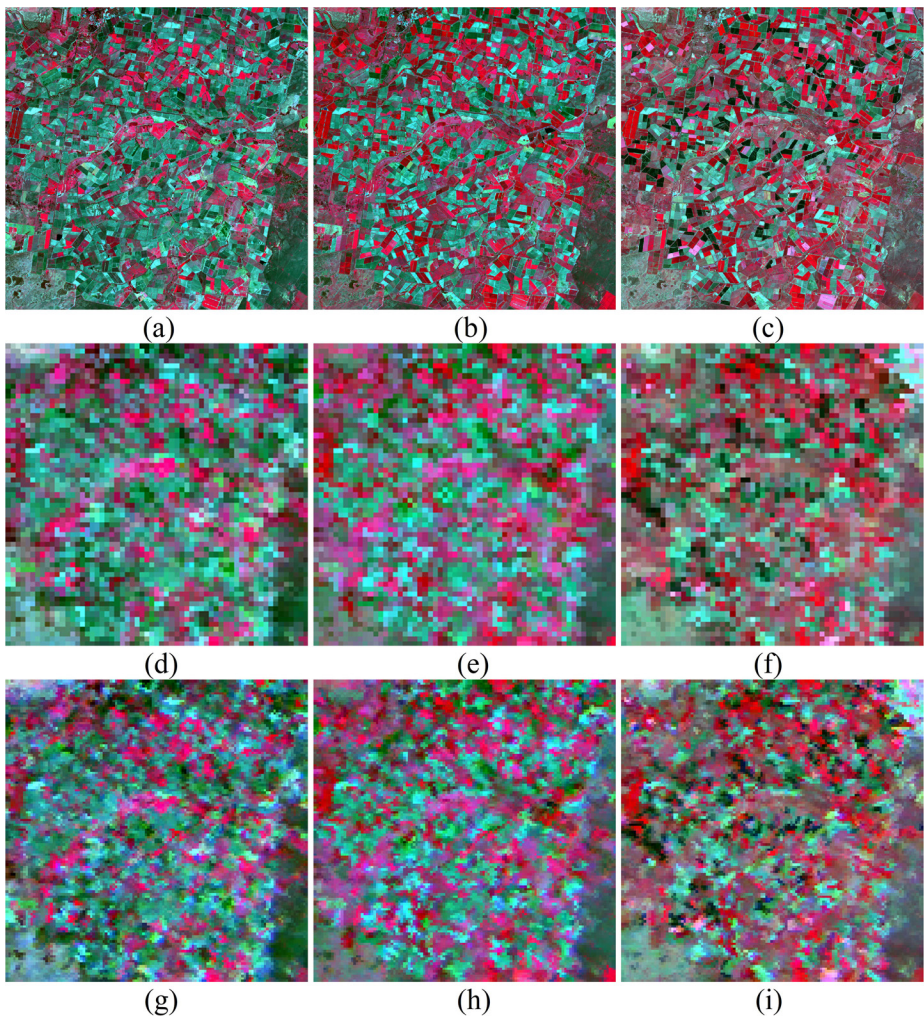


Figure 2. The Coleambally data set (near-infrared-red-green as RGB). (a to c) Landsat surface reflectance data. (d to f) MODIS surface reflectance data. (g to i) The corresponding 250-m ATRPK-fused MODIS images. Left to right: Data acquired on July 6, 2013, August 14, 2013, and September 8, 2013.

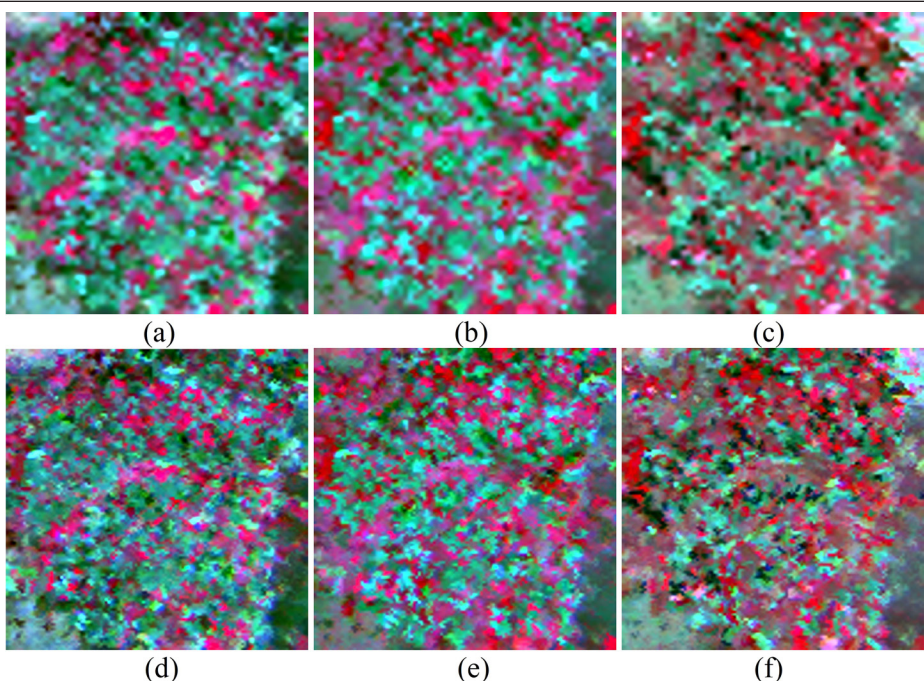


Figure 3. The 30-m interpolated results of the MODIS data set for the Coleambally area. (a to c) 30-m bicubic interpolation results of observed 500-m data. (d and e) 30-m bicubic interpolation results of the ATRPK-fused 250-m data.

for the 30-m Landsat data (upper row), 500-m MODIS data (middle row), and 250-m fused MODIS data (lower row). The bicubic interpolation approach was then performed to downscale the 500-m and 250-m MODIS data to 30 m, which were used as input for spatio-temporal fusion, as shown in Figure 3. As can be seen Figures 2d–2i and 3, the 250-m fused data undoubtedly provide more abundant information (e.g., clearer boundary between different land cover classes) than the 500-m data. This can be illustrated by the variances of the data. Table 1 shows the variances of the six bands in the three pairs of 500-m and 250-m MODIS images. Taking the NIR band on July 6, 2013, as an example, the variance of the 500-m NIR band is 27.4462×10^{-4} , and that of the 250-m NIR band is 38.0577×10^{-4} . Clearly, the variances of 250-m data are larger, suggesting that they contain more spatial details than the 500-m original images. Based on SPSTFM, the task of our experiment is to predict the 30-m Landsat image on August 14, 2013, by taking as input two pairs of Landsat-MODIS images on July 6, 2013, and September 8, 2013, and the MODIS image on August 14, 2013. The actual 30-m Landsat image acquired on August 14, 2013, was used as reference for evaluating the accuracy of the fusion results.

Figure 4 shows the coarse-spatial-resolution dictionary atoms trained using six bands of 500-m data and 250-m data. It can be seen that the 250-m dictionary atoms present more spatial details, while the 500-m dictionary atoms are smoother. Figure 5 shows the 30-m fusion results of SPSTFM (using 500-m or 250-m MODIS images as input) and STARFM and ESTARFM (using 250-m MODIS images as input). Also, the results for two 1.5×1.5 km heterogeneous regions (marked in yellow in Figure 5a) are shown in the middle and lower rows. Generally, two observations can be made.

First, for SPSTFM, compared with the 30-m Landsat predictions produced using 500-m MODIS images, the 30-m predictions produced using the 250-m image are visually more accurate. For example, in subarea S1, some green pixels are incorrectly predicted by SPSTFM as red pixels using a 500-m image. However, when using the 250-m data, the predictions of green pixels are more satisfactory for SPSTFM, and the color of the pixels is much closer to the reference.

Second, using the same 250-m MODIS data, SPSTFM produces more accurate results than the other two methods. This can be illustrated by checking the restoration of the green

Table 1. Variances ($\times 10^{-4}$) of the 500-m and 250-m MODIS images.

Band	July 6, 2013		August 14, 2013		September 8, 2013	
	500 m	250 m	500 m	250 m	500 m	250 m
Blue	0.3493	0.3976	0.3746	0.4389	0.5601	0.6485
Green	0.4977	0.5430	0.4131	0.4470	1.1528	1.3226
Red	1.9266	2.9863	1.7781	2.8175	2.8274	4.3367
NIR	27.4462	38.0577	41.1098	61.3962	37.7855	56.4422
SWIR1	6.9214	7.5548	4.6227	5.1424	13.7667	15.4255
SWIR2	7.7068	8.8241	5.0401	5.8113	11.3330	13.0472

NIR = near-infrared; SWIR = shortwave infrared.

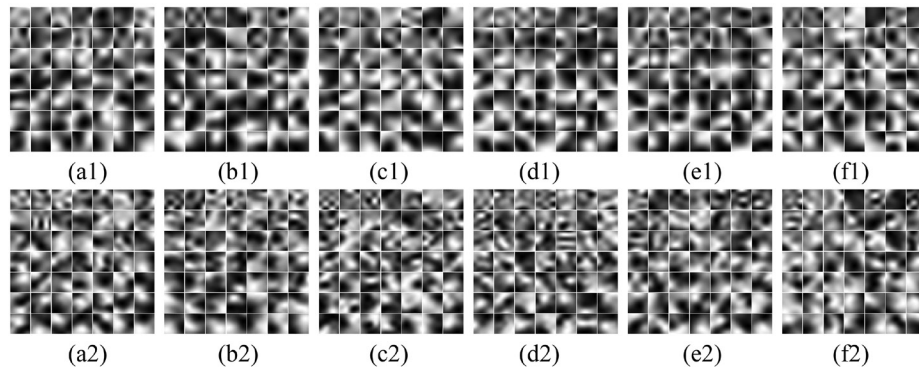


Figure 4. The dictionary atoms produced from the MODIS data set for the Coleambally area. (a1 to f1) Dictionary atoms obtained by training the 500-m data for six bands. (a2 to f2) Dictionary atoms obtained by training the 250-m data for six bands. Left to right: Atoms for MODIS blue, green, red, near-infrared, shortwave infrared 1, and shortwave infrared 2 bands.

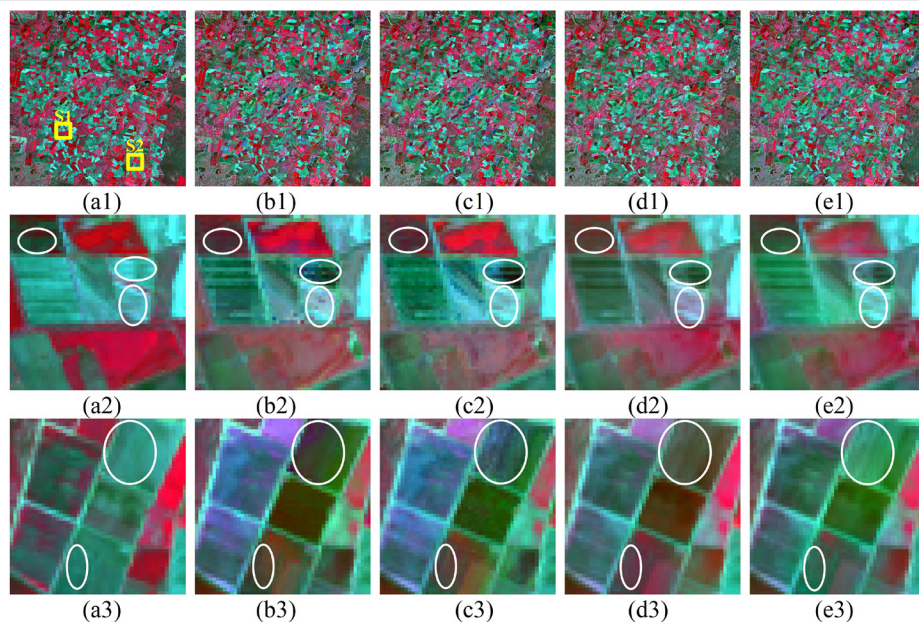


Figure 5. 30-m spatiotemporal fusion results for the Coleambally data set. (a) 30-m true Landsat 8 image on July 6, 2013 (the two heterogeneous subareas marked in yellow are used for analysis in lines 2 and 3). (b) 30-m ESTARFM results predicted using the 250-m fused MODIS images. (c) 30-m STARFM results predicted using the 250-m fused MODIS images. (d and e) 30-m SPSTFM results predicted using the original 500-m MODIS images and the 250-m fused MODIS images, respectively. Line 1 shows the results for the whole area, and lines 2 and 3 are the results for the two heterogeneous subareas (S1 and S2) marked in (a).

pixels in subarea S2. For STARFM and ESTARFM predictions, the color of the original green pixels at the center location is not satisfactorily restored. SPSTFM, however, can reproduce the color of the pixels more reliably—not only the green pixels at the center location, but also the ones at the left side. In addition, SPSTFM can produce more accurate predictions for land cover changes than STARFM and ESTARFM. As can be seen from Figure 6, from September 8, 2013, to August 14, 2013, there exist noticeable land cover changes. For example, in the

marked subarea, there are abrupt changes for the red patch at the left part. Compared with ESTARFM and STARFM, SPSTFM can identify the contours of the changed patch more satisfactorily.

Table 2 lists the quantitative evaluation results for the three methods (STARFM, ESTARFM, and SPSTFM). Here, we considered four commonly used indices for evaluating remote sensing image fusion methods: root-mean-square error (RMSE), CC, structural-similarity index (SSIM; Wang *et al.* 2004), and spectral angle mapper (SAM; Kruse *et al.* 1993).

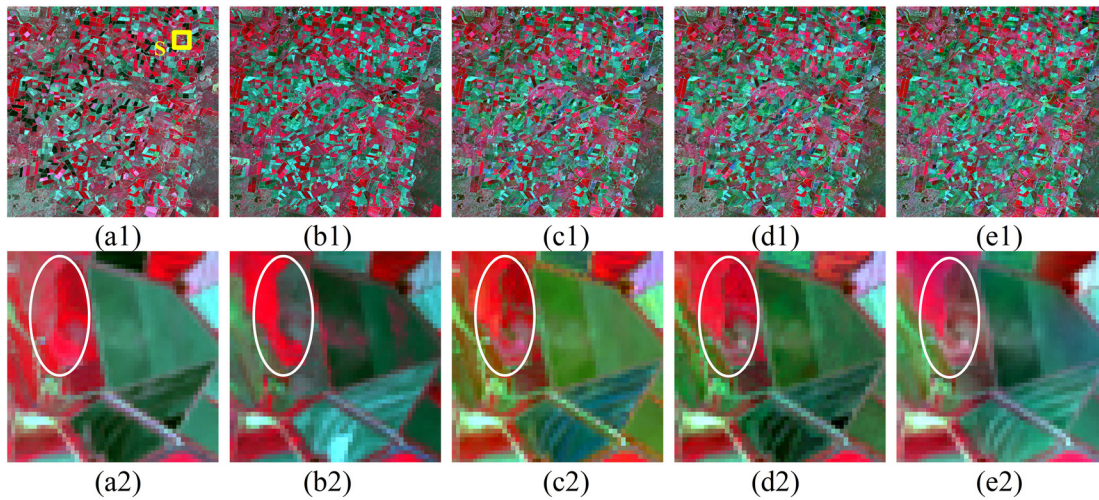


Figure 6. Predictions of land cover changes from September 8, 2013, to August 14, 2013. (a) 30-m true *Landsat 8* image on September 8, 2013 (the subarea marked in yellow is used for analysis in line 2). (b) 30-m true *Landsat 8* image on August 14, 2013. (c) 30-m ESTARFM results predicted using the 250-m fused MODIS images. (d) 30-m STARFM results predicted using the 250-m fused MODIS images. (e) 30-m SPSTFM results predicted using the 250-m fused MODIS images. Line 1 shows the results for the whole area, and line 2 is the results for the heterogeneous subarea marked in (a).

Table 2. Quantitative assessment for the Coleambally data set.

Band	ESTARFM	STARFM	SPSTFM	
	250-m MODIS	250-m MODIS	500-m MODIS	250-m MODIS
RMSE				
Blue	0.0099	0.0083	0.0094	0.0088
Green	0.0111	0.0103	0.0110	0.0100
Red	0.0177	0.0160	0.0171	0.0149
NIR	0.0415	0.0459	0.0415	0.0360
SWIR1	0.0476	0.0375	0.0454	0.0430
SWIR2	0.0420	0.0331	0.0417	0.0409
Mean	0.0283	0.0252	0.0277	0.0256
CC				
Blue	0.8043	0.8315	0.8422	0.8686
Green	0.7692	0.7901	0.7754	0.8147
Red	0.8327	0.8532	0.8435	0.8889
NIR	0.9197	0.9162	0.9203	0.9409
SWIR1	0.6824	0.7339	0.7542	0.8009
SWIR2	0.7880	0.8098	0.8330	0.8519
Mean	0.7994	0.8225	0.8281	0.8610
SSIM				
Blue	0.7933	0.8250	0.8256	0.8516
Green	0.7682	0.7898	0.7737	0.8112
Red	0.8264	0.8483	0.8353	0.8783
NIR	0.9189	0.9101	0.9154	0.9370
SWIR1	0.6748	0.7306	0.7403	0.7814
SWIR2	0.7619	0.7967	0.7932	0.8053
Mean	0.7905	0.8167	0.8139	0.8441
SAM	0.1330	0.1153	0.1291	0.1374

CC = correlation coefficient; NIR = near-infrared; RMSE = root-mean-square error; SAM = spectral angle mapper; SSIM = structural-similarity index; SWIR = shortwave infrared.

Table 3. Quantitative assessment for the Lower Gwydir Catchments data set.

Band	ESTARFM	STARFM	SPSTFM	
	250-m MODIS	250-m MODIS	500-m MODIS	250-m MODIS
RMSE				
Blue	0.0123	0.0154	0.0101	0.0100
Green	0.0182	0.0235	0.0151	0.0149
Red	0.0227	0.0306	0.0198	0.0190
NIR	0.0284	0.0315	0.0265	0.0256
SWIR1	0.0323	0.0409	0.0273	0.0271
SWIR2	0.0245	0.0286	0.0199	0.0194
Mean	0.0231	0.0284	0.0198	0.0193
CC				
Blue	0.8690	0.7977	0.8974	0.9038
Green	0.8544	0.7609	0.8874	0.8955
Red	0.8725	0.7665	0.8846	0.9034
NIR	0.8613	0.8092	0.8722	0.8907
SWIR1	0.8952	0.8440	0.9224	0.9267
SWIR2	0.9028	0.8798	0.9314	0.9350
Mean	0.8759	0.8097	0.8992	0.9057
SSIM				
Blue	0.8657	0.7912	0.8948	0.9092
Green	0.8508	0.7545	0.8846	0.8915
Red	0.8690	0.7619	0.8822	0.8994
NIR	0.8567	0.8040	0.8680	0.8835
SWIR1	0.8941	0.8404	0.9203	0.9245
SWIR2	0.9014	0.8737	0.9314	0.9350
Mean	0.8729	0.8043	0.8969	0.9058
SAM	0.0565	0.0730	0.0491	0.0482

CC = correlation coefficient; NIR = near-infrared; RMSE = root-mean-square error; SAM = spectral angle mapper; SSIM = structural-similarity index; SWIR = shortwave infrared.

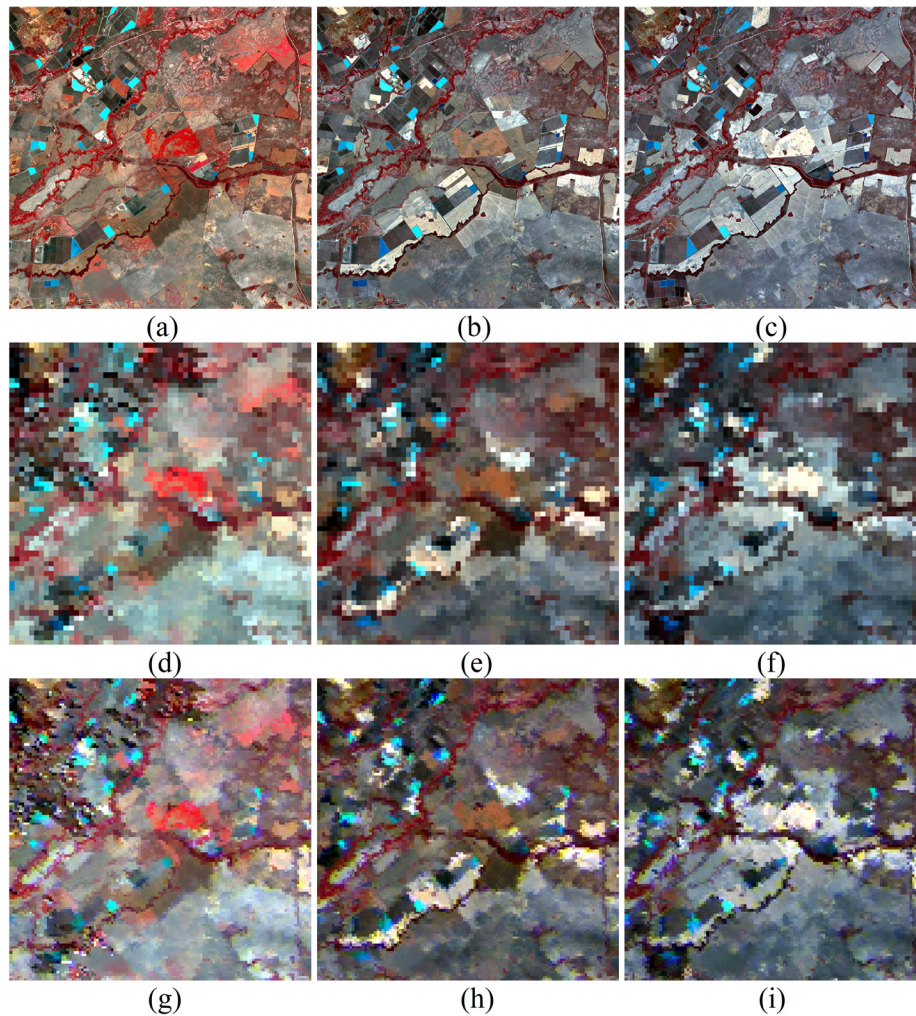


Figure 7. The Lower Gwydir Catchments data set (near-infrared-red-green as RGB). (a to c) Landsat surface reflectance data. (d to f) MODIS surface reflectance data. (g to i) Corresponding 250-m ATPRK-fused MODIS images. Left to right: Data acquired on October 2, 2013, October 18, 2013, and November 3, 2013.

The ideal values for RMSE, CC, SSIM, and SAM are 0, 1, 1, and 0, respectively. As can be seen from Table 2, for all six bands of predictions of SPSTFM, the 250-m fused images result in smaller RMSE and larger CC and SSIM values compared to the 500-m images. The mean CC gain for SPSTFM is 0.0329, and the corresponding mean SSIM gain is 0.0302. With respect to mean RMSE, it is reduced by 0.0021 for SPSTFM. Furthermore, the fusion results based on SPSTFM are more accurate than those based on STARFM and ESTARFM. Specifically, when using 250-m images, the mean CC values of ESTARFM, STARFM, and SPSTFM are 0.7994, 0.8225, and 0.8610, respectively. The mean SSIM values are 0.7905, 0.8167, and 0.8441. The mean CC gains of SPSTFM over ESTARFM and STARFM are 0.0616 and 0.0385, respectively, and the corresponding mean SSIM gains are 0.0536 and 0.0274. The main reason is that although both STARFM and ESTARFM consider the relationship between neighboring pixels when predicting the reflectance of the central pixel, the change trend between pixels may be discontinuous (e.g., abrupt changes), which may exacerbate the performances of STARFM and ESTARFM. The SPSTFM algorithm utilizes the patch as the basic unit of fusion, which considers the continuity of neighbor pixels in each patch and can capture the amplitude and structure of surface changes (such as color and texture) more accurately. Therefore, the performance of SPSTFM is superior to that of STARFM and ESTARFM, especially for the case involving land cover changes (Huang and Song 2012).

Experiment on the Lower Gwydir Catchments Data Set

In this experiment, three pairs of *Landsat 8* OLI and MODIS surface reflectance images covering a 28×28 km area of Lower Gwydir Catchments were used. The images were acquired on October 2, 2013, October 18, 2013, and November 3, 2013. Figure 7 shows the images with NIR-red-green as red-green-blue composite for the 30-m Landsat data (upper row), 500-m MODIS data (middle row), and 250-m fused MODIS data (lower row). It can be seen that from October 2, 2013, to October 18, 2013, some vegetation regions were changed to built-up areas. From October 18, 2013, to November 3, 2013, similar land cover changes also occurred. Similar to the previous experiment, we used two pairs of Landsat-MODIS images on October 2, 2013, and November 3, 2013, as well as the MODIS image on October 18, 2013, to predict the Landsat-like image on October 18, 2013.

Figure 8 shows the predicted 30-m Landsat image on October 18, 2013, based on SPSTFM (using 500-m or 250-m MODIS images as input) and STARFM and ESTARFM (using 250-m MODIS images as input). It can be seen from Figure 8 that the predictions of ESTARFM and STARFM for heterogeneous regions are not as reliable as that of SPSTFM when the same 250-m data were used as input. For example, in heterogeneous subareas S1 and S2, ESTARFM incorrectly predicts some red pixels as green ones, and STARFM incorrectly predicts the brown pixels as red ones. For SPSTFM, however, the predictions are

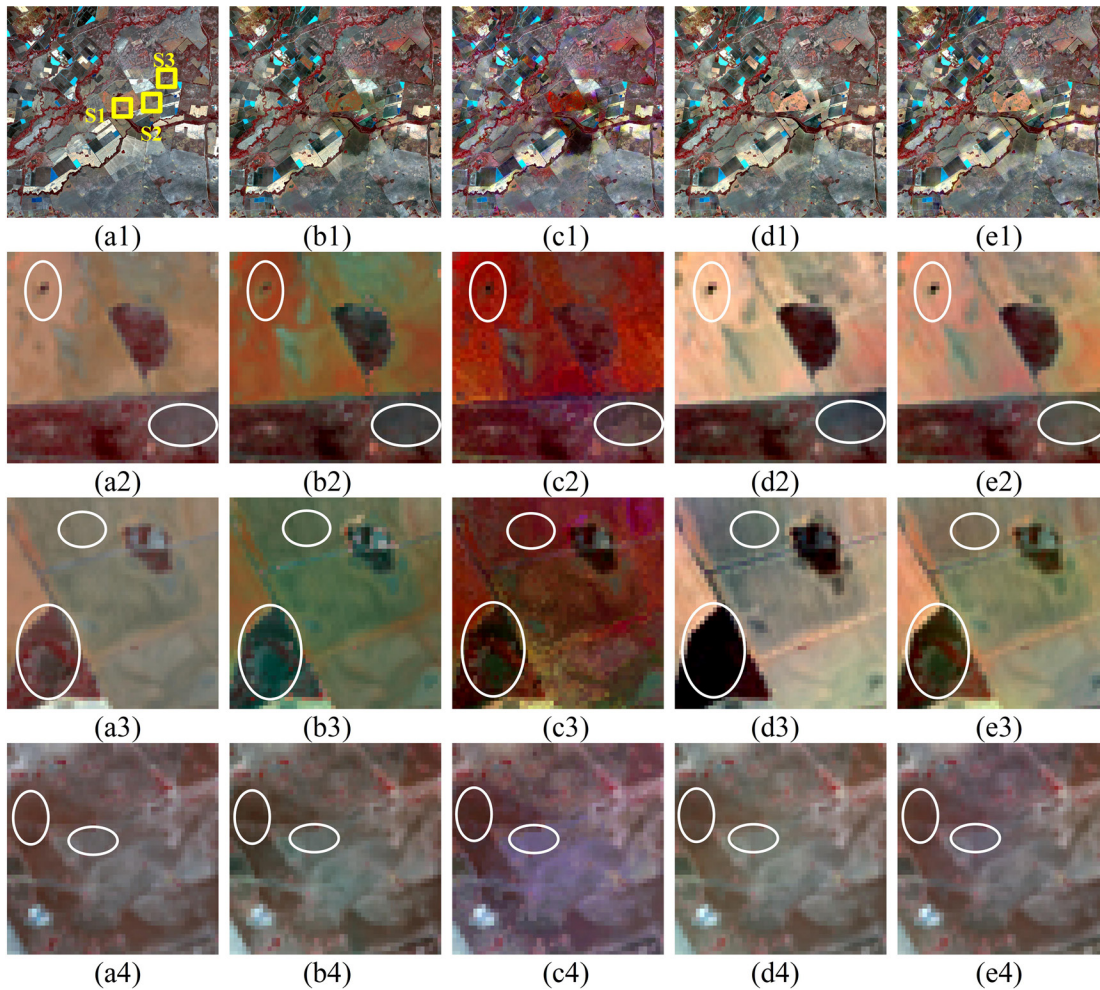


Figure 8. 30-m spatiotemporal fusion results for the Lower Gwydir Catchments data set. (a) 30-m true *Landsat 8* image on October 18, 2013 (the three subareas marked in yellow are used for analysis in lines 2, 3, and 4). (b) 30-m ESTARFM results predicted using the 250-m fused MODIS images. (c) 30-m STARFM results predicted using the 250-m fused MODIS images. (d and e) 30-m SPSTFM results predicted using the original 500-m MODIS images and the 250-m fused MODIS images, respectively. Line 1 shows the results for the whole area, and lines 2, 3, and 4 are the results for the three subareas (S1 and S2 are heterogeneous subareas and S3 is a homogeneous subarea) marked in (a).

obviously closer to the actual image. The main reason is that ESTARFM assumes that the change ratio of each land cover remains constant during the observation period. In reality, however, the change of reflectance of land cover is often affected by many factors, and the change process is more complex. STARFM is proposed based on the assumption that the spectra of similar pixels in the neighborhood are constant and there are no land cover changes during the observation period, which makes the model susceptible to environmental and phenological changes, leading to large errors in prediction for heterogeneous regions and land cover changes. SPSTFM utilizes sparse representation and dictionary learning approaches in signal domain to increase the prediction accuracy of land cover changes and heterogeneous regions. It uses the change patches (in terms of image difference) of fine- and coarse-spatial-resolution images to train fine- and coarse-spatial-resolution joint dictionaries and uses a sparse-coding technique to select the optimal signal combination to approximately reconstruct the original image. When using the algorithm, the reflectance change can be predicted nonlinearly, which is more consistent with reality. Therefore, the spatiotemporal fusion model based on learning can more accurately predict the reflectance variation caused by land cover changes. In addition, it is worth noting that the SPSTFM results produced using a 250-m image are more accurate than those

using a 500-m image. For example, in homogeneous subarea S3, the fusion result produced using a 500-m image incorrectly predicts some gray pixels as green, while the fusion result of a 250-m image is closer to the actual image.

Table 3 lists the quantitative evaluation results in terms of RMSE, CC, SSIM, and SAM. From Table 3, we can see clearly that for SPSTFM, the fusion results produced using the 250-m image lead to smaller RMSE and SAM values, and larger CC and SSIM ones, than those produced using the original 500-m image. Specifically, when using the 250-m image, the mean CC and SSIM values of SPSTFM are increased by 0.0100 and 0.0089, and the mean RMSE and SAM values are reduced by 0.0005 and 0.0009. Meanwhile, when using 250-m data as input it can be found that SPSTFM is the most accurate among the three methods. More precisely, the mean CC gains of SPSTFM over ESTARFM and STARFM are 0.0333 and 0.0995, respectively, and the corresponding mean SSIM gains are 0.0329 and 0.1015. Compared to ESTARFM and STARFM, the mean RMSE reductions of SPSTFM are 0.0038 and 0.0090, respectively, and the corresponding mean SAM reductions are 0.0083 and 0.0248.

Discussion

In this article, we applied ATRPK to fuse the 250-m bands with 500-m bands of MODIS images to acquire 250-m bands 1–7.

Combined with the SPSTFM algorithm, we utilized two pairs of known Landsat-MODIS (250-m) images at t_1 and t_3 , and a 250-m MODIS image at t_2 , to generate a 30-m Landsat-like image at t_2 . Compared with the scheme of using 500-m images, using 250-m images can produce results with more spatial detail and greater accuracy. Meanwhile, when given the same data (i.e., 250-m data) as input, the learning-based spatiotemporal fusion approach SPSTFM outperforms STARFM and ESTARFM.

The ATPRK approach combines linear regression with ATPK, which considers the spatial correlation of pixels and perfectly retains the spectral characteristics of the 500-m bands. The fused 250-m images contain more spatial detail than the original 500-m images, and further provide more effective information for after the spatiotemporal fusion. In this article, the approximate version of ATPRK not only achieves similar performance to ATPRK but also greatly reduces the computing time. While the performance is encouraging, it is worth noting that there exists uncertainty in the state-of-the-art ATPRK method. For example, the linear regression model constructed from 500-m bands may not be suitable for 250-m bands. In future research, we will attempt to develop a more reliable image fusion method for fusing 250-m MODIS data to further enhance spatiotemporal fusion of MODIS and Landsat data.

Compared with the mainstream STARFM and ESTARFM, the learning-based SPSTFM produces great accuracy for heterogeneous areas. In the learning-based spatiotemporal fusion approaches, how to effectively capture the temporal changes of fine- and coarse-spatial-resolution images is extremely important. In this article, the feature-mapping network and overcomplete dictionary are constructed by the image reflectance change characteristics in the observation period, which are applied to reconstruct the reflectance change information at prediction time. However, when the change characteristics are not complete enough, the accuracy of the spatiotemporal fusion result will be compromised to some extent. The sparse-representation approach has been widely used for super-resolution of natural images, where a rich feature-training database is available. On the contrary, for remote sensing images there are still very few feature-training databases that can meet different fusion needs. In future work, it will be of great interest to extract the features that conform to geological characteristics and semantic information of remote sensing images to build a training database, so as to reduce the uncertainty caused by incomplete features (i.e., reflectance change in SPSTFM in this article).

SPSTFM trains fine- and coarse-spatial-resolution dictionary pairs by extracting the effective features (high-frequency information) from the fine- and coarse-spatial-resolution difference images. The mapping relationship between fine- and coarse-spatial-resolution images is constructed by assuming that the sparse coefficients at different spatial resolutions are the same. In recent years, deep learning has received extensive attention. Deep learning needs a large amount of data to train the learning model. Since remote sensing data have the characteristics of being massive in volume and rich in information, we can utilize the “big data” characteristic of deep learning-based training to obtain a more effective mapping relationship between MODIS and Landsat images to further increase the reconstruction accuracy. In addition, although SPSTFM is superior to STARFM and ESTARFM, its computing time is long, which is the common issue with learning-based algorithms. In this article, the computational time of SPSTFM is about 4 hours, whereas those of STARFM and ESTARFM are both less than 30 minutes. Therefore, our further research will also follow the idea of simultaneously increasing the accuracy of fusion and reducing the computational complexity. Specifically, in the process of tuning parameters, we found that the number of dictionary atoms has a certain effect on

the prediction accuracy. That is, a larger number of dictionary atoms can result in greater prediction accuracy, which means that sufficient dictionary atoms can fit the spatial features in images more reliably. This is consistent with the points mentioned by Yang *et al.* (2010). However, as the number of atoms increases, the time for training and reconstructing also increases correspondingly. We can try to select dictionary atoms with rich spatial details, such as heterogeneous image patches. However, it is also a difficult problem to select appropriate samples from thousands of image patches, as there are a large number of similar image patches in the same region. Therefore, in future research it is expected that a method will be found for screening samples, which can increase accuracy under a smaller number of dictionary atoms. In addition, the size of the image patch is an important factor that affects the computing time. It is worthwhile to explore a method to quantitatively analyze the impact of image-patch size in different regions and bands, and select an optimal size accordingly.

Conclusion

This article proposes a new spatiotemporal fusion strategy by using 250-m MODIS data for sparse representation. First, the 250-m fused MODIS images are produced using ATPRK. Then the existing advanced SPSTFM approach is used to fuse 250-m MODIS images and 30-m Landsat images to produce the Landsat-like image. The experimental results of two data sets show that compared with the existing scheme of using original 500-m MODIS data, using 250-m fused MODIS data can produce more accurate predictions. Meanwhile, when using the same 250-m MODIS data, the SPSTFM predictions are more accurate than those of the popular STARFM and ESTARFM methods.

Acknowledgments

This work was supported by the National Natural Science Foundation of China under Grants 41971297 and 61675051, Fundamental Research Funds for the Central Universities under Grant 02502150021, and Tongji University under Grant 02502350047.

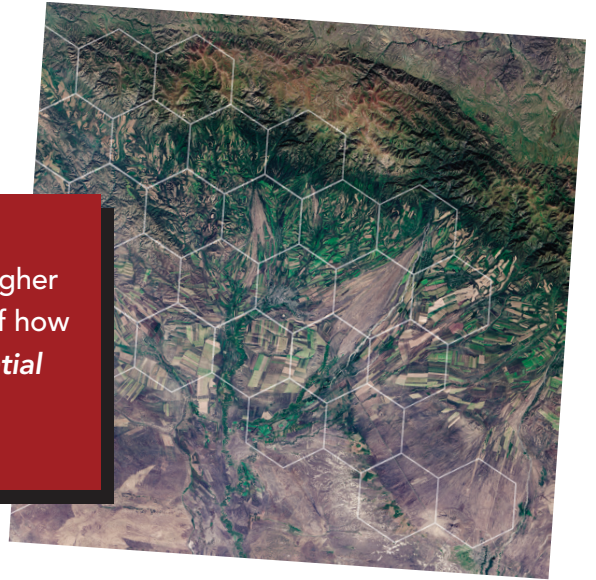
References

- Aharon, M., M. Elad and A. Bruckstein. 2006. K-SVD: An algorithm for designing overcomplete dictionaries for sparse representation. *IEEE Transactions on Signal Processing* 55 (11):4311–4322.
- Anderson, M. C., R. G. Allen, A. Morse and W. P. Kustas. 2012. Use of Landsat thermal imagery in monitoring evapotranspiration and managing water resources. *Remote Sensing of Environment* 122:50–65.
- Cherchali, S., O. Amram and G. Flouzat. 2000. Retrieval of temporal profiles of reflectances from simulated and real NOAA-AVHRR data over heterogeneous landscapes. *International Journal of Remote Sensing* 21 (4):753–775.
- Davis, G., S. Mallat and M. Avellaneda. 1997. Adaptive greedy approximations. *Constructive Approximation* 13 (1):57–98.
- Fortin, J.-P., M. Bernier, A. El Battay. 2000. Estimation of surface variables at the sub-pixel level for use as input to climate and hydrological models, Final report to Centre national d'études Spatiales (France) Rapport de recherche INRS-Eau.
- Ganguly, S., M. A. Friedl, B. Tan, X. Zhang, and M. Verma. 2010. Land surface phenology from MODIS: Characterization of the Collection 5 global land cover dynamics product. *Remote Sensing of Environment* 114 (8):1805–1816.
- Gao, F., J. Masek, M. Schwaller and F. Hall. 2006. On the blending of the Landsat and MODIS surface reflectance: Predicting daily Landsat surface reflectance. *IEEE Transactions on Geoscience and Remote Sensing* 44 (8):2207–2218.
- Goetz, S. 2007. Crisis in earth observation. *Science* 315 (5820):1767.

- Hansen, M. C., R. S. Defries, J.R.G. Townshend and R. Sohlberg. 2000. Global land cover classification at 1 km spatial resolution using a classification tree approach. *International Journal of Remote Sensing* 21 (6–7):1331–1364.
- He, C., P. Shi, D. Xie and Y. Zhao. 2010. Improving the normalized difference built-up index to map urban built-up areas using a semiautomatic segmentation approach. *Remote Sensing Letters* 1 (4):213–221.
- Hilker, T., M. A. Wulder, N. C. Coops, J. Linke, G. McDermid, J. G. Masek, F. Gao and J. C. White. 2009. A new data fusion model for high spatial- and temporal-resolution mapping of forest disturbance based on Landsat and MODIS. *Remote Sensing of Environment* 113 (8):1613–1627.
- Huang, B. and H. Song. 2012. Spatiotemporal reflectance fusion via sparse representation. *IEEE Transactions on Geoscience and Remote Sensing* 50 (10):3707–3716.
- Kruse, F. A., A. B. Lefkoff, J. W. Boardman, K. B. Heidebrecht, A. T. Shapiro, P. J. Barloon and A.F.H. Goetz. 1993. The spectral image processing system (SIPS)—Interactive visualization and analysis of imaging spectrometer data. *Remote Sensing of Environment* 44:145–163.
- Roy, D. P., J. Ju, P. Lewis, C. Schaaf, F. Gao, M. Hansen and E. Lindquist. 2008. Multi-temporal MODIS–Landsat data fusion for relative radiometric normalization, gap filling, and prediction of Landsat data. *Remote Sensing of Environment* 112 (6):3112–3130.
- Song, H. and B. Huang. 2013. Spatiotemporal satellite image fusion through one-pair image learning. *IEEE Transactions on Geoscience and Remote Sensing* 51 (4):1883–1896.
- van der Meer, F. D., H.M.A. van der Werff, F.J.A. van Ruitenbeek, C. A. Hecker, W. H. Bakker, M. F. Noomen, M. van der Meijde, E.J.M. Carranza, J. B. de Smeth and T. Woldai. 2012. Multi- and hyperspectral geologic remote sensing: A review. *International Journal of Applied Earth Observation and Geoinformation* 14 (1):112–128.
- Wang, Q. and P. M. Atkinson. 2018. Spatio-temporal fusion for daily Sentinel-2 images. *Remote Sensing of Environment*. 204:31–42.
- Wang, Q., W. Shi and P. M. Atkinson. 2016. Area-to-point regression kriging for pan-sharpening. *ISPRS Journal of Photogrammetry and Remote Sensing* 114:151–165.
- Wang, Q., W. Shi, P. M. Atkinson and Y. Zhao. 2015. Downscaling MODIS images with area-to-point regression kriging. *Remote Sensing of Environment* 166:191–204.
- Wang, Q., Y. Zhang, A. O. Onojeghuo, X. Zhu and P. M. Atkinson. 2017. Enhancing spatio-temporal fusion of MODIS and Landsat data by incorporating 250 m MODIS data. *IEEE Journal of Selected Topics in Applied Earth Observations and Remote Sensing* 10 (9):4116–4123.
- Wang, Z., A. C. Bovik, H. R. Sheikh and E. P. Simoncelli. 2004. Image quality assessment: From error visibility to structural similarity. *IEEE Transactions on Image Processing* 13 (4):600–612.
- Wu, M., W. Huang, Z. Niu and C. Wang. 2015. Generating daily synthetic Landsat imagery by combining Landsat and MODIS data. *Sensors* 15 (9):24002–24025.
- Wu, M., Z. Niu, C. Wang, C. Wu and L. Wang. 2012. Use of MODIS and Landsat time series data to generate high-resolution temporal synthetic Landsat data using a spatial and temporal reflectance fusion model. *Journal of Applied Remote Sensing* 6 (1):063507.
- Xu, H.-Q. 2005. Extraction of water body information using improved normalized difference water body index (MNDWI). *Journal of Remote Sensing* 9 (5):79–85.
- Yang, J., J. Wright, T. S. Huang and Y. Ma. 2010. Image super-resolution via sparse representation. *IEEE Transactions on Image Processing* 19 (11):2861–2873.
- Zhang, X., M. A. Friedl, C. B. Schaaf, A. H. Strahler, J.C.F. Hodges, F. Gao, B. C. Reed and A. Huete. 2003. Monitoring vegetation phenology using MODIS. *Remote Sensing of Environment* 84 (3):471–475.
- Zhu, X., J. Chen, F. Gao, X. Chen and J. G. Masek. 2010. An enhanced spatial and temporal adaptive reflectance fusion model for complex heterogeneous regions. *Remote Sensing of Environment* 114 (11):2610–2623.
- Zhu, X., E. H. Helmer, F. Gao, D. Liu, J. Chen and M. A. Lefsky. 2016. A flexible spatiotemporal method for fusing satellite images with different resolutions. *Remote Sensing of Environment* 172:165–177.
- Zhukov, B., D. Oertel, F. Lanzl and G. Reinhackel. 1999. Unmixing-based multisensor multiresolution image fusion. *IEEE Transactions on Geoscience and Remote Sensing* 37 (3):1212–1226.

GEOSPATIAL REVOLUTION

With more than 1 million video views, the *Geospatial Revolution Project* is the go-to source for government, higher education, and workforce development for an overview of how geospatial technology is changing the world. The *Geospatial Revolution Project* is anchored in a world-class research university and trusted for its PBS editorial standards.



THE NEXT GENERATION

WPSU Penn State is celebrating the 10th Anniversary (2010-2020) of the launch of the original *Geospatial Revolution Project* with a new video episode about next-generation innovations in geospatial technology.

Our Emmy Award-winning production team explores stories from public safety, business, and national defense. The real revolution in geospatial technologies is just beginning!



CONTACT

Please make a philanthropic gift to WPSU Penn State to support the new episode. *For more information, contact:*

Elaine Brzycki
Project Development
WPSU Penn State
ejb23@psu.edu

Kristian Berg
Director, Geospatial Revolution Project
WPSU Penn State
kjb35@psu.edu

Dr. Todd S. Bacastow
Teaching Professor
Dept. of Geography • Penn State
tsb4@psu.edu

Karen Schuckman
Associate Teaching Professor
Dept. of Geography • Penn State
kls505@psu.edu

AUDIENCES & DISTRIBUTION

The new episode—with ready-made *Geospatial Revolution* audiences in government, public safety, industry, education, and the general public—will be screened at conferences, posted to social media, linked to the original project website, and shared with original engagement partners:

- U.S. government (e.g., U.S. DOD, NGA, FBI, U.S. Army Corps of Engineers)
- Higher education/workforce development collaborators
- K-12 STEM education

“Geospatial Revolution is considered the ‘Bible’ of the GIS field. I can’t wait to see the next episode!”

– Dr. Salvatore Amaduzzi
University of Udine, Italy



GEOSPATIAL REVOLUTION
geospatialrevolution.psu.edu

LEARN
DO
GIVE
BELONG

ASPRS Offers

- » Cutting-edge conference programs
- » Professional development workshops
- » Accredited professional certifications
- » Scholarships and awards
- » Career advancing mentoring programs
- » *PE&RS*, the scientific journal of ASPRS

asprs.org

ASPRS